

LOW VOLTAGE, MEMS-BASED REFLECTIVE AND REFRACTIVE OPTICAL
SCANNERS FOR ENDOSCOPIC BIOMEDICAL IMAGING

By

ANKUR JAIN

A DISSERTATION PRESENTED TO THE GRADUATE SCHOOL
OF THE UNIVERSITY OF FLORIDA IN PARTIAL FULFILLMENT
OF THE REQUIREMENTS FOR THE DEGREE OF
DOCTOR OF PHILOSOPHY

UNIVERSITY OF FLORIDA

2006

Copyright 2006

by

Ankur Jain

To my parents, Ranjan and Poonam, to my brother Prateek, and to my fiancée Kavitha for their constant love, unwavering support, confidence and encouragement.

ACKNOWLEDGMENTS

I would like to thank my advisor, Dr. Huikai Xie, for the constant support and guidance he has given me over the past few years. I first met Huikai in August 2002, and subsequently joined his research group as a PhD student in the fall semester. I am grateful for all the insight he has provided, and am thankful to him for introducing me to the areas of MEMS and endoscopic biomedical imaging. I have personally gained technical expertise, as well as professional know-how through my interactions with him, and I will forever be indebted to him for mentoring me towards becoming a better microsystems technology engineer. The research presented in this dissertation was also painstakingly reviewed by other members of my PhD committee, Dr. Toshikazu Nishida, Dr. Ramakant Srivastava, and Dr. William Ditto, and for that I am grateful. I have enjoyed many conversations with Dr. Nishida, both personally and professionally. Working as a graduate teaching assistant for Dr. Srivastava was a pleasure, and I am grateful for our personal friendship. Dr. Ditto has provided me with unique insights related to the biomedical application aspect of this project.

I want to acknowledge technical and personal discussions with Dr. Mark Sheplak and Dr. David Arnold, as their advice helped improve my research work and their pleasant company at MEMS conferences is always welcome. Further appreciation goes out to Dr. Peter Zory for his valuable friendship, for always being a mentor, and for his indispensable lessons on how to maintain a good research notebook.

The Biophotonics and Microsystems Lab (BML) located in 136 Larsen Hall was home to this project, and I am indebted to my BML group members. Special thanks go out to Hongwei Qu for teaching me the ropes in the cleanroom, and to Shane Todd for helping me with electrothermal modeling. Hongwei has always been a pillar of support within BML, and I enjoyed working with him on various projects. Shane worked with me on various micromirror projects, and I have benefited greatly from our professional interactions and personal friendship. I would like to acknowledge support from Anthony Kopa, both personally and also for using my 2-D micromirror for imaging purposes. Other BML members who aided me during the course of my research include Deyou Fang, Maojiao He, Mi Huang, Mingliang Wang, Ben Caswell and the newcomers Kemiao “Alex” Jia and Lei Wu. Alex and Lei have proven to be worthy successors for my project, and I will value their camaraderie. All BML members work great as a team, and I have so many good memories about the multilingual jokes told in the lab, and the parties and sports that we all participated in.

BML is just part of the much bigger microsystems group at the University of Florida, known as the Interdisciplinary Microsystems Group (IMG). I am grateful to all IMG members for their support-group-like environment and technical expertise. In particular, I would like to thank my colleagues Venkat Chandrasekaran, Stephen Horowitz, Anurag Kasyap, Chris Bahr, David Martin, Ryan Holman, Erin Patrick, Israel Boniche, Janhavi Agashe, Sheetal Shetye, Jian “Jackie Chan” Liu, Yawei Li, Vijay Chandrasekharan, Lee Hunt, Tai-An Chen, Karthik Kadirvel, Robert Taylor, Brandon Bertolucci, Champak Das and Zheng Xia, to name a few. Venkat introduced me to the world of wire-bonding, while Dave, Ryan and Chris kept our IMG server running 24/7.

Thanks go to Anurag for helping me with the vibrometer, to Erin for help with the PCB milling machine, and to Israel and Janhavi for AutoCAD assistance. I thank Brandon and the Ultimate Frisbee gang for relentlessly organizing sporting events that helped to upkeep the morale of IMG. Finally, credit is due to all other IMG members for general technical assistance, and for maintaining a lively work environment in the office, lab and even inside the cleanrooms.

This work would not be complete without help from our external collaborators. I thank Dr. Yingtian Pan and Zhenguo Wang at the State University of New York at Stony Brook for validating the use of my micromirrors for endoscopic optical coherence tomographic (OCT) imaging. I am grateful that they invited me to visit their lab so that I could witness OCT imaging using my endoscopically-packaged micromirrors. Two-photon excitation fluorescence imaging and second harmonic generation nonlinear optical imaging experiments using my micromirrors were demonstrated in collaboration with Dr. Min Gu and Ling Fu at the Swinburne University of Technology, Australia. I thank Ling for the many hours she has put into this project, and for her personal friendship. I would also like to thank Dr. Michael Bass and Te-Yuan Chung from CREOL, University of Central Florida, Orlando, for letting me use their thermal imager for my research.

The MEMS device fabrication was done using the facilities provided by the University of Florida Nanofabrication Facilities (UFNF) and by the UF Microfabritech center. Therefore, I appreciate the support provided by the UFNF staff Al Ogden, Ivan Kravchenko, Bill Lewis and the UF Microfabritech staff. Scanning electron microscopy (SEM) and white light profilometry were performed using the equipment at the Major

Analytical Instrumentation Center (MAIC) at the University of Florida. I wish to thank Dr. Luisa Dempere, Wayne Acree, Andrew Gerger and Brad Willenberg of the MAIC for their assistance. Special thanks go to Tanya Riedhammer who helped me with the Variable-Pressure SEM for imaging my photoresist microlenses. I also want to acknowledge our administrative assistant, Joyce White, for her help and support.

Finally, I am eternally grateful to my family and friends for their constant support and encouragement. I would like to thank my parents, Ranjan and Poonam, and my brother, Prateek, for their confidence in me, for their endless love and support, and for keeping me debt-free all through graduate school. I want to thank my fiancée Kavitha, for all her love, support, advice, and also for all the car rides to school she provided that ultimately helped my research. Thanks are due to my friends Anuradha Ventakesan and Boman Irani who kept me going throughout graduate school. I also want to acknowledge my friends Kanak Behari Agarwal and Himanshu Kaul whose learned advice helped me through the “mid-PhD crisis”.

The MEMS-based endoscopic biomedical imaging project at the University of Florida has been supported by the National Science Foundation Biophotonics Program through award number BES-0423557, and by the Florida Photonics Center for Excellence.

TABLE OF CONTENTS

	<u>page</u>
ACKNOWLEDGMENTS	iv
LIST OF TABLES	xi
LIST OF FIGURES	xii
ABSTRACT	xviii
CHAPTER	
1 INTRODUCTION	1
1.1 Limitations of Conventional Cancer Diagnosis Methodologies.....	1
1.2 Emerging Optical Coherence Tomography	3
1.3 MEMS-based OCT	4
1.4 MEMS-based OCM	6
1.5 Research Objectives.....	9
1.6 Dissertation Overview	10
2 OPTICAL BIOIMAGING METHODOLOGIES.....	12
2.1 Optical Coherence Tomography.....	12
2.1.1 OCT System Design	13
2.1.2 Key Imaging Parameters	17
2.1.3 Internal Organ OCT Imaging	20
2.1.4 MEMS-based OCT	22
2.2 Optical Coherence Microscopy	24
2.2.1 Bench-Top OCM.....	26
2.2.2 MEMS-based OCM.....	27
2.3 Non Linear Optical Imaging.....	29
2.3.1 Two-Photon Excitation Fluorescence Imaging	30
2.3.2 Second Harmonic Generation Imaging	33
2.3.3 Nonlinear Optical Imaging System Design.....	35
2.3.4 Endoscopic Nonlinear Optical Imaging	37
2.3.5 MEMS-based Endoscopic Nonlinear Optical Imaging.....	39
3 ELECTROTHERMAL MICROMIRRORS AND ENDOSCOPIC OCT IMAGING.....	40

3.1	Scanning Micromirrors	40
3.2	Electrothermal Actuation and Design	44
3.3	Microfabrication Process	46
3.4	Bimorph Actuation and Theoretical Analysis	50
3.5	Electrothermal Micromirrors	54
3.5.1	One-Dimensional Electrothermal Micromirror	54
3.5.2	Two-dimensional Electrothermal Micromirror	57
3.5.2.1	Device design	57
3.5.2.2	Device characterization	59
3.5.2.3	Laser scanning experiment	62
3.6	Micromirror Packaging	63
3.7	MEMS-based Endoscopic OCT Imaging	65
3.7.1	MEMS-based OCT System Design	65
3.7.2	OCT Imaging Results	71
3.8	Summary	73
4	LARGE-VERTICAL-DISPLACEMENT MICROMIRRORS AND NON-LINEAR OPTICAL IMAGING	75
4.1	LVD Microactuator Design	77
4.2	1-D LVD Micromirror	80
4.2.1	Fabricated Device	80
4.2.2	Equivalent Circuit Model	81
4.2.3	Experimental Results	86
4.2.3.1	Static response	86
4.2.3.2	Frequency response/resonant scanning	89
4.3	2-D LVD Micromirror	92
4.3.1	Mirror Design	92
4.3.2	Experimental Results	94
4.3.2.1	Bi-directional scanning	94
4.3.2.2	Two-dimensional dynamic scanning	98
4.3.2.3	Vertical displacement motion	100
4.4	MEMS Mirror-based Nonlinear Endoscopy	102
4.4.1	Nonlinear Optical Imaging System	103
4.4.2	Experimental Results	104
4.5	Summary	107
5	MICROLENS SCANNERS AND OPTICAL CONFOCAL MICROSCOPY	109
5.1	LVD Microlens Scanner	109
5.1.1	Microlens Scanner Design	111
5.1.2	Fabricated Microlens Scanner	111
5.1.3	Experimental Results	115
5.2	Millimeter-Range LVD Microlens Scanner	119
5.2.1	Millimeter-Range Scanner Design	120
5.2.2	Fabrication Process	121
5.2.3	Experimental Results	126

5.3 LVD Microlens Packaging	132
5.4 Summary	134
6 CONCLUSIONS AND FUTURE WORK	135
6.1 Research Effort Accomplishments	137
6.2 Future Work	138
APPENDIX	
A NON-CMOS, WAFER LEVEL FABRICATION PROCESS	140
B ARTICLES GENERATED BY THIS RESEARCH EFFORT	145
LIST OF REFERENCES	148
BIOGRAPHICAL SKETCH	162

LIST OF TABLES

<u>Table</u>	<u>page</u>
3-1 Thermomechanical properties of some possible bimorph materials at room temperature.....	45
4-1 Parameters used by the equivalent circuit model of the 1-D LVD micromirror.....	84
4-2 Actuator characteristics for the 2-D LVD micromirror.	96
5-1 Microlens characteristics.....	113
5-2 Estimated microlens parameters for various desired focal lengths.	126

LIST OF FIGURES

<u>Figure</u>	<u>page</u>
1-1 Schematic of a MEMS-based OCT/OCM system. (a) System block diagram. (b) Optical delay line that uses the LVD micromirror as a reference mirrors for transverse and axial scanning. (c) OCT endoscope that uses a 1-D or 2-D LVD micromirror for transverse scanning of tissue. (d) OCM endoscope that uses a LVD microlens for axial scanning of tissue.....	7
2-1 OCT schematic.....	13
2-2 OCT tissue scanning modes. (a) Conventional longitudinal scanning (A-scan). (b) <i>En-face</i> scanning (B-scan).....	15
2-3 Comparison between histology, ultrasound and OCT images of biological tissue. (a) HE-stained histology, (b) 50-MHz ultrasound, and (c) OCT image of a nevus.....	16
2-4 Comparison between ultrasound and OCT images of human coronary artery plaques. (a) <i>In vivo</i> OCT image with axial imaging resolution of 13 μm . (b) 30 MHz intravascular ultrasound image of the same artery with a lower resolution of 100 μm	17
2-5 Gaussian beam optics.....	19
2-6 Existing endoscopic OCT probe designs.(a) Radial imaging probe design. (b) Forward imaging probe design.....	20
2-7 MEMS-based endoscopic OCT system.....	24
2-8 High NA scanning approaches for OCT. (a) Reference mirror and focusing optics placed on a movable stage to achieve dynamic focusing. (b) Lateral and axial scanning achieved by displacement of the fiber tip.....	25
2-9 MEMS-based endoscopic OCM schematic.....	26
2-10 Difference between OCM and OCT.....	27
2-11 1- μm axial resolution by 3- μm lateral resolution tomogram of a tadpole.	28

2-12	Energy band diagrams illustrating (a) one photon and, (b) two photon excitation fluorescence phenomena.	31
2-13	Optical sectioning ability of TPEF imaging. (a) Single-photon excitation of fluorescein by 488 nm light. (b) Two-photon excitation using 960 nm light.	32
2-14	Schematic of a nonlinear microscope.....	36
2-15	(a) Pulse train from a mode-locked Ti:Sapphire laser at 80 MHz. (b) The laser pulses typically have a FWHM duration of 100 fs, and (c) a spectral FWHM bandwidth of ~ 10 nm.	36
2-16	Two-photon fluorescence and SHG signals emitted by a sample excited by 800 nm light.	37
2-17	Two-photon imaging of the hamster cheek pouch tissue at an excitation wavelength of 780 nm. (a) Normal tissue. Precancerous tissue: (b) Moderate Dysplasia. (c) Carcinoma <i>in situ</i> . Cancerous tissue: (d) nonpapillary, and (e) papillary squamous cell carcinoma.	38
3-1	Side view of a bimorph beam.....	45
3-2	Electrothermal micromirror basic structure. (a) Top view. (b) Cross-sectional side view.....	47
3-3	DRIE CMOS-MEMS fabrication process flow.	48
3-4	SEM of a fabricated 1-D micromirror with initial tilt angle.	50
3-5	Bimorph actuation mechanism. Side views of: (a) Initial position of mirror at zero bias. (b) Downward rotation of mirror plate on application of bias voltage to polysilicon resistor.	51
3-6	SEM of 1-D micromirror.....	55
3-7	1-D mirror characterization. (a) Rotational static response. (b) Plot of the heater resistance versus applied current.	56
3-8	Frequency response of the 1-D mirror.	56
3-9	Schematic of the 2-D mirror design. (a) Top view showing the axes of rotation. (b) Cross-sectional view of A-A'.	58
3-10	SEM of a fabricated 2-D micromirror.....	59
3-11	2-D Mirror Characterization. (a) Rotation angle vs. current, and (b) Polysilicon resistance vs. current for the two actuators.	60

3-12	Thermal images of a device biased at 10 V. (a) Temperature distribution across the mirror actuator only. (b) Thermograph of the entire device.....	61
3-13	Laser scanning using the 2-D mirror. (a) Schematic of experimental setup. (b) 4 x 4 pixel images scanned by the micromirror.	63
3-14	Micromirror package. (a) Packaged micromirror on a custom PCB. (b) Picture of the PCB package. (c) Picture of a packaged mirror alongside a US dime coin...	64
3-15	Endoscopic OCT probe designs. (a) Side-imaging configuration. (b) Forward-imaging configuration.	65
3-16	Schematic of the MEMS-based endoscopic OCT system.....	66
3-17	Photographs of the 5-mm diameter MEMS-based OCT endoscope at the State University of New York at Stony Brook.....	69
3-18	Photograph of the portable, MEMS-based endoscopic OCT system at the State University of New York at Stony Brook.....	70
3-19	Comparison of OCT with histological image. (a) OCT image, and (b) histological image of rat bladder.....	71
3-20	Bench-top versus MEMS-based endoscopic OCT imaging of rat bladder. (a) Bench-top OCT image. Size: 6 mm by 2.7 mm. (b) Endoscopic MEMS-based OCT image. Size: 4 mm by 2.7 mm.....	72
4-1	Design schematic of the LVD mirror. (a) Top view. (b) Cross-sectional view across A-A'.	77
4-2	Coventor simulations. (a) Device side-view. (b) 3-D model of the LVD micromirror illustrating the initial curling of the bimorph actuators.	78
4-3	Wiring schematic for the LVD actuators.	79
4-4	SEM images of the LVD micromirror.	81
4-5	Line scan of the surface profile of the LVD micromirror.	81
4-6	Equivalent circuit model of the LVD micromirror device.....	82
4-7	SEM of the burn pattern of the mirror actuator.....	85
4-8	LVD mirror characterization. Plots of the (a) rotation angle versus applied voltage, and (b) polysilicon heater resistance versus applied voltage for the two actuators. (c) Plot showing the linear correlation between rotation angle and polysilicon resistance of the actuators.....	88

4-9	Piston motion mode. (a) Vertical displacement of the mirror plate as a function of the frame actuator voltage. (b) Plot of the mirror actuator voltage versus frame actuator voltage that was used to drive the LVD device to obtain less than 0.03° tilting of the mirror plate.....	90
4-10	Frequency response of the LVD micromirror device.....	91
4-11	2-D LVD micromirror design. (a) Top view of the 2-D micromirror, highlighting the 4 bimorph actuators. (b) Top view of the actuator area boxed in part (a). (c) Cross-sectional view of the bimorph actuator as seen across A-A'.....	93
4-12	SEM of a fabricated 2-D LVD mirror.....	93
4-13	Static 2-D line scans. (a) Plot showing the optical angles scanned in 2-D space when each actuator is individually actuated. (b) Plot of the effective optical angle scanned versus actuation voltage for each actuator.....	95
4-14	Static characterization. (a) Plot showing the linear scan pattern during static 2-D scanning of <i>Act1</i> and <i>Act4</i> only. <i>Act4</i> was actuated at different <i>Act1</i> bias voltages. (b) Linear plot of actuator resistance versus optical scan angle for each actuator.....	96
4-15	Tilt angle stability of the mirror plate versus time.....	97
4-16	Initial tilt angle of the mirror plate in x and y directions at different environmental temperatures.....	98
4-17	Photographs of 2-D scan patterns obtained by exciting actuators 1 and 4 only. (a)-(e) Lissajous figures scanned by the micromirror by varying only the phase of the two excitation signals. (f) Lissajous figure scanned at an excitation frequency ratio of 1:10.....	99
4-18	2-D raster scanning pattern obtained using actuators 1 and 4.....	99
4-19	Piston motion mode. (a) Vertical displacement of the mirror plate as a function of <i>Act4</i> voltage. (b) Corresponding plot of the relationship between <i>Act3</i> and <i>Act4</i> voltages that is required to generate the vertical displacement. (c) Linear increase of <i>Act3</i> and <i>Act4</i> resistance with vertical displacement.....	101
4-20	Tilting of the mirror plate in the negative y-direction (due to thermal coupling) as a function of vertical position of the mirror.....	102
4-21	Schematic of the nonlinear optical imaging system.....	103
4-22	Cross-sectional view of the double-clad photonic crystal fiber.....	104

4-23	Second harmonic generation imaging. (a) Series of SHG line profiles from rat tail tendon taken at 10 μm axial steps. (b) SHG line profile of an unstained rat esophagus tissue.	105
4-24	2-D raster scan pattern scanned by actuators 1 and 4 only.	106
4-25	TPEF imaging of 10- μm diameter fluorescent microbeads. (a) Bench-top TPEF imaging system. (b) MEMS-based TPEF imaging.	106
4-26	<i>In vitro</i> imaging of rat stomach epithelial surface stained with 1% acridine orange in Ringer's solution.	107
5-1	Design schematic of the LVD microlens scanner. (a) Top view. (b) Cross-sectional side view. (c) 3-D illustration of the scanner.	112
5-2	SEMs of: (a) Fabricated LVD lens holder, and (b) LVD microlens scanner.	113
5-3	Microlens fabrication process. (a) Backside Si etch. (b) Oxide etch. (c) Deep Si trench etch. (d) Si undercut. (e) Microlens formation by reflow of photoresist.	114
5-4	SEM of a fabricated PR microlens.	115
5-5	Vertical displacement experiment. (a) Vertical displacement of the microlens as a function of frame actuator voltage. (b) Plot of the ratio of the applied voltages to the lens and frame actuators that was used to obtain the vertical displacement shown in (a).	116
5-6	Plot showing the increase in polysilicon heater resistances versus vertical displacement for the two actuators.	117
5-7	Microlens imaging quality. (a) Schematic of the imaging experiment apparatus. (b) Photo of the test pattern. (c) Snap-shot images of the test pattern as obtained through the PR microlens.	118
5-8	CCD image of a 4 μm focused beam spot (top), and its corresponding intensity profile (bottom).	119
5-9	Top view of the millimeter-range LVD microlens scanner.	120
5-10	Modified fabrication process for mm-LVD microlens scanner. (a) Backside Si etch. (b) Oxide etch. (c) Spin on photoresist. (d) Anisotropic photoresist etch to expose metal-2 layer. (e) Metal wet etch followed by photoresist removal. (f) Deep Si trench etch. (g) Silicon undercut. (h) Microlens formation by reflow of photoresist.	121
5-11	Modified process for die-level fabrication of the microlens scanner.	122

5-12	Photograph of the CMOS die after the wet etch of lithographically exposed aluminum layers.	123
5-13	(a) SEM of a fabricated scanner before microlens formation. Close-up views of (b) lens actuator; and (c) frame actuator bimorph regions.	124
5-14	SEM of a fabricated microlens scanner with integrated polymer microlens.	124
5-15	SEMs of (a) convex microlens, and (b) ball-type microlens.	125
5-16	Imaging using the photoresist microlens. (a) Photograph of the test pattern on a chrome mask. (b) Corresponding image of the test pattern as seen at the focal plane of the photoresist microlens.	126
5-17	Vertical displacement of the microlens scanner. (a) Microlens displacement as a function of frame actuator voltage. (b) Displacement versus applied electrical power. (c) Corresponding linear relationship between the two voltages.	128
5-18	Change in resistance versus vertical displacement of the microlens.	129
5-19	Change of initial microlens elevation with ambient temperature.	129
5-20	Lateral shift of the microlens during vertical displacement actuation. (a) Illustration of the lateral shift. (b) Characterized plot of the lateral shift.	130
5-21	Dynamic response of the microlens scanner. (a) Mechanical response when a square excitation was applied to both actuators at $t = 0$. This can be fitted to an exponential envelope using the damping ratio, ξ . (b) Frequency response showing the resonant peaks.	131
5-22	Microlens package design. (a) Microlens package schematic. (b) Forward-imaging OCM endoscope.	132
5-23	Packaged OCM endoscope. (a) With the Lucite end cap. (b) Without the end cap to show the packaged microlens scanner.	133
A-1	Non-CMOS, wafer-level fabrication process illustrating the steps required to fabricate the 1-D LVD micromirror device.	140

Abstract of Dissertation Presented to the Graduate School
of the University of Florida in Partial Fulfillment of the
Requirements for the Degree of Doctor of Philosophy

LOW VOLTAGE, MEMS-BASED REFLECTIVE AND REFRACTIVE OPTICAL
SCANNERS FOR ENDOSCOPIC BIOMEDICAL IMAGING

By

Ankur Jain

August 2006

Chair: Huikai Xie

Major Department: Electrical and Computer Engineering

Imaging technologies such as optical coherence tomography (OCT), two-photon excitation fluorescence microscopy (TPEF), and second harmonic generation (SHG) microscopy require optical scanners to transversely scan a focused laser beam onto the tissue specimen being imaged. However, for *in vivo* early-cancer detection of internal organs the optical scanners must be integrated into slender endoscopes. The goal of this work is to develop millimeter-sized MEMS optical scanners packaged inside endoscopes to enable endoscopic biomedical imaging.

This work reports MEMS micromirrors and microlens scanners fabricated using post-CMOS micromachining processes, which can provide large scan ranges at low driving voltages. Several 1-D and 2-D micromirror scanners have been designed, fabricated and characterized. Scanning micromirrors, as large as 1.3 by 1.1 mm², have demonstrated optical scan angles greater than 40° at actuation voltages below 20Vdc. The

maximum scanning speed of these devices is in the range of 200 to 500Hz, which is adequate for real-time bio-imaging.

A new electrothermal microactuator design is reported which enables large vertical displacements (LVD). This LVD microactuator uses two sets of electrothermal bimorph thin-film beams to provide out-of-plane elevation to the micromirror, while keeping the mirror parallel to the substrate. LVD micromirrors have demonstrated large bi-directional scanning ability ($>\pm 40^\circ$) as well as large vertical piston motion ($\sim 0.5\text{mm}$) at low driving voltages ($< 15\text{V}$). A 1-D LVD micromirror has the ability to scan optical angles greater than 170° at its resonance frequency of 2.4kHz.

Polymer microlenses integrated with the LVD microactuators have been developed for endoscopic optical coherence microscopy which requires microlenses to axially scan their focal planes by 0.5 to 2 mm. A modified fabrication process allows larger polymer lenses with better thermal isolation to be integrated. A maximum vertical displacement of 0.71mm was obtained.

These scanners have been packaged inside 5-mm diameter endoscopes to enable *in vivo* imaging. Endoscopic OCT with transverse and axial resolutions of $15\mu\text{m}$ and $12\mu\text{m}$, respectively has been demonstrated at imaging speeds of 2 to 6 frames/second. TPEF and SHG imaging with imaging resolution greater than $1.5\mu\text{m}$ has been obtained. These results show the potential for the use of MEMS-based endoscopy for early-cancer detection.

CHAPTER 1 INTRODUCTION

Cancer is a leading killer disease worldwide, and it accounts for as many as one-quarter of deaths in the United States of America. For the year 2005, the American Cancer Society estimates 570,280 cancer deaths in the US, and expects more than 2 million new cancer cases to be diagnosed [1]. Although cancers in the breast, colon, rectum, cervix, prostate, skin and the oral cavity are readily treatable provided they are diagnosed at a pre-invasive stage, early lesions in these tissues are often almost impossible to detect without regular screening. A study has estimated that the 5-year survival rate of patients with these types of cancers can increase to 95% if the cancers are diagnosed during their localized precancerous stage [1]. Therefore, early detection of many of these precancerous lesions is essential in order to greatly reduce patient morbidity and mortality.

The goal of this research effort is to develop endoscopic imaging modalities that can detect and diagnose *in vivo* precancerous lesions. It is proposed to achieve endoscopic imaging through the use of miniature optical scanners packaged inside endoscopes. This chapter discusses the limitations of existing cancer diagnostic techniques and introduces a new cancer detection technique along with the objectives of the project.

1.1 Limitations of Conventional Cancer Diagnosis Methodologies

Cancer researchers have estimated that more than 85% of all cancers originate inside the epithelium layer that lines the internal surfaces of organs throughout the human

body [2]; therefore it is of paramount importance to develop methods that can diagnose cancers just below the tissue surface. The existing diagnosis of cancers is carried out through visual inspection of the tissue surface followed by random tissue biopsy. Internal organ cancer screening is conducted by using special biopsy endoscopes that are equipped with cameras for visually inspecting the internal organ tissue surfaces.* Since precancers originate below the tissue surface, conventional endoscopes that only image the tissue surface are unable to make an accurate diagnosis. Therefore, this current practice of white-light endoscopy often requires biopsies for *ex vivo* histological analysis and clinical diagnosis of suspect tissue. This biopsy procedure creates significant delay in clinical diagnosis, with the added risk and cost of the medical procedure. Another limitation is the biopsy tissue sampling density. A study performed by Reid *et al.* on the early detection of high-grade dysplasia in Barrett's esophagus proved that by reducing the tissue biopsy sampling interval from 2 cm to 1 cm, the success in detecting cancer was doubled [3]. However, even this practice of biopsy over-sampling suffers from substantial limitations since there is a practical limit in the number of biopsies that can be performed, thereby diminishing its diagnostic potential.

Imaging techniques such as radiography, computed tomography (CT), magnetic resonance imaging (MRI), and ultrasound allow noninvasive investigation of large-scale structures in the human body and also permit three-dimensional (3-D) visualization. However, the imaging resolution of these existing diagnostic techniques makes the detection and diagnosis of many precancers difficult if not impossible. For example, bronchial cancers are not commonly detected at curable stages since the precancerous

* Ali Fazel, M.D., Personal Communication, Gainesville, FL, 2004.

lesions are generally smaller than the detection limit of current imaging modalities. The spatial resolution of approaches such as conventional radiography, CT, and MRI is generally restricted to a few millimeters in standard clinical practice [4], thereby preventing the detection of lesions less than 1 cm in diameter [5].

However, for detecting cancer in its early stages, an imaging technology with a higher resolution ($< 20 \mu\text{m}$) is necessary for accurate diagnosis. In addition, clinical screening procedures such as the random biopsy procedure for the diagnosis of cancer can be improved by using a high-resolution, non-invasive imaging technique to identify biopsy sites that correspond to the most severe disease.

1.2 Emerging Optical Coherence Tomography

Optical coherence tomography (OCT) is an emerging diagnostic medical imaging technology that produces high-resolution, cross-sectional images of biological samples [6-8]. Optical coherence tomography combines the operating principles of ultrasound with the imaging performance of a microscope. It uses advanced photonics and fiber optics to focus an infrared light beam into a sample, and then uses low-coherence interferometry to measure the echo time delay of the reflected light to determine tissue microstructure. The OCT imaging depth is limited by optical attenuation from tissue absorption and scattering to about 2 to 3 mm. This is the same scale as that generally imaged using biopsy and histology. A very attractive feature of OCT imaging is the high resolution. Although ultrasound imaging has greater imaging depth, OCT has a much higher imaging resolution of $10 \mu\text{m}$ or less [9]. An OCT system with $1 \mu\text{m}$ axial resolution has also been demonstrated [10], which is about two orders of magnitude higher than that of standard ultrasound imaging. Even though high-frequency ultrasonic

imaging has been shown to obtain a resolution of about 10 μm [11], the simplicity of OCT systems permits a much lower hardware cost. Since OCT uses infrared light it is much safer to use than CT systems which use harmful x-rays. OCT imaging is minimally-invasive and has the potential to eliminate risky and time-consuming biopsy procedures; therefore it is also known as *optical biopsy*.

Optical coherence tomography has been proved to be clinically useful in the field of ophthalmology, and has great potential for use in cardiovascular, gastrointestinal and pulmonary imaging through the use of endoscopes and catheters [5, 12, 13]. Endoscopic OCT systems have been demonstrated to be able to detect *in vivo* cancers at a very early stage [14, 15]. For these internal organ applications, the imaging probe must be small, and fast image scanning is required. Various methodologies have been proposed to transversely scan the optical beam across the internal tissue surface. Some endoscopic OCT devices use a rotating hollow cable that carries a single-mode optical fiber, while others use a galvanometric plate or piezoelectric transducer, that swings the distal fiber tip to perform *in vivo* transverse scanning of tissue [12, 14, 16].

1.3 MEMS-based OCT

Micro-Electro-Mechanical Systems (MEMS) or Microsystem Technology (MST) is another emerging technology that makes miniature sensors and actuators through batch-fabrication micromachining processes. Micromirrors manufactured using this technology have been widely used for optical displays and optical switching [17, 18]. MEMS-based transducers have been also widely used by the automobile industry which uses accelerometers and other inertial sensors for deploying safety air-bags and other vehicle stability applications. The small size, fast speed and low power consumption of MEMS

mirrors make them ideal for use in an endoscopic OCT imaging probe. In fact, researchers have started to use MEMS mirrors for the transverse scanning of endoscopic OCT systems [19-23]. Xie *et al.* demonstrated a 5 mm diameter MEMS-based OCT endoscope that used a 1-D electrothermal mirror to scan the light beam onto the biological tissue [19]. By performing 1-D transverse scans of the tissue, high resolution cross-sectional 2-D images were obtained. Zara *et al.* also reported an endoscopic OCT system based on MEMS mirrors in 2002 [24], in which the MEMS mirror has large deflection angle but requires elaborate assembly. Tran *et al.* [25] and Herz *et al.* [26] demonstrated radial endoscopic-OCT imaging using MEMS micromotors packaged inside endoscopes that rotated a prism or mirror. More recently Fan *et al.* [22] and McCormick *et al.* [23] separately demonstrated 3-D endoscopic OCT imaging through the use of 2-D electrostatic micromirrors packaged inside fiber-optic endoscopes. However, the high voltages required for electrostatic actuation may be a concern due to electrical safety issues during internal organ imaging. Even though the electrothermal micromirrors used by Xie *et al.* [19] operate at low voltages, the large initial tilt angle of the mirror plate complicated the endoscope package design. Another limitation of all these existing micromirror-based OCT endoscopes is that their lateral resolution is restricted to a few tens of microns in order to provide the necessary millimeter-range depth of focus. These lateral resolutions are not sufficient since a much high lateral resolution ($< 10 \mu\text{m}$) is required for the detection of *in vivo* precancers. These issues regarding the use of existing MEMS scanners for OCT imaging will be discussed in greater detail in Chapters 2 and 3.

Proposed solution: In prior work, 1-D and 2-D electrothermal micromirrors with large rotation angles at low actuation voltages were designed for transverse scanning in OCT imaging [27-30]. However the unidirectional operation, non-stationary center of rotation and large initial tilt angle of these mirrors complicated device packaging and optical design. These issues can be resolved by using a novel microactuator design that uses two complementarily-oriented electrothermal actuators to keep the mirror parallel to the substrate, and these actuators also provide bi-directional scanning capability to the mirror. This actuator pair can also generate large, out-of-plane, piston motion at low actuation voltages ($< 15V$). MEMS devices using this novel microactuator design are referred to as large-vertical-displacement (LVD) microdevices. It is proposed to use micromirrors integrated with either one or two sets of LVD microactuators to perform 1-D or 2-D transverse scanning, respectively. The fabricated mirrors will be packaged inside endoscopes to perform OCT imaging. Also, further miniaturization of the overall OCT system is possible by replacing the bulky axial scanning mirror with a phase-only LVD micromirror. Figure 1-1 shows the schematic of a MEMS-based OCT system in which the LVD micromirror can be used for axial reference scanning as well as endoscopic transverse bi-directional scanning applications. Further details about the LVD micromirrors are provided in Chapter 4.

1.4 MEMS-based OCM

Optical coherence microscopy (OCM) is an extension of OCT imaging technique, and it allows for ultrahigh-resolution cross-sectional imaging of highly-scattering tissue by combining the imaging capabilities of OCT technology and high numerical-aperture (NA) confocal microscopy. In OCM, the high imaging resolution in the axial direction is provided by low-coherence interferometry, while the micron imaging resolution in the

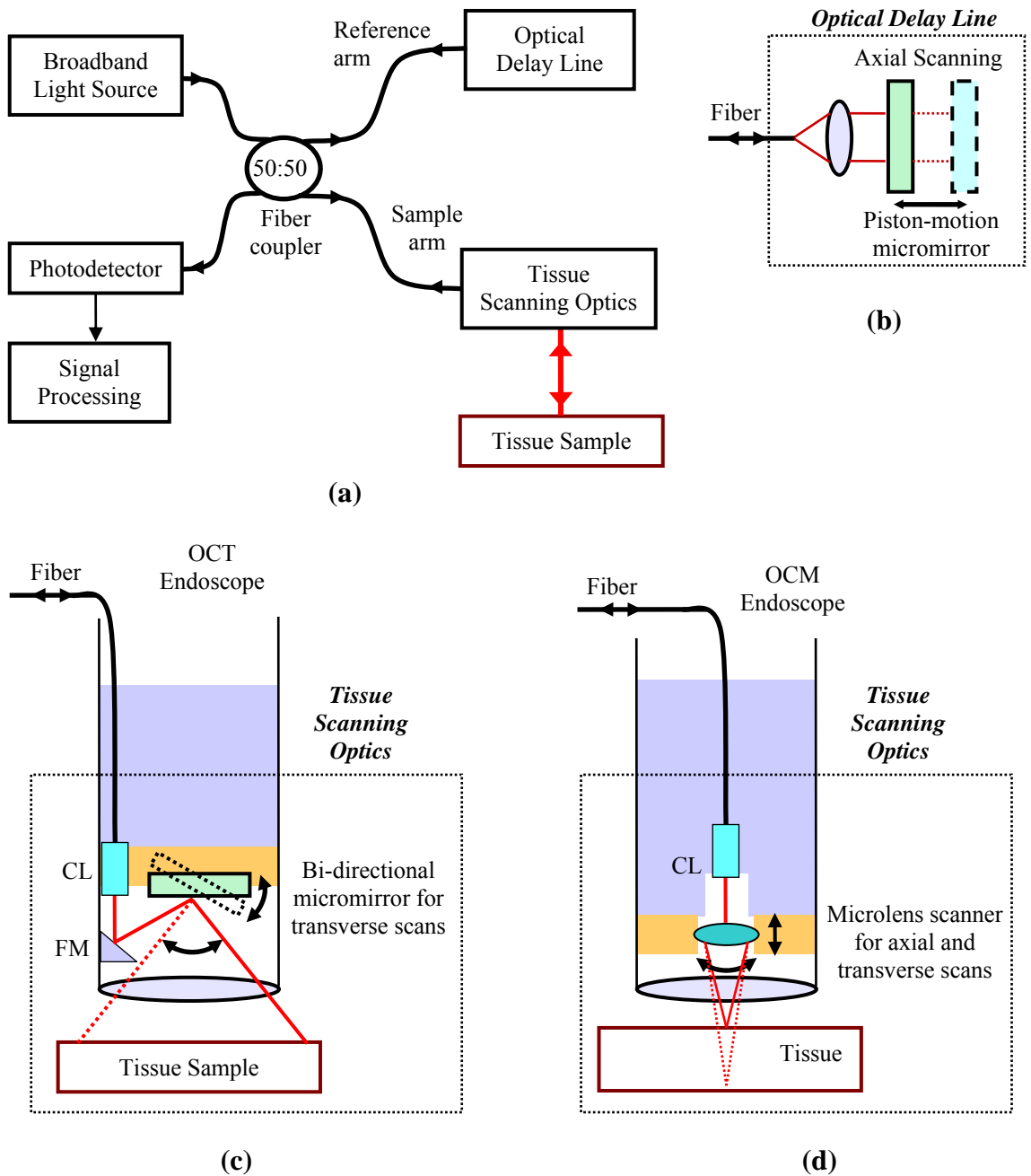


Figure 1-1: Schematic of a MEMS-based OCT/OCM system. (a) System block diagram. (b) Optical delay line that uses the LVD micromirror as a reference mirrors for transverse and axial scanning. (c) OCT endoscope that uses a 1-D or 2-D LVD micromirror for transverse scanning of tissue. (d) OCM endoscope that uses a LVD microlens for axial scanning of tissue. CL: collimating lens. FM: Fixed mirror.

lateral direction is provided by confocal microscopy. Bench-top OCM systems have demonstrated lateral imaging resolutions better than 3 μm [10], and thereby have the ability to detect precancerous lesions at the cellular level (similar to histology).

Therefore, in order to detect and diagnose precancers in internal organs, endoscopic OCM apparatus is highly desirable. Unfortunately, the high-NA optical components of OCM systems are bulky, therefore existing OCM systems are restricted to bench-top set-ups just like standard microscopes. Researchers have been investigating various methodologies to develop an endoscopic OCM system, and till date none have been reported in literature. Endoscopic OCM essentially requires a scanning mechanism which can vertically displace a highly-focused light spot by up to 2 millimeters inside tissue. Fitting a high-NA optical scanner that meets this requirement into a millimeter-scale endoscope has been a challenge.

Proposed solution: This project proposes to integrate a high-NA microlens with an LVD microactuator to form a LVD microlens scanner which can then be fitted into an endoscope for OCM imaging. This endoscopic OCM probe will then be used to obtain high-resolution images in both lateral and longitudinal directions. Since high lateral resolution results in a reduced depth-of-focus, the LVD microactuator will be used for vertically displacing the microlens in order to focus a light spot at different depths inside tissue. A schematic of an OCM endoscope is shown in Figure 1-1(d). The LVD microlens scanner design allows it to axially displace the focal plane of the scanning microlens by up to a few millimeters. These LVD scanners are appropriate for endoscopic OCM systems since the scanners are small enough to fit inside millimeter-sized endoscopes,

and also need low voltages for actuation. Details about MEMS-based OCM and LVD microlens scanners are presented in Chapter 5.

1.5 Research Objectives

The main goal of this research project is to develop miniature optical scanners for an endoscopic imaging modality that can detect and diagnose *in vivo* precancerous lesions. This main goal has been further subdivided into two approaches for this research effort. First, this work aims to extend and improve on the MEMS-based endoscopic OCT imaging technology developed by Xie [31], by developing novel reflective optical micro-scanners. The aim of this approach is to fabricate reflective scanners that are capable of providing large bi-directional optical scans ($>20^\circ$) at low actuation voltages (<20 V), and they also should be small enough to fit inside a 5-mm diameter endoscope. A two-dimensional optical scanner will also be developed in order to enable three-dimensional OCT imaging. These micromirrors can also be used with other endoscopic imaging techniques such as two-photon excitation fluorescence and second harmonic generation microscopy for *in vivo* visualization of precancers.

Secondly, this project aims to develop a MEMS-based OCM system which uses a refractive micro-scanner to provide ultrahigh resolution endoscopic imaging for the detection of early cancers. The objective of this approach is to develop microlens scanners which can focus a light beam at different depths inside biological tissue. This scanner should be capable of providing millimeter-range displacements at actuation voltages below 20 V, and should also be small enough to fit inside 5-mm diameter endoscopes. A prototype microlens scanner was initially developed to demonstrate proof-

of-concept, and this scanner design was then scaled to develop millimeter-scale scanners that meet the requirements of this project.

1.6 Dissertation Overview

This dissertation is divided into six chapters. The first chapter provides the motivation for this work and a background of current imaging methods used for the detection of cancer.

Chapter 2 provides the background information on three emerging biomedical imaging technologies that can perform *in vivo* detection of precancerous lesions. These include optical coherence tomography and microscopy, and nonlinear optical imaging techniques of two-photon excitation fluorescence and second harmonic generation. The required OCT scanning-probe characteristics for endoscopic OCT imaging are also explained.

Chapter 3 provides a comprehensive literature review of various MEMS micromirror design structures and their limitations for use in endoscopic OCT imaging systems. Electrothermally-actuated micromirror designs are also introduced and their principles of operation and fabrication process are explained in great detail. Endoscopic OCT imaging using these micromirrors is also demonstrated.

Chapter 4 presents a novel large-vertical-displacement (LVD) microactuator design that has the ability to perform bi-directional rotational motion as well as generate large vertical displacements. 1-D and 2-D LVD micromirrors using this actuator design are demonstrated. Nonlinear optical endoscopy using these devices is also presented.

In Chapter 5, a novel LVD microlens scanner design along with experimental results is presented. This microlens scanner will be used for endoscopic optical coherence microscopy (OCM) imaging, and has been packaged inside a 5-mm diameter endoscope.

Finally, Chapter 6 summarizes the entire research effort and lists suggestions for future work, along with a list of accomplishments for this project.

CHAPTER 2 OPTICAL BIOIMAGING METHODOLOGIES

2.1 Optical Coherence Tomography

Optical coherence tomography (OCT) is an emerging *in vivo* diagnostic medical imaging technology that produces high-resolution, cross-sectional images of biological samples [6-8]. Optical coherence tomographic imaging technology is an optical analogy of the more conventional ultrasonic pulse-echo imaging technology which measures the intensity and echo delay of acoustic waves to determine tissue microstructure. Since the speed of light is many orders of magnitude faster than that of acoustic waves, a direct measurement of optical echoes cannot be obtained electronically as in ultrasound imaging. Therefore OCT uses an optical measurement technique known as low-coherence interferometry to measure the optical delay information in the back-reflected signal from tissue. Low-coherence interferometry was initially developed and demonstrated for optical-coherence domain reflectometry (OCDR), a 1-D optical ranging technique used for locating faults in fiber optic cables [32-34]. Optical coherence tomography is based on the principles of low-coherence interferometry, and it uses advanced photonics and fiber-optics to image high-resolution cellular structure of tissues at depths greater than conventional microscopes. This section presents the operating principle of OCT imaging technology and also discusses the scanning probe requirements for endoscopic OCT imaging.

2.1.1 OCT System Design

The schematic of an OCT system is shown in Figure 2-1. The core of this system is a Michelson interferometer, which uses a broadband light source (BBS) to provide a low-coherence infrared light beam.

This low-coherence infrared light beam is split at a fiber coupler into the reference and sample arms of the interferometer. The light in the sample arm is focused onto the sample; and the reflected light containing time-of-flight information is collected by the same optical fiber. The reflections from the sample and reference arms are then combined at the coupler and their optical interference is detected by a photodetector.

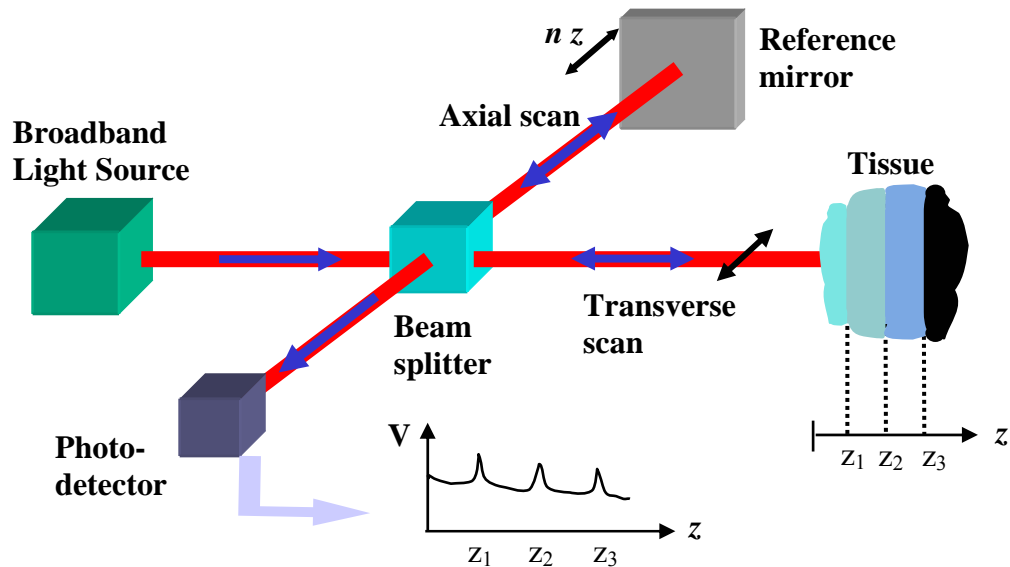


Figure 2-1: OCT schematic.

Optical interference is detected by the photodetector only when the optical path difference of the reference and sample arms is within the coherence length of the light source. That is, only the light reflected back from a particular depth of the sample is detected. This is called *coherence gating*. The amplitude of the interferometric signal (detected by the photodetector) provides a direct measure of the intensity of back-

scattered light from a tissue segment as thin as the coherence length of the BBS. Since OCT imaging provides tissue microstructure information pixel by pixel, scanning mechanisms are required to scan the tissue in axial and lateral directions. The depth information of the tissue sample is acquired through the axial (z -axis) scanning of an optical delay line (*i.e.*, the reference mirror in Figure 2-1), while the lateral information is obtained by transversely scanning the light beam in the sample arm of the interferometer. Multiple longitudinal scans are performed at different lateral locations to provide a two-dimensional data set which contains the back-scattering information of a tissue cross-section. This 2-D data is then displayed as a grayscale or false color OCT image. Since multiple longitudinal scans are performed at different lateral positions, this scanning mechanism is similar to the A-scan image scanning method used in ultrasound. *En-face* scanning is another method in which the tissue is transversely scanned at different longitudinal locations to generate a B-scan OCT image. A schematic of these scanning operations is shown in Figure 2-2.

Depending on the coherence length of the employed broadband light source, OCT can provide cellular or even sub-cellular resolutions (1~20 μm), which are one or two orders of magnitude higher than that of commonly used ultrasound imaging (~100 μm) [9]. Figures 2-3 and 2-4 show the difference in tissue image resolutions obtained using ultrasound and OCT technologies [9, 35].

Since more than 85% of all cancers originate in the tissue epithelial layer, which is within the penetration depth (a few mm) of infrared light [2, 36, 37], malignant or premalignant changes of epithelia can be detected at a very early stage without performing biopsies. Also by using OCT imaging along with conventional biopsy, highly

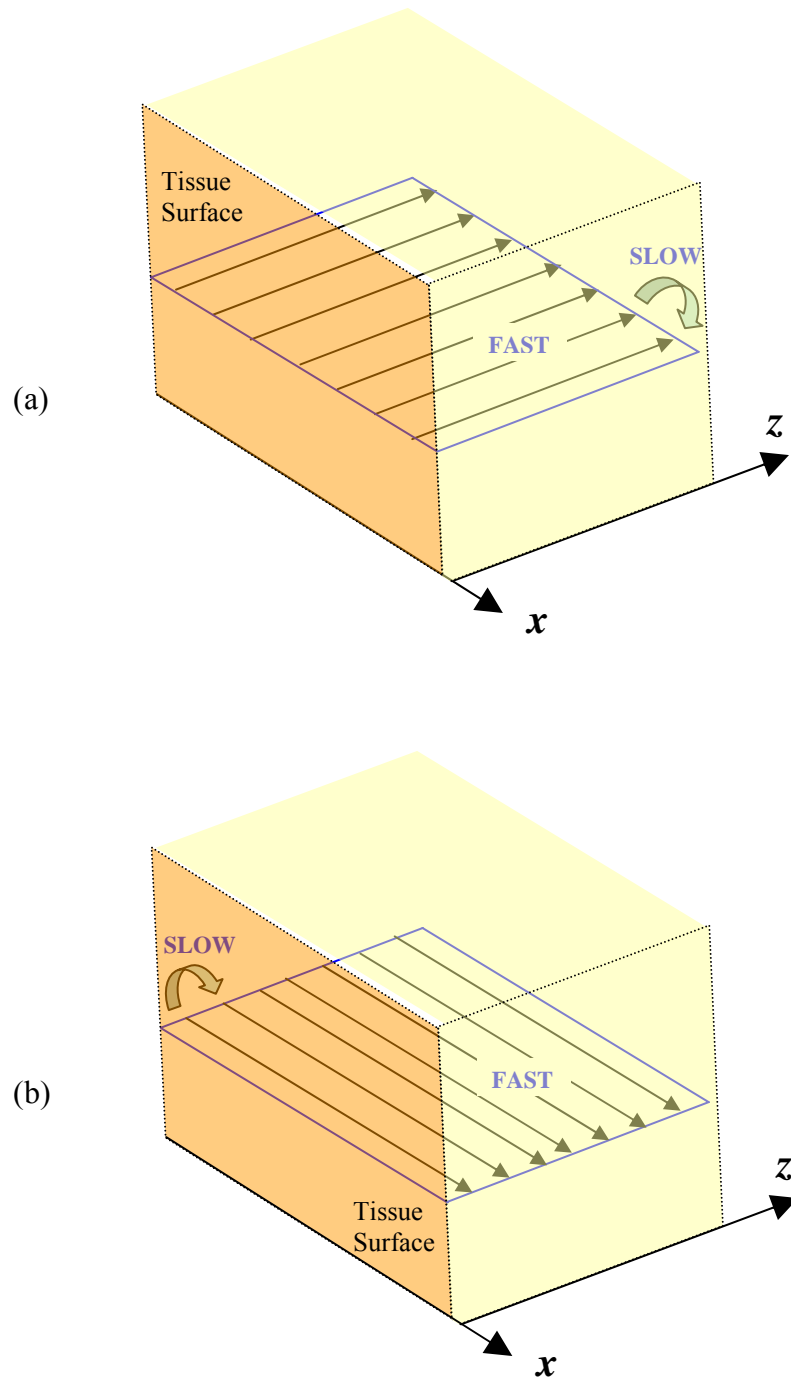


Figure 2-2: OCT tissue scanning modes. (a) Conventional longitudinal scanning (A-scan). (b) *En-face* scanning (B-scan). Adapted from Podoleanu *et al.* [38].

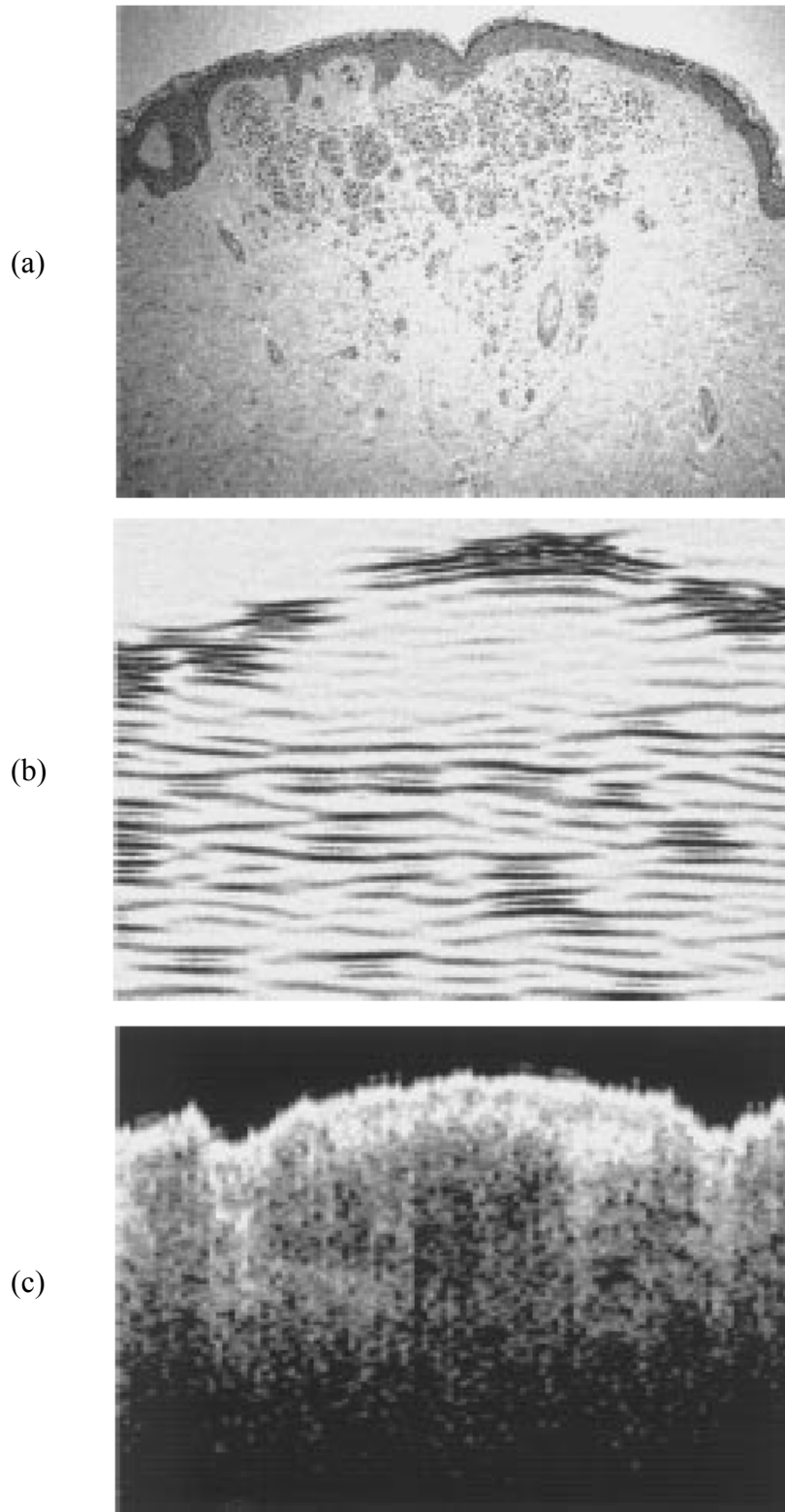


Figure 2-3: Comparison between histology, ultrasound and OCT images of biological tissue. (a) HE-stained histology, (b) 50-MHz ultrasound, and (c) OCT image of a nevus. © 1996 IEEE. Reprinted, with permission, from Pan *et al.* [35].

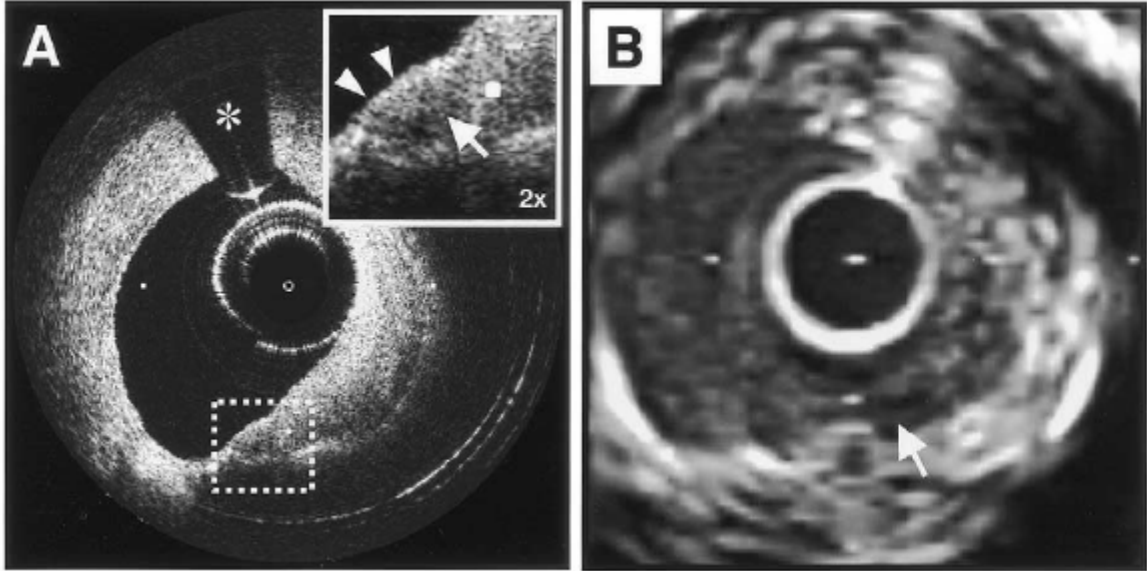


Figure 2-4: Comparison between ultrasound and OCT images of human coronary artery plaques. (a) *In vivo* OCT image with axial imaging resolution of $13\ \mu\text{m}$. (b) 30 MHz intravascular ultrasound image of the same artery with a lower resolution of $100\ \mu\text{m}$. Reprinted from Jang *et al.* [39], Copyright 2002, with permission from The American College of Cardiology Foundation.

suspicious tissue areas can be easily identified which can reduce the randomness of biopsies. Optical coherence tomography has been applied to a wide variety of biological tissue and organ systems including eyes, skin, teeth and gastrointestinal and respiratory tracts [5, 12, 14, 40-42]. Researchers have also demonstrated 3-D OCT imaging by 2-D lateral scanning of tissue [23, 42, 43].

2.1.2 Key Imaging Parameters

The performance of an OCT system is mainly determined by its axial and transverse imaging resolutions, dynamic range and also by its imaging speed. OCT achieves a very high axial resolution because the axial and lateral resolutions are independent of each other, unlike the case with conventional or confocal microscopy.

In OCT the axial resolution is determined by the coherence length of the broadband light source. For a light source with a Gaussian spectrum, the coherence length (l_c) in air

is given by [8]:

$$l_c = \frac{2 \ln(2)}{\pi} \frac{\lambda_0^2}{\Delta\lambda} \approx 0.44 \frac{\lambda_0^2}{\Delta\lambda} \quad (2-1)$$

where, λ and $\Delta\lambda$ are the center wavelength and the full-width at half-maximum (FWHM) spectral bandwidth of the light source, respectively. In order to obtain high axial resolution, a short temporal coherence length is desired, therefore, a light source with a broad emission bandwidth, i.e., a broadband light source (BBS) should be used. The BBS should operate in a spectral range that allows adequate penetration of light into tissue. Researchers have determined that BBS's that emit infrared light with a center wavelength between 1200 nm to 1800 nm achieve the deepest penetration in most tissues [44]. Another requirement for the BBS is that the irradiance of the emitted light should be high enough to provide a wide dynamic range. A wide dynamic range provides high detection sensitivity by enabling OCT imaging of weakly backscattering microstructures present deep inside the tissue.

As shown in Figure 2-5, the lateral resolution of an OCT system is determined by the spot-size of the focused optical beam on the tissue. The diameter of the focused spot-size of a Gaussian beam is given by:

$$\Delta x = \frac{4\lambda_0}{\pi} \frac{f}{D} \approx \frac{2\lambda_0}{\pi} \left(\frac{1}{NA} \right) \quad (2-2)$$

where, D is the diameter of the beam, NA is its numerical aperture, and f is the focal length of the lens. The lateral resolution of an OCT system is also affected by the depth of focus of the optical beam.

The depth of focus, also known as the confocal parameter or the Rayleigh range, of an optical beam is the longitudinal distance within which the optical beam is considered

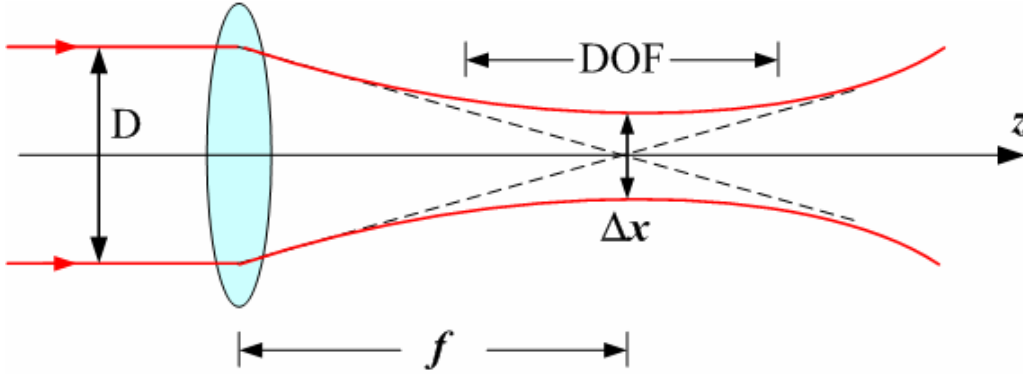


Figure 2-5: Gaussian beam optics.

to be in focus. The depth of focus (DOF) of a Gaussian beam is given by:

$$DOF = \frac{8\lambda}{\pi} \left(\frac{f}{D} \right)^2 = \frac{\pi}{2\lambda} (\Delta x)^2 \approx \frac{2\lambda}{\pi} \left(\frac{1}{NA} \right)^2 \quad (2-3)$$

This implies that a smaller spot-size will increase the lateral resolution but at the cost of reduced depth of focus. Since OCT imaging can penetrate tissue depths up to a few millimeters [36, 41], a depth of focus of a few millimeters is required. To overcome this depth of focus limitation, many researchers limit the numerical aperture of the scanning optics to obtain a DOF of approximately 1 mm [8]. At a center wavelength of 1300 nm, a lateral spot size of about 29 μm is achieved with a DOF of 1 mm. In order to improve lateral resolution without sacrificing depth of focus, some researchers have developed novel methods to scan the reference path-length and position of the focused sample optical-beam simultaneously [45, 46]. These methods that increase the lateral resolution without reducing the DOF will be discussed in Section 2.2.

The focal length of the scanning optics is of the same order of magnitude as the working distance between the OCT scanner and the tissue sample, which is typically a few millimeters. Therefore, by plugging in a focal length of a few millimeters in Equation (2-2), one can see that in order to obtain a lateral resolution better than 20 μm , the diameter of the optical beam on the scanning optics should be large (> 1 mm). This is

an important requirement to consider while designing optical scanners for endoscopic OCT imaging.

2.1.3 Internal Organ OCT Imaging

It is challenging to realize *in vivo* imaging of internal organs due to the size limitations of conventional OCT systems. Fiber optic endoscopes specifically designed for endoscopic OCT imaging are required for imaging internal organs. Some key factors that have to be considered for *in vivo* OCT imaging are endoscope sizes and imaging speed. Therefore for internal organ applications, miniature OCT imaging endoscopic probes with diameters of a few millimeters must be developed. Also the transverse scanning mechanism should be fast enough to provide real-time images.

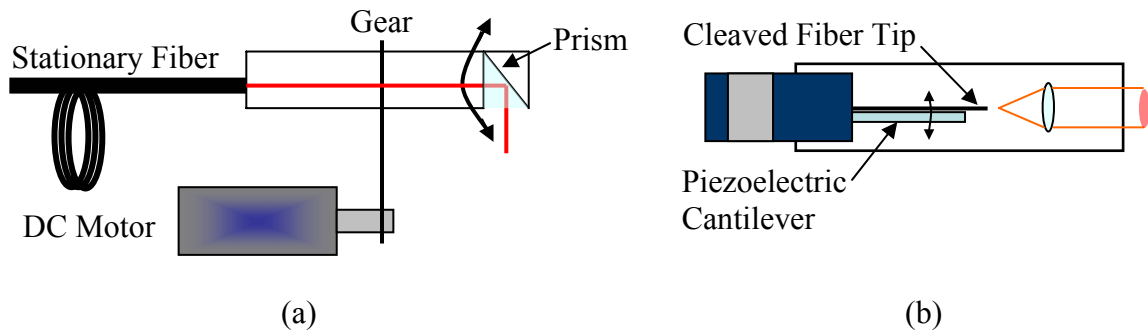


Figure 2-6: Existing endoscopic OCT probe designs.(a) Radial imaging probe design. Adapted from Li *et al.* [47]. (b) Forward imaging probe design. Adapted from Boppart *et al.* [16].

Various methodologies have been presented to transversely scan the optical beam across the tissue surface to obtain 2-D OCT images. Many researchers have demonstrated radial OCT scans by rotating a hollow cable that carries a single-mode fiber and a microprism [12, 13, 47, 48]. Bouma and Tearney used a galvanometer to linearly translate a optical fiber above the surface of *in vivo* tissue [49]. Sergeev *et al.* used a galvanometric plate to swing the distal fiber tip to perform transverse scanning [14].

Bopart *et al.* [16, 50] and Li *et al.* [16, 50] also demonstrated transverse scanning by swinging a cantilevered fiber tip, but by using piezoelectric methods. A schematic drawing of these types of endoscopes is shown in Figure 2-6. These existing methods are complex and use bulky components, thereby miniaturization of the endoscopic OCT system becomes difficult. Furthermore, rotating a fiber is slow and it also introduces complexities due to non-linear optical coupling. Therefore, it may be advantageous to replace these existing scanning mechanisms with a MEMS-based scanning solution to perform OCT imaging. This MEMS-based solution may also result in smaller probe sizes with faster scanning speeds, and at potentially lower cost.

The MEMS-based device should meet the following requirements for use in OCT probes:

Large scanning angle: A large scan angle should be provided by the device in order to image large tissue areas. Large scanning angle combined with fast scanning speed will also reduce the OCT imaging time.

Fast scanning speed: A fast scanning speed is desired to enable real-time OCT imaging, as well as to reduce the time required to conduct the endoscopic procedure.

Low operating voltage: Low voltage operation of the MEMS scanner is essential for electrical safety of the patient during internal organ imaging.

High resolution: The scanner should be able to provide lateral resolutions (spot sizes) better than a few tens of microns at working distances of a few millimeters.

Small size: Endoscope diameters should be smaller than a few millimeters, therefore MEMS devices should be small enough to fit inside. However, there exists a

trade-off between the small device size and high resolution requirements since a larger scanner size is needed for high spatial resolution.

The small size, fast speed and low power consumption of MEMS mirrors makes them an ideal choice for use in endoscopic OCT imaging probes. The micromirror must be large (~ 1 mm) and optically-flat to maintain high light coupling efficiency and spatial resolution, and should also have large angle of rotation to meet the scanning range requirements. In fact, OCT endoscopes using micromirrors actuated electrostatically or electrothermally, have already been reported in literature [24, 51, 52]. Using these systems two dimensional, high resolution, cross-sectional images were obtained.

As shown in Figure 2-1, 3-D OCT imaging requires 2-D transverse scanning. However, almost all existing OCT systems have only 1-D transverse scanning. In those cases, 3-D imaging is typically obtained by physically pulling the entire imaging probe. Since endoscopic catheters are flexible, the pull-out length may not be exactly the same as the physical displacement of the imaging probe. Therefore, there also exists a requirement for miniature scanners that can transversely scan the tissue surface in 2-D, thereby enabling endoscopic 3-D OCT imaging.

2.1.4 MEMS-based OCT

As discussed earlier in this section, the key to making compact OCT probes is to miniaturize the scanning mirrors. In fact, there are a few groups who are working on MEMS micromirror based OCT. Pan *et al.* assembled the first MEMS micromirror based endoscopic OCT system in 2001 [53]. Zara *et al.* also reported an endoscopic OCT system based on MEMS mirrors in 2002 [24], in which the MEMS mirror has large deflection angle but requires elaborate assembly.

Xie *et al.* reported a MEMS-based endoscopic OCT system that used a single-axis, single-crystal-silicon, electrothermal micromirror to scan the light beam onto the tissue [51]. Figure 2-7 shows a schematic of the MEMS-based OCT setup reported by Xie *et al.* [51], where the scanning micromirror along with the focusing optics was packaged inside a 5-mm diameter endoscope. The collimated light in the sample arm of the Michelson's interferometer is reflected off a beam steering 1-D micromirror and focused into the tissue. The same mirror collects the back-scattered light from the tissue, and the tissue microstructure is determined by low coherence interferometry. Two-dimensional (2-D) (*i.e.*, x - z) cross-sectional images are obtained by combining the transverse scanning of the 1-D micromirror in the x -direction with the axial scanning of the reference mirror in the z -direction, as shown in Figure 2-7. This MEMS-based system acquired OCT images at a rate of 5 frames per second, thereby demonstrating the potential for real-time clinical diagnosis of cancers. Since the micromirror is packaged inside a flexible endoscope, no mechanical movement of the endoscope is necessary for OCT imaging.

Other researchers have also used MEMS-based solutions to address the transverse scanning requirements of endoscopic OCT systems. Qi *et al.* used a MEMS deformable mirror to tune the focus of the OCT objective lens [54]. Tran *et al.* demonstrated an endoscopic OCT catheter using a MEMS micromotor to rotate a prism [25], while Herz *et al.* used a MEMS micromotor to rotate a mirror [26]. However, all these efforts are focused on only transverse scanning in one direction. 3-D OCT images can be obtained by using a MEMS scanner that can transversely scan the tissue in the x - y plane, *i.e.*, in two dimensions. Yeow *et al.* demonstrated 3-D OCT imaging by using a 2-D electrostatic

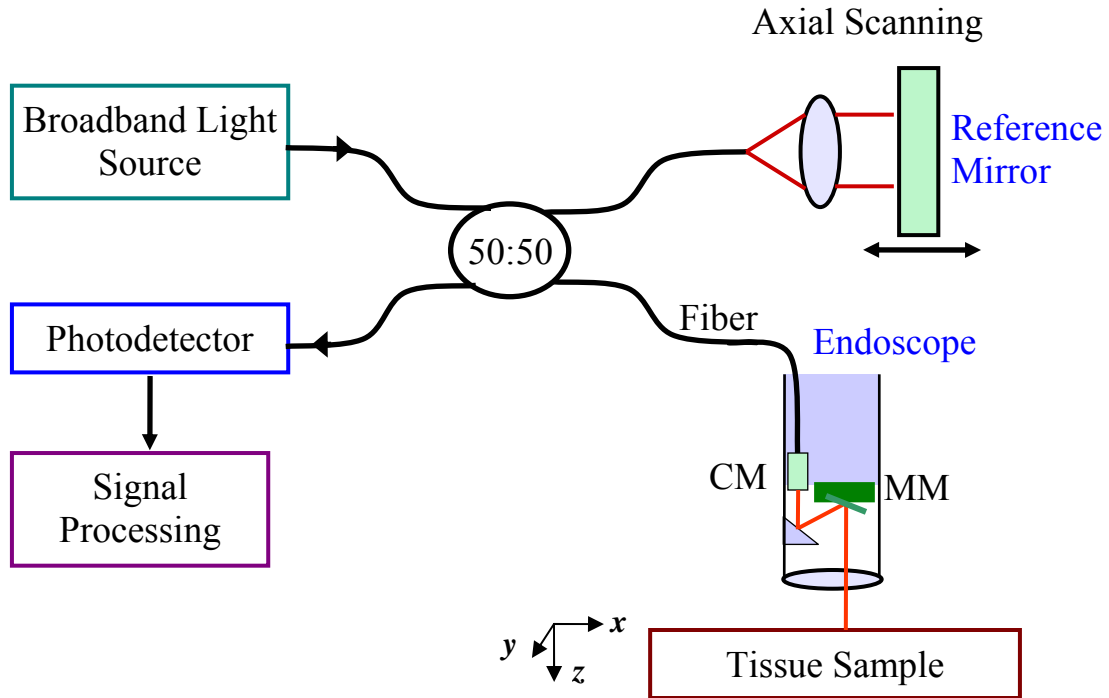


Figure 2-7: MEMS-based endoscopic OCT system. MM: Micromirror. CM: Collimator.

micromirror that scanned angles smaller than $\pm 0.5^\circ$ in both transverse directions [21]. Fan *et al.* packaged a 2-D electrostatic micromirror inside a 5-mm diameter endoscope for *in vivo* OCT imaging [22]. McCormick *et al.* also demonstrated 3-D endoscopic OCT imaging using a 2-D scanning MEMS micromirror that used electrostatic actuation [23]. However, the high voltages required by electrostatic actuation for the abovementioned scanners may be a concern due to electrical safety issues during internal organ imaging.

MEMS mirrors will be discussed in detail in the next chapter.

2.2 Optical Coherence Microscopy

As discussed in the previous section, the lateral resolution of an OCT system was restricted to a few tens of microns due to the millimeter-range depth-of-focus requirement for the scanning optics. This low lateral imaging resolution was due to the use of focusing optics with relatively low numerical apertures (NA). Researchers have demonstrated

various OCT system architectures that use high NA optics to obtain high-lateral resolution images without sacrificing the required depth of focus [10, 45, 46, 54, 55]. Figure 2-8 illustrates some of these different scanning approaches. Drexler *et al.* demonstrated a bench-top OCT system that used an x - z scanning stage to traverse the tissue sample in the transverse and axial directions to perform OCT imaging with resolutions better than $3\ \mu\text{m}$ [10]. The depth of focus of their imaging optics was less than $100\ \mu\text{m}$, therefore nine separate OCT images were fused together to form a millimeter-deep ultrahigh-resolution tomogram. Other researchers have developed novel methods to scan the reference path-length and the position of the focused sample optical-beam simultaneously, thereby improving lateral resolution without sacrificing the depth of focus [45, 46]. Schmitt *et al.* placed the reference scanning mirror and the focusing optics on the same movable stage, which allowed the use of lenses with high NA [45]. Since these modified OCT systems use high NA optics to obtain OCT images with high lateral resolutions ($< 10\ \mu\text{m}$), they are also referred to as optical coherence microscopes.

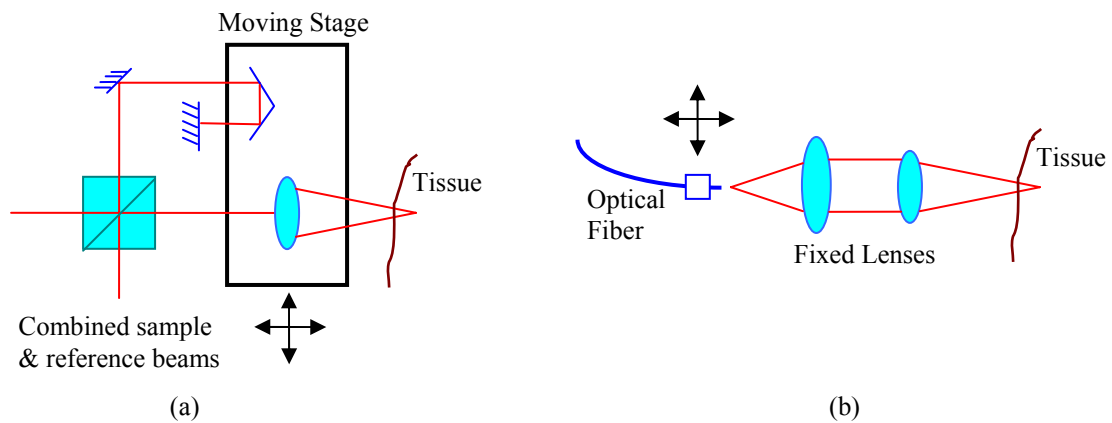


Figure 2-8: High NA scanning approaches for OCT. (a) Reference mirror and focusing optics placed on a movable stage to achieve dynamic focusing. Adapted from Schmitt *et al.* [45]. (b) Lateral and axial scanning achieved by displacement of the fiber tip. Adapted from Schmitt [8].

2.2.1 Bench-Top OCM

Optical coherence microscopy (OCM) is an extension of OCT technology and it allows for ultrahigh-resolution cross-sectional imaging of highly-scattering tissue by combining the imaging capabilities of OCT and high NA confocal microscopy. In OCM, the high imaging resolution in the axial direction is provided by low-coherence interferometry, while the micron imaging resolution in the lateral direction is provided by confocal microscopy. Confocal microscopy is an optical technique that is used for imaging thin optical sections of relatively transparent tissue with very high resolution.

Researchers have demonstrated bench-top OCM systems that obtained imaging resolutions better than $10\ \mu\text{m}$ in both, the axial and transverse dimensions [56-58]. A schematic of an OCM system is shown in Figure 2-9. As seen in the figure, the OCM system architecture is similar to that of OCT systems, the only difference being the imaging methodology of the tissue scanning optics. Figure 2-10 shows the difference

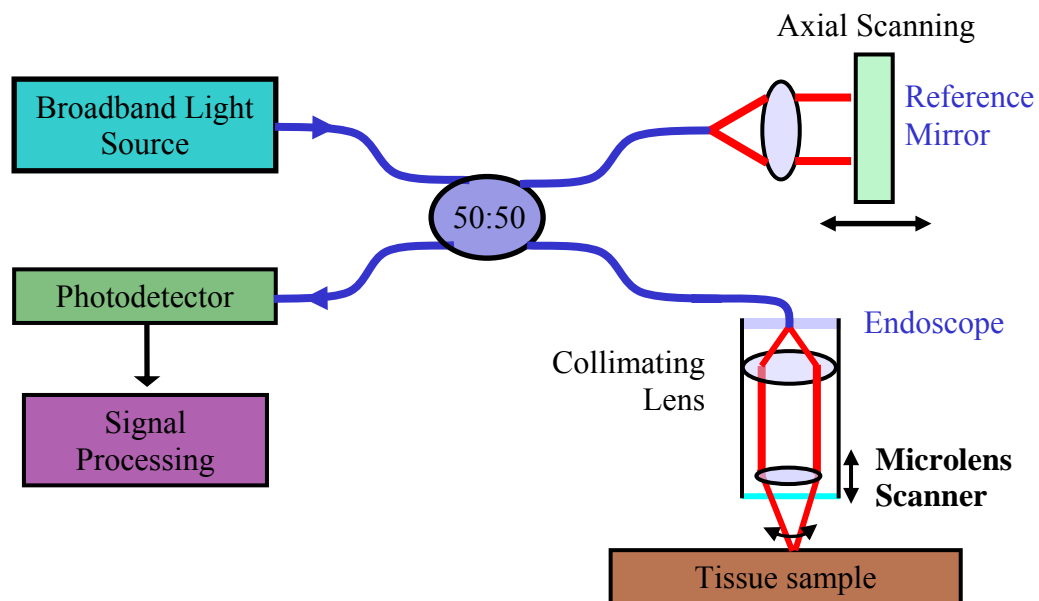


Figure 2-9: MEMS-based endoscopic OCM schematic.

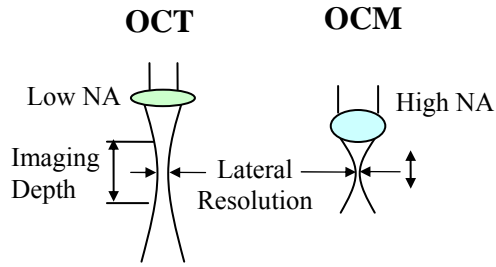


Figure 2-10: Difference between OCM and OCT.

between OCM and OCT imaging methodologies. OCT relies on large depth of focus to obtain imaging depth at the price of low transverse resolution, while OCM uses higher NA lenses ($NA > 0.2$) to achieve high transverse resolution but with smaller imaging depth. The OCM imaging depth can be extended by using a moving lens or stage, as mentioned above. Figure 2-11 shows the tissue image acquired using an OCM system, demonstrating that cellular imaging is possible using this technology. Therefore, OCM technology is very promising for the early detection of cancer.

2.2.2 MEMS-based OCM

Although bench-top OCM systems allow for ultrahigh lateral and axial resolutions, endoscopic OCM probes with ultrahigh imaging resolutions are needed for *in vivo* detection of precancers in internal organs. Since the methods shown in Figure 2-8 require the use of mechanical stages with stepper motors, they are bulky and slow, and therefore cannot be used for ultrahigh-resolution endoscopic OCM imaging. A MEMS-based dynamic focusing micromirror has been proposed by Qi *et al.* that could potentially be used for endoscopic OCM [54]. They demonstrated a MEMS deformable mirror to focus a high NA objective lens at different depths inside biological tissue. However their micromirror requires a high ac voltage of 400 V (peak to peak) to produce a 1.25-mm focus scan range. Ding *et al.* used an axicon lens to obtain OCT images with a lateral

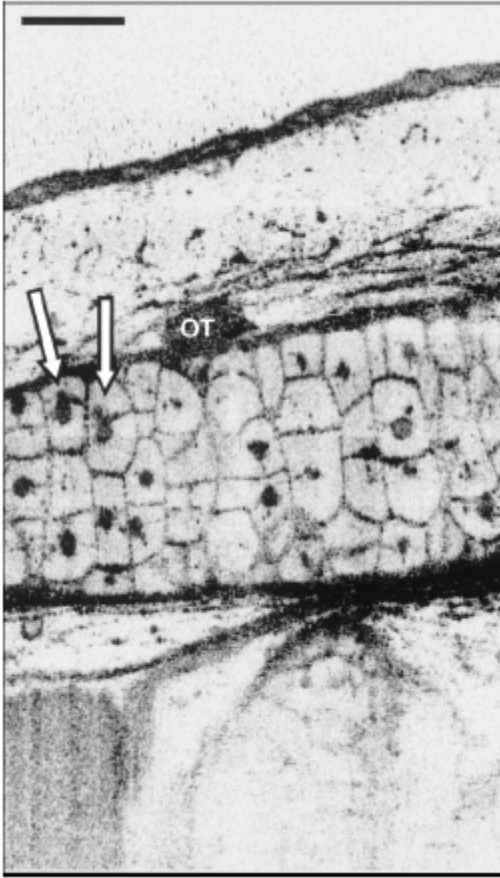


Figure 2-11: 1- μm axial resolution by 3- μm lateral resolution tomogram of a tadpole. Reprinted, with permission, from Drexler *et al.* [10].

resolution of 10 μm with a depth of focus of 6 mm [59]. However, the axicon lens significantly reduced the optical signal intensity, which will result in a lower sensitivity for the OCT system. Kwon *et al.* demonstrated a microlens scanner for micro-confocal imaging that used electrostatic vertical-comb-drives; however its vertical scan range is restricted to less than 55 μm and therefore unsuitable for OCM imaging [60-62].

In order to obtain high lateral resolution without compromising the axial scanning range and small size requirement of endoscopic OCM systems, a MEMS microlens can be used to scan along the optical axis. This MEMS scanner should be able to axially displace the focal plane of the scanning microlens by up to a few millimeters. Other requirements are that the scanner should be small enough to fit inside millimeter-sized

endoscopes, and it should also use low voltage for actuation. A schematic of a MEMS-based OCM system is shown in Figure 2-9. The overall system design is similar to the MEMS-based OCT system architecture presented in Section 2.1.4. Infrared light in the sample arm of the Michelson interferometer is first collimated by a GRIN lens placed inside the hollow endoscope. Then the collimated light is focused by a high NA polymer microlens into the tissue, as shown in Figure 2-9. In this OCM scanner design, the polymer microlens is attached to a MEMS microactuator, which enables vertical displacement of the microlens. A vertical displacement of the microlens results in vertical displacement of the focused beam-spot inside the tissue. By changing the vertical position of the focused beam-spot, it is possible to scan axially into the tissue. Since a high NA microlens is used, this system will provide OCM images with high lateral resolution. Unlike the axicon lens used by Ding *et al.* [59], the smaller depth of focus of the polymer microlens will maintain a strong optical signal intensity, which will help to improve the overall OCT system sensitivity.

2.3 Non Linear Optical Imaging

The imaging methods described in the preceding sections were linear optical imaging methods, since the magnitude of the observed signals from tissue changes linearly with incident light intensity. The well-known optical phenomena of reflection, refraction, and diffraction occur in the linear domain since the intensity of reflected, refracted or diffracted light changes linearly with the magnitude of the incident light. Other naturally occurring linear events are the absorption of light and photochemical reactions such as in the photosynthesis process in plants and bacteria [63].

This section introduces another class of imaging modalities that use the nonlinear optical properties of tissue for high-resolution imaging. The nonlinear optical imaging

modalities presented in the following sections have the potential to detect and diagnose *in vivo* cancers at a very early stage.

2.3.1 Two-Photon Excitation Fluorescence Imaging

Two-photon excitation fluorescence (TPEF) microscopy is a nonlinear optical imaging technique which can provide high resolution imaging at the cellular level. TPEF microscopy is a new form of scanning far-field fluorescence optical microscopy. Far-field fluorescence optical microscopy is typically a one-photon excitation fluorescence based microscopy technique, in which illumination is focused into a diffraction-limited spot scanned on the tissue specimen, thereby confining the excitation focal region. The diagram in Figure 2-12(a) depicts the phenomena of fluorescence when a single photon is absorbed by a fluorescent molecule, and so the molecule is excited to a higher energy state. The excited molecule now returns to its ground energy state by emission of a fluorescent photon at a characteristic wavelength. As seen in Figure 2-12(a), the energy of the fluorescing photon is less than the energy of the excitation photon, therefore the fluorescence emission is shifted towards a longer wavelength than that used for excitation. This means that in order to obtain fluorescence from samples that exhibit fluorescence in the blue-green wavelengths (~ 450 nm), the sample would have to be excited at a lower ultraviolet (UV) wavelength of about 350 nm. However, exciting tissue samples at UV or blue wavelengths is undesirable due to problems due to photobleaching and phototoxicity [64]. Another problem with one-photon excitation is that the entire thickness of the sample within the hourglass-shaped region of the focused light spot is excited, which results in poor optical sectioning ability. This is shown in Figure 2-13(a).

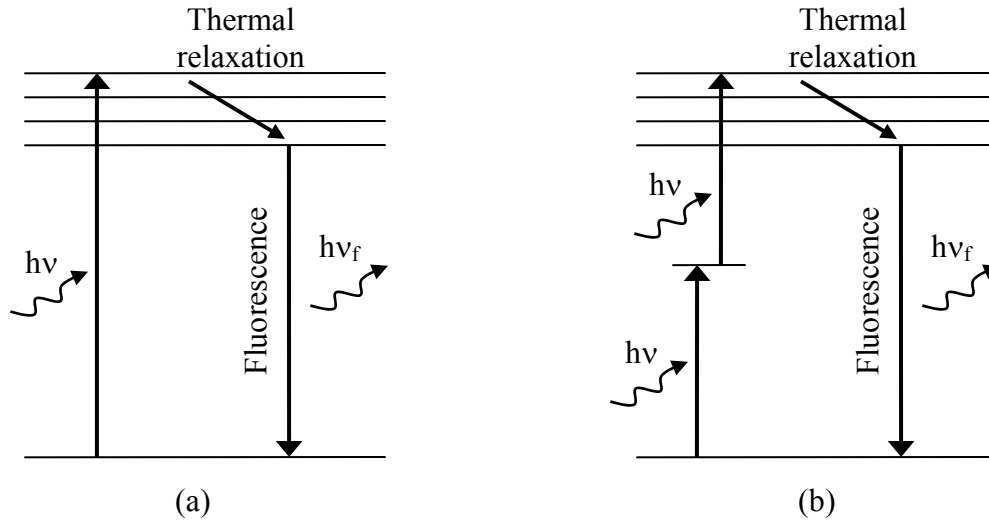


Figure 2-12: Energy band diagrams illustrating (a) one photon and, (b) two photon excitation fluorescence phenomena.

Two-photon excitation fluorescence (TPEF) microscopy provides an inherent optical sectioning ability to improve axial imaging resolution, and it is also less affected by the effects of photobleaching and phototoxicity. For two-photon excitation to occur, the fluorescent molecule should simultaneously absorb two photons of a longer wavelength to reach its excited state. As shown in Figure 2-12(b), two photons with lower energy are simultaneously absorbed to provide the energy needed to prime the fluorescence process. The fluorescent molecule now emits a single photon of fluorescence as if it were excited by a single higher energy photon. This phenomenon of TPEF depends on two photons interacting simultaneously with the molecule, and it results in a quadratic dependence on the intensity of incident excitation light. In contrast, conventional fluorescence is linearly dependent with the excitation light intensity. The reason that TPEF is referred to as a nonlinear imaging method is due to the fact that the rate of occurrence depends nonlinearly on the incident light intensity. Since light intensity is the highest at the focal spot, the largest probability of observing TPEF is at

this location. Axially away from the focal plane, the TPEF probability drops off rapidly with decreasing light intensity. As seen in Figure 2-13(b), no significant amount of fluorescence is emitted from regions away from the focal plane, and this demonstrates TPEFs' inherent optical sectioning ability. Therefore, TPEF microscopy can image tissue with very high resolution in all three dimensions.

TPEF theory: The probability, p that a molecule absorbs two photons simultaneously to reach its excited state has been computed as [64]:

$$p \propto KI^2 \quad (2.4)$$

where, K is a proportionality factor, and I is the intensity of the incident laser beam. The timescale for the keyword 'simultaneous' for TPEF is the same timescale of molecular

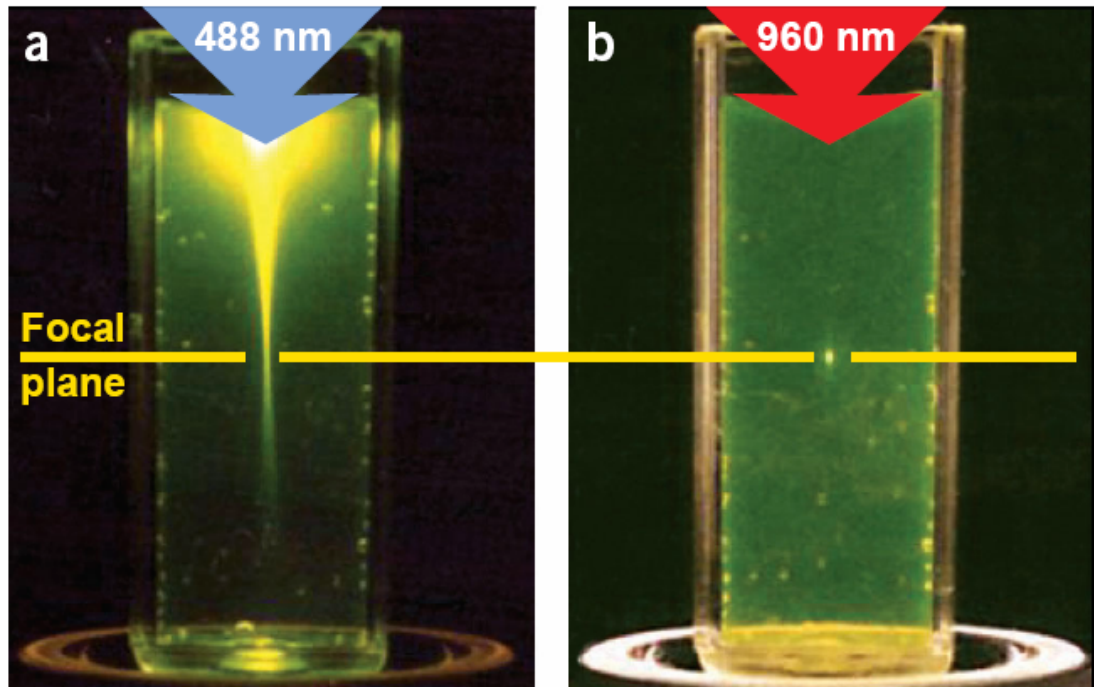


Figure 2-13: Optical sectioning ability of TPEF imaging. (a) Single-photon excitation of fluorescein by 488 nm light. (b) Two-photon excitation using 960 nm light. Reprinted by permission from Macmillan Publishers Ltd: Nature Biotechnology, Zipfel *et al.* [65], copyright 2003.

energy fluctuations at photon energy scale, and using Heisenberg's uncertainty principle this has been computed to mean a temporal window of 10^{-16} s or 0.1 fs [64]. The emitted fluorescence intensity, $I_f(t)$ from the molecule is proportional to the molecular cross-section δ , and also to the square of the incident intensity $I(t)^2$ [64]:

$$I_f(t) \approx \delta \cdot I(t)^2 \approx P(t)^2 \delta \left(\frac{NA^2}{2\hbar c \lambda} \right)^2 \quad (2.5)$$

where, $P(t)$ is the optical power of the incident light, c is the speed of light, \hbar is the Planck quantum of action, δ is the two-photon absorption cross-section, and NA is the numerical aperture of the focusing objective. The time averaged fluorescence intensity emitted from a fluorophore when excited with a pulsed laser beam with pulse width τ_p , repetition rate f_p , and average power P_0 can be computed from Equation (2.5) as:

$$\langle I_{f,p}(t) \rangle = \frac{P_0^2 \delta}{\tau_p f_p} \left(\frac{NA^2}{2\hbar c \lambda} \right)^2 \quad (2.6)$$

The number of photons absorbed by a fluorophore per pulse is given by [66]:

$$n_a \approx \frac{P_0^2 \delta}{\tau_p f_p^2} \left(\frac{NA^2}{2\hbar c \lambda} \right)^2 \quad (2.7)$$

Equation (2.7) does not account for saturation effects, and was computed with the paraxial approximation assumption.

2.3.2 Second Harmonic Generation Imaging

Second harmonic generation (SHG) is also a nonlinear optical process, similar to TPEF, and it can be used for high resolution imaging of tissue microstructure. SHG converts an input optical wave into an output optical wave of twice the input frequency,

therefore this phenomenon is also commonly known as frequency doubling. This is the same process used to produce green light at a wavelength of 532 nm from a Nd-YAG laser operating at 1.06 μm [63].

Similar to TPEF, the probability of SHG is proportional to the square of the intensity of the incident excitation light. Thus, SHG imaging has the same intrinsic optical sectional ability as TPEF imaging. However, unlike TPEF, SHG is confined to imaging only highly polarizable materials that lack a center of symmetry. SHG imaging can be used for bioimaging purposes since biological materials can be highly polarizable and the cellular membranes contain SHG-active constituents which are asymmetrically distributed [67]. The second-harmonic light emitted from the noncentrosymmetric, highly polarizable material is exactly half the wavelength of the incident excitation light. Therefore, the SHG process within the nonlinear optical material converts two incident photons into one exiting photon at exactly half the wavelength (or twice the energy). As described in Section 2.3.1, in TPEF some of the incident energy of the photon is lost during thermal relaxation of the excited state (Figure 2-12(b)), but in the case of SHG, there is no excited state and so SHG is energy conserving and it also preserves the coherence of the incident laser light. Since SHG does not involve excitation of molecules, it should not suffer from photobleaching or phototoxicity effects (which limit the usefulness of fluorescence microscopy). Another advantage of SHG is that it uses excitation wavelengths in the near-infrared range which allow for excellent depth penetration, thereby permitting imaging of thick tissue samples [68].

SHG theory: The nonlinear polarization for a material can be expressed as [68]:

$$P = \chi^{(1)} \otimes E + \chi^{(2)} \otimes E \otimes E + \chi^{(3)} \otimes E \otimes E \otimes E + \dots \quad (2-8)$$

where, P is the induced polarization vector, E represents the electric field vector, $\chi^{(i)}$ is the i th order nonlinear susceptibility tensor, and \otimes represents a combined tensor product and integral over frequencies. The first term in the series, $\chi^{(1)}$ describes normal absorption and reflection of light. The second term describes the sum and difference frequency generation; and thereby also describes SHG. The third term describes two-photon absorption (the probability of which is linearly proportional to the imaginary part of the third-order nonlinear susceptibility tensor), as well as third harmonic generation and coherent anti-Stokes Raman scattering. The portion of the polarization that contributes to SHG is:

$$P^{(2)} = \chi^{(2)} \otimes E \otimes E \quad (2-9)$$

The intensity of the SHG signals, I_{SHG} emitted from such materials will scale as follows [68]:

$$I_{SHG} \propto P_0^2 \tau (\chi^{(2)})^2 \quad (2-10)$$

where P_0 and τ are the laser pulse energy and pulse width, respectively. This term shows the nonlinear dependence of the SHG emission intensity to the incident light intensity.

2.3.3 Nonlinear Optical Imaging System Design

The schematic of a nonlinear optical imaging system is shown in Figure 2-14. The light source generally consists of a pump laser and a Ti:Sapphire laser which generates ~100 femtosecond long laser pulses at around 1W power at a repetition rate of 80 MHz. A laser pulse train output of such a laser system is depicted in Figure 2-15. This laser light is focused by a microscope objective lens and scanned laterally on the tissue sample using an XY beam scanner. In a fluorescence microscopy system, the dichroic mirror is used

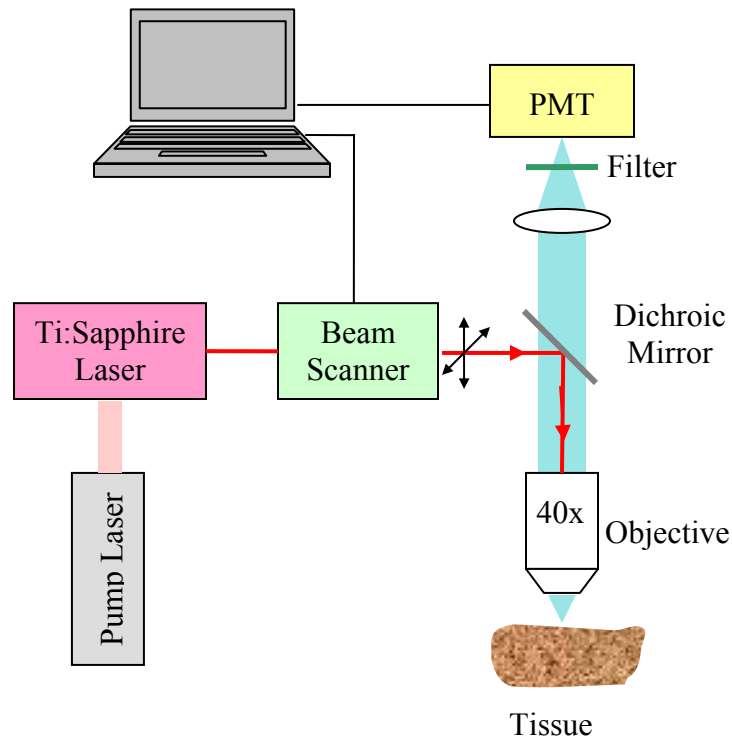


Figure 2-14: Schematic of a nonlinear microscope.

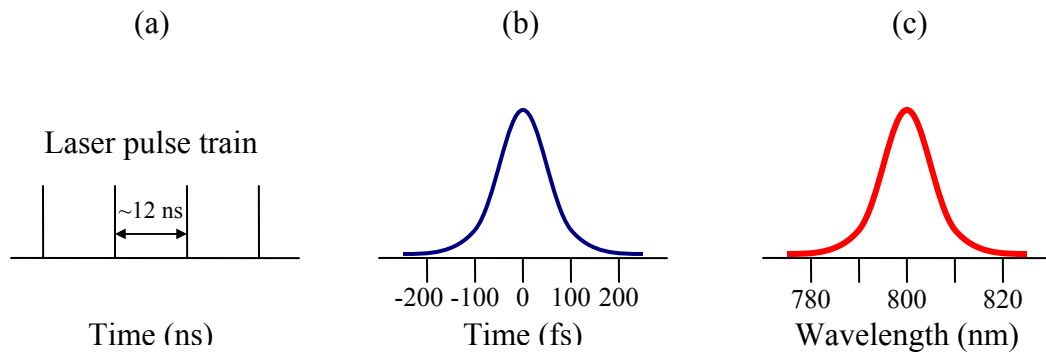


Figure 2-15: (a) Pulse train from a mode-locked Ti:Sapphire laser at 80 MHz. (b) The laser pulses typically have a FWHM duration of 100 fs, and (c) a spectral FWHM bandwidth of ~ 10 nm. Adapted from Zipfel *et al.* [65].

for separating the excitation and emission light beams. This dichroic mirror reflects light with wavelengths longer than 800 nm, while it transmits light with shorter wavelengths. The emission signal from the tissue specimen is collected by the same focusing optics, passes through the dichroic mirror, and is detected by a photomultiplier tube (PMT) as

shown in Figure 2-14. A bandpass filter is inserted in the light path before the PMT to help differentiate between the TPEF and SHG signals. Figure 2-16 illustrates the SHG and TPEF emissions when excited with near-infrared light.

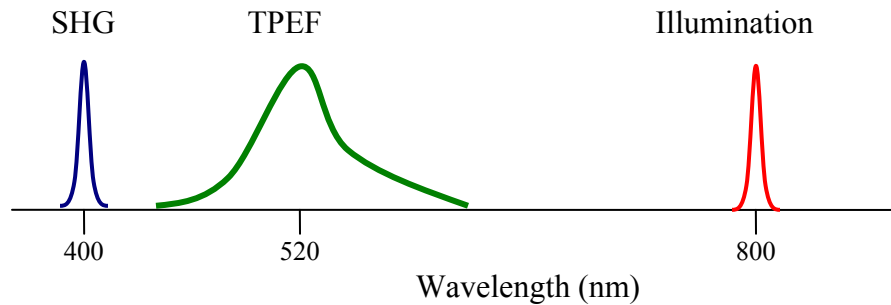


Figure 2-16: Two-photon fluorescence and SHG signals emitted by a sample excited by 800 nm light.

Researchers have used nonlinear optical microscopes to image and identify cancerous tissue with very high resolution as shown in Figure 2-17. The hamster cheek pouch biopsies were imaged using a bench-top system with lateral and axial imaging resolutions of 0.35 and 1.25 μm , respectively [69].

2.3.4 Endoscopic Nonlinear Optical Imaging

As stated in the previous section, researchers have successfully demonstrated high resolution imaging of tissue using bench-top nonlinear microscopes [69, Zipfel, 2003 #241]. However in order to demonstrate *in vivo* imaging, lateral beam scanning endoscopes are required.

Jung and Schnitzer developed a free-space multiphoton endoscope using GRIN lenses [70]; however, the lack of a flexible optical fiber prevents its use for endoscopic *in vivo* imaging. Helmchen *et al.* used a piezoelectric bending element to transversely scan a cantilevered fiber tip [71], but the 1.3-cm diameter, 7.5-cm long endoscope is too bulky

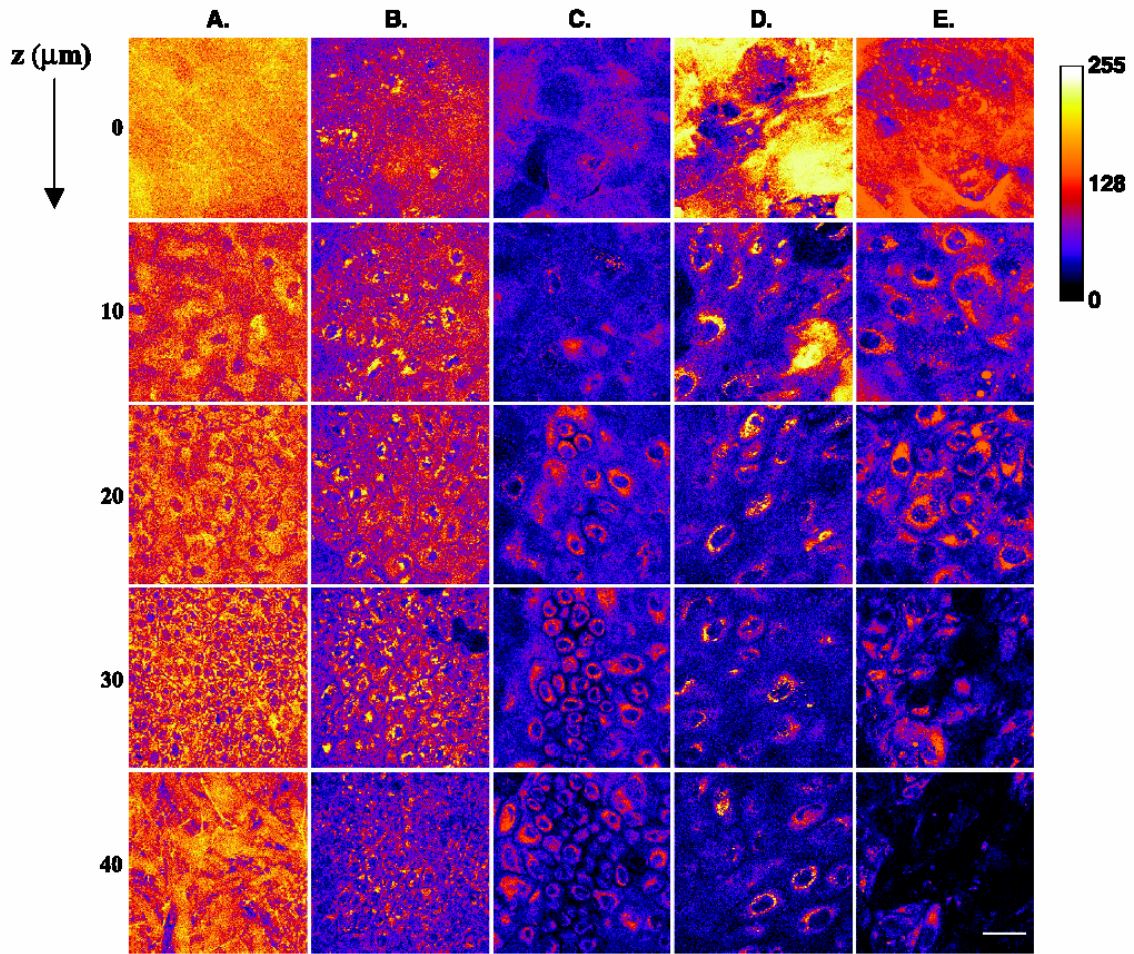


Figure 2-17: Two-photon imaging of the hamster cheek pouch tissue at an excitation wavelength of 780 nm. (a) Normal tissue. Precancerous tissue: (b) Moderate Dysplasia. (c) Carcinoma *in situ*. Cancerous tissue: (d) nonpapillary, and (e) papillary squamous cell carcinoma. The top image is at the surface of the tissue, and each subsequent image in the montage represents a 10- μm axial step. Scale bar represents 30 μm . Reprinted, with permission, from Skala *et al.* [69].

to be used for internal organ imaging. Flusberg *et al.* [72] also used a piezoelectric actuator, along with a MEMS micromotor, to create a multiphoton microscope designed for imaging peripheral organs of small animals. Gobel *et al.* demonstrated *in vivo* TPEF imaging using a fiber bundle and GRIN lens, but averaging and the use of a Gaussian blur filter were needed to improve image quality [73]. Bird and Gu developed a radially scanning endoscope, similar to the OCT endoscope design illustrated in Figure 2-6(a),

that required an external motor to physically rotate the endoscope [74]. Myaing *et al.* also adapted a piezoelectric OCT endoscope for *in vivo*, endoscopic TPEF imaging [75].

2.3.5 MEMS-based Endoscopic Nonlinear Optical Imaging

It is clear from the above discussion that the design requirements for TPEF endoscopes are almost the same as that for OCT endoscopes, which are listed in Section 2.1.3. The main difference being that the nonlinear imaging probes should be able to provide spot-sizes in the micron range, and should also be able to laterally scan higher power laser beams. MEMS-based scanners, packaged inside endoscopes with high numerical aperture optics, are very suitable for endoscopic nonlinear optical imaging as they can provide large scan ranges with high imaging resolution.

L. Fu *et al.* used the micromirrors developed by this research effort to demonstrate the first-ever MEMS-based nonlinear optical endoscopy system [76, 77]. Recently, Piyawattanametha *et al.* used an electrostatic micromirror to transversely scan the proximal end of a free-space, GRIN-lens endoscope [78]. The high voltage requirement (up to 160 V) of this MEMS scanner is a safety concern for *in vivo* internal organ imaging.

Ideally, the MEMS-based endoscopes should be capable of providing large scan range and high imaging resolution at a fast scan speed, but at low operating voltage. MEMS micromirrors are discussed in the next chapter, while the endoscopic TPEF and SHG imaging results obtained by this research effort are reported in Section 4.4.

CHAPTER 3 ELECTROTHERMAL MICROMIRRORS AND ENDOSCOPIC OCT IMAGING

As mentioned in the previous chapter, system miniaturization is the key for OCT to become practical for clinical use in imaging visceral organs. We can see from Figure 2-7 that the miniaturization of OCT imaging systems is largely determined by the axial scanning and transverse scanning mirrors. MEMS technology leverages integrated circuits (IC) technology to manufacture micro-scale devices and systems [79, 80], and thus is the natural choice to make scanning microdevices, i.e., MEMS micromirrors. This chapter introduces different types of MEMS micromirrors, and justifies the selection of electrothermal actuation as the preferred choice of micromirror actuation for internal organ OCT imaging probes. The basic operating principles, fabrication process and characterization results of 1-D and 2-D electrothermal micromirrors are presented. Finally, OCT imaging using these micromirrors packaged inside endoscopic probes is also demonstrated.

3.1 Scanning Micromirrors

Rotational scanning micromirrors are widely used for a variety of applications, such as optical displays [81, 82], biomedical imaging [20, 51, 83], barcode scanning [84, 85], optical switching [18, 86-88], and laser beam steering [85, 89]. There are numerous commercially available MEMS scanning micromirrors ranging from Texas Instruments' DMDs (Digital Micromirror Devices) [17] to Lucent Technologies' optical switch [18]. Most of these commercially-available micromirrors are surface micromachined and their size is limited to about 0.1 mm due to curling that is caused by residual stresses in thin-

film structures. For biomedical imaging applications, relatively large mirrors (>0.5 mm) are required to maintain high spatial resolution. Therefore, bulk-micromachining processes are often used to make relatively large, flat single-crystal silicon (SCS) micromirrors. These micromirrors can be actuated using electromagnetic, piezoelectric, electrostatic or electrothermal techniques.

Fast scanning speeds and low power consumption make electrostatically-actuated micromirrors the most popular amongst all scanning mirrors. Electrostatic micromirrors can be further subdivided into two categories based on electrode placement. The first type of mirror design uses the electrostatic force created by parallel-plate electrodes placed underneath the mirror to generate rotation. Micromirrors using this approach have demonstrated rotation angles of $\pm 8^\circ$ at 142 V [18], $\pm 7.5^\circ$ [90], and $\pm 7^\circ$ at 70 V [91]. Since most of these devices are fabricated using surface micromachining techniques, there is a trade-off between mirror-plate size and the maximum allowed rotation angle due to the small gap size between the electrodes. Other researchers have used bulk micromachining methods which achieve larger electrode gaps thereby permitting larger mirror sizes; but this significantly increases the actuation voltage. Parallel-plate actuation using bulk micromachining have yielded 2-D mirrors that rotate $\pm 5^\circ$ at 160-170 V [92], $\pm 5^\circ$ at 200 V [93], and $\pm 3^\circ$ at 40V [94].

Since the tradeoff between the mirror size and rotation angle limits the applications of parallel-plate electrostatic actuation to small micromirrors, a second category of electrostatic mirrors have been developed that use electrostatic comb fingers to rotate the mirror plate. A number of vertical comb drive (VCD) designs based on single-crystal silicon (SCS) have been reported for achieving larger rotation angles with large mirror

sizes [95-101]. For instance, Conant *et al.* reported a fast-scanning VCD micromirror by using silicon-on-insulator (SOI) wafers [96]. Xie *et al.* demonstrated a curled-hinge VCD micromirror that rotated $\pm 4.7^\circ$ at 18V [97]. Patterson *et al.* reported a VCD design in which photoresist re-flow was used to tilt comb fingers, but the device fabrication uniformity and yield may be concerns [98]. Krishnamoorthy *et al.* used SOI wafers to fabricate self-aligned VCD micromirrors [99]. Milanović *et al.* used lateral comb drives to generate torsional rotation [100, 101]. Kim and Lin reported an electrostatic micromirror with a pre-tilted mirror using localized plastic deformation of silicon by Joule heating [95]. 2-D electrostatic mirrors using comb drives have also been reported to produce mechanical rotation angles of $\pm 5.5^\circ$ at a resonance of 720 Hz and 16 V voltage [102], up to $\pm 11^\circ$ at 100 V [103], $\pm 6.2^\circ$ at 55 V [104], and $\pm 10^\circ$ at 140 V [101]. Although the high resonant frequencies of electrostatic mirrors allow for high speed scanning, the scan area is limited by the small rotation angles. Also, the high voltages required for larger angular actuation is a deterring factor for their use in certain applications, such as in endoscopes for internal biomedical imaging.

On the other hand, electrothermal actuation can generate large rotational displacements at low drive voltages. Electrothermally-actuated micromirrors use thin-film bimorph cantilevers (composed of materials with different coefficients of thermal expansion) that are attached to a mirror plate. Joule heating of these bimorph structures result in rotation of the mirror plate. Micromirrors based on the bending of bimorph or multimorph structures have been reported [51, 105-108]. Metals are often used as the top layer of bimorph structures due to their large thermal expansion coefficients and high reflectivity. The commonly used bottom layers include silicon dioxide [51, 105, 106,

108] and silicon [107, 109-111]. Heating sources can be provided by polysilicon [51, 105], diffusion [107], or metal resistors [106, 108]. 2-D electrothermal mirrors have reported mirror rotation of $\sim 15^\circ$ at a resonant frequency of 1.3 kHz [84], and also rotation angles as large as 40° at 15 V [30]. There is also an interesting report in which a clamped-clamped polysilicon beam was used as the thermal actuator [112]. In this case, the buckling of the clamped-clamped beam due to thermally-induced stress is used for actuation, and the polysilicon beam itself functions as a thermal resistor. The disadvantages of thermal actuation include high power consumption, relatively slow speed and poor temperature stability. Even though electrothermal micromirrors generally consume more electrical power than others, they are the best suited choice for some applications that require large optical angles at low driving voltages.

Electromagnetic micromirrors rotate due to the Lorentz force generated by the interaction of an external magnetic field with electric current flowing through a coil on the mirror plate. Electromagnetic micromirrors have been demonstrated using metallic coils [113-115] or magnetic materials such as Permalloy [116]. Although electromagnetic micromirrors can achieve large rotation angles of $\pm 10^\circ$ [86], $\pm 15.7^\circ$ [114], and 23° [87] at low actuation voltages, they are bulkier than other micromirrors since they require large external magnets. Therefore it is challenging to compactly package these electromagnetic micromirrors for applications with stringent size restrictions, such as endoscopic imaging.

Piezoelectric actuation is another mechanism that can generate large forces and have low power consumption and high bandwidth. In piezoelectric mirrors, mirror rotation is brought about by the piezoelectric bending of thin-film PZT actuators/cantilevers on application of an electric voltage. Piezoelectrically actuated

micromirrors with rotation angles of 2.3° at 4.5 V [117], 2.2° at 60 V [118], 3.5° at 40 V [119], and upto 5.5° at 16 V [88], have been reported. Even though some piezoelectric mirrors operate at low voltages, they are limited to the area they can scan. Other drawbacks of piezoelectric actuation include small displacements and charge leakage and hysteresis effects which often require a feedback control loop.

As mentioned in Chapter 2, micromirrors specifically designed for use inside endoscopic probes for internal organ biomedical imaging must meet requirements of small size, fast scanning speed, large scan angles, and low operating voltage. Electrothermal actuation was chosen as the preferred actuation method since it meets all the above mentioned requirements. The following sections present the fundamentals of electrothermal actuation, and also the fabrication process used to fabricate 1-D and 2-D micromirrors that use electrothermal actuation to achieve large angular displacements at low driving voltages for endoscopic optical coherence tomographic imaging.

3.2 Electrothermal Actuation and Design

All electrothermal micromirror designs described in this dissertation use the same basic design structure which is based on electrothermal bimorph actuation. A bimorph structure, illustrated in Figure 3-1, consists of two thin-film layers that have different coefficients of thermal expansion. A temperature change induces stress in the two layers due to the difference in their thermal expansion coefficients, thereby resulting in bending of the bimorph beam. This temperature change can be brought about by resistive Joule heating.

Although any two materials with different coefficients of thermal expansion can be used to form bimorph structures, their mechanical properties and material compatibility

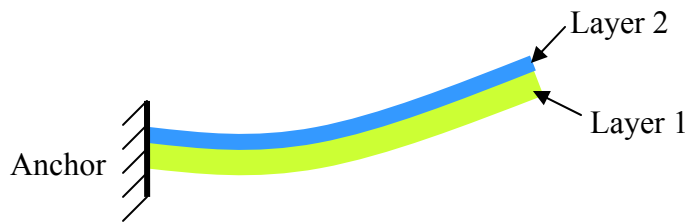


Figure 3-1: Side view of a bimorph beam.

must also be considered. Table 3-1 lists some materials that may be used in conjunction with others to form bimorph structures. Researchers have also reported bimorphs that were formed by a layer of metal and polyimide polymer [120, 121].

Table 3-1: Thermomechanical properties of some possible bimorph materials at room temperature.

Material	Coefficient of Thermal Expansion [10^{-6} /K]	Young's Modulus [10^{11} N/m ²]	Specific Heat [10^3 J/kgK]	Thermal Conductivity [W/mK]	Density [10^3 kg/m ³]
<i>Layer 1</i>					
Si	2.6	1.62	0.691	170	2.42
SiO ₂	0.4	0.74	0.84	1.1 [†]	2.66
Si ₃ N ₄	2.8	1.55	0.711 [†]	18.5	3.19 [†]
SiC	3.5	4.57		86.5	3.2
Poly-Si	2.3	1.60 [†]	0.754		2.33
<i>Layer 2</i>					
Al	23.0	0.69	0.9	235	2.692
Au	14.3	0.8	0.129	318	19.4
Pt	8.9	1.47	0.133	73	21.5
Cu	16.7	1.2	0.387	401	8.95
Ni	12.8	2.1	0.444	91	9.04
Pb	28.7	0.16	0.128	35	11.48

Material properties obtained from [110], and those marked [†] obtained from Memsnet.org

All electrothermal MEMS devices presented in this dissertation are fabricated using a CMOS-MEMS process [122], therefore bimorph actuators are composed of silicon dioxide (SiO₂) and aluminum (Al) thin-film layers which are provided by the CMOS process. As given in Table 3-1, the coefficients of thermal expansion for SiO₂ and Al are $0.4 \times 10^{-6}/\text{K}$ and $23 \times 10^{-6}/\text{K}$, respectively. It is this large difference in the thermal expansion coefficients of the two materials that attributes to the large actuation range of the fabricated MEMS optical scanners.

The basic structure of an electrothermal micromirror is shown in Figure 3-2. It consists of a mirror plate attached to the substrate by a bimorph beam actuator. The mirror plate is composed of an Al top layer which forms broadband, highly reflective surface of the mirror, a single-crystal silicon (SCS) membrane bottom layer which adds stiffness to the mirror to ensure surface flatness, and a SiO₂ layer in between the Al and SCS layers. The bimorph actuator is composed of a top aluminum layer, a bottom silicon dioxide layer, and within the SiO₂ layer is embedded an electrically-resistive polysilicon layer to provide Joule heating. A unique micromachining process which can be used to fabricate the bimorph structure shown in Figure 3-3 is detailed in the next section.

3.3 Microfabrication Process

It is a widely known fact that thin-film deposition processes generate residual stress and stress gradients, which cause curling of the resultant thin-film microstructures. Micromirrors made up of thin-film layers are typically small in size, in order to reduce their optical quality degradation due to curling. Therefore, this thin-film curling limits the useful size of micromirrors to about 10-100 μm . In order to increase mirror sizes without sacrificing the mirror flatness, single-crystal silicon (SCS) based mirrors are desirable. As

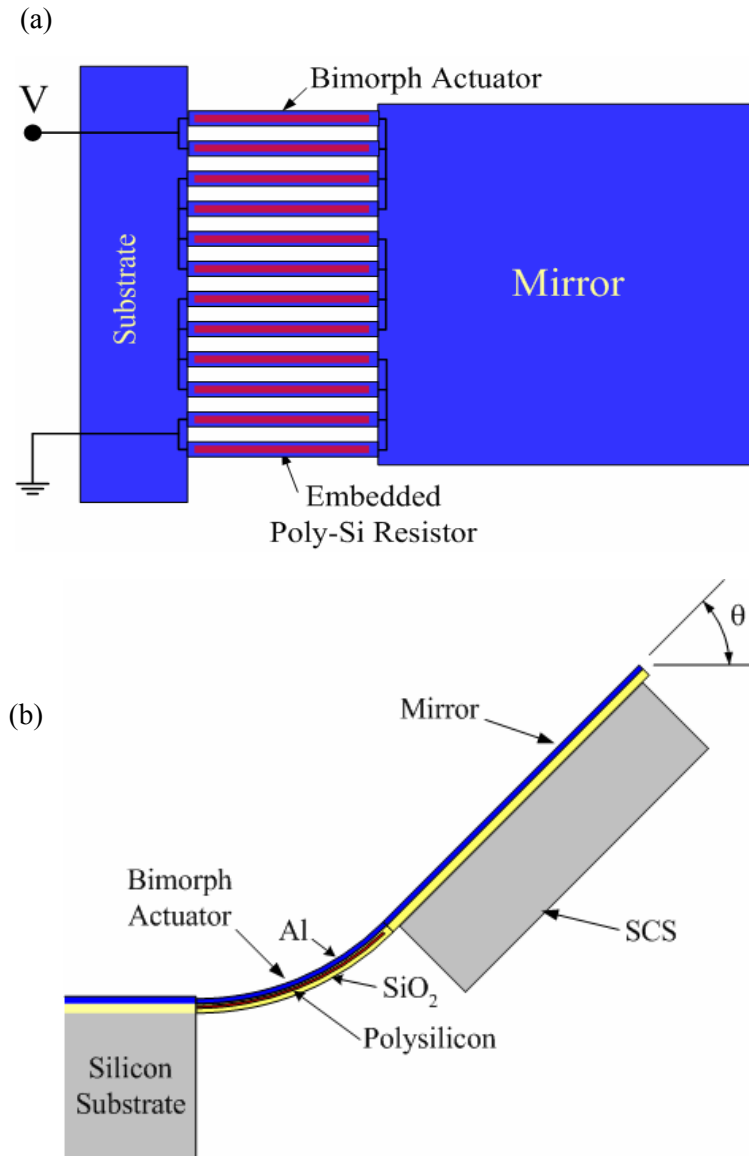


Figure 3-2: Electrothermal micromirror basic structure. (a) Top view. (b) Cross-sectional side view.

introduced in the previous section, the bimorph micromirrors presented here require thin-film bimorph structures for actuation and SCS structures for large size and flatness. The micromirrors were fabricated by a deep-reactive-ion-etch (DRIE) CMOS-MEMS process [122]. The basic idea of this process is to introduce an SCS layer underneath CMOS multi-layer structures in such a way that the mechanical properties are dominated by the SCS layer, electrical connections provided by the CMOS interconnect metal layers,

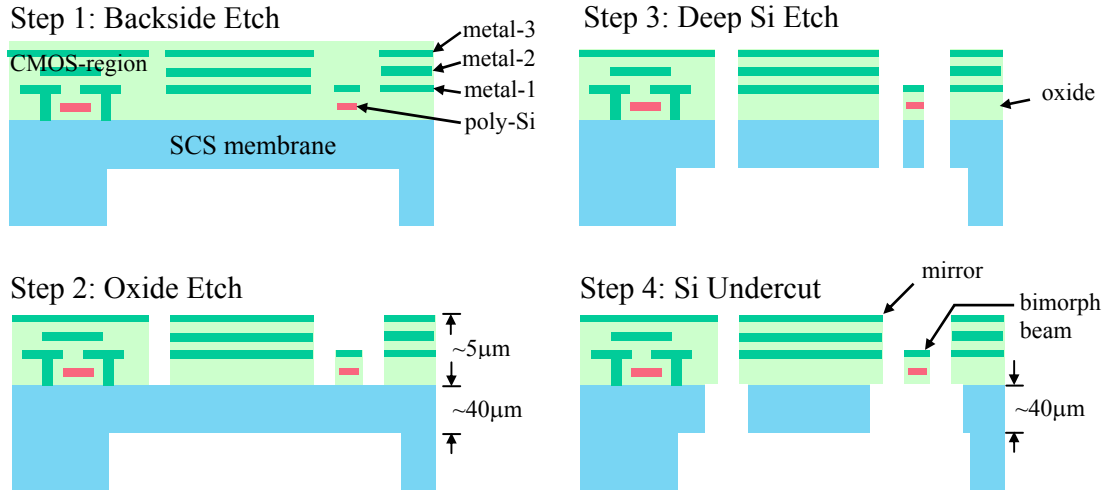


Figure 3-3: DRIE CMOS-MEMS fabrication process flow.

heating source provided by polysilicon and high reflectivity by the top metal layer. This maskless post-CMOS micromachining process has also been successfully used to fabricate integrated MEMS accelerometers and gyroscopes [123, 124].

The process flow is shown in Figure 3-3, which is completely CMOS-compatible and involves only four dry-etch steps. The process starts with CMOS wafers or chips that are fabricated at virtually any CMOS foundry. As a demonstration of foundry-CMOS compatibility, the devices presented in this dissertation were fabricated using the Agilent 0.5-µm or the AMI 0.5-µm 3-metal CMOS processes available through the MOSIS foundry service [125]. The first step of the post-CMOS fabrication process is to perform a backside DRIE step to form a 30 µm to 50 µm-thick SCS membrane. This etch step is carried out by the Bosch process [126 1996] on a Surface Technology Systems (STS) inductively-coupled-plasma (ICP) etcher. The etching chemistry used is SF_6/O_2 with the following parameters: 600 W coil power, 12 W platen power, 130 sccm SF_6 flow, 13 sccm O_2 flow, and 37 mT chamber pressure. This step controls the thickness of the microstructure and forms a cavity (~200 µm deep) that allows the microstructure to move

freely in a wide range. The depth of the cavity is determined by the thickness of the CMOS chips (which is typically around 250 μm). The second step is a frontside anisotropic oxide etch that uses the CMOS interconnect metal (i.e., aluminum) as an etching mask. This oxide RIE etch is performed in a Unaxis Shuttlelock ICP etcher with the following process conditions: 600 W coil power, 100 W platen power, 15 sccm SF_6 flow, 5 sccm Ar flow, and a chamber pressure of 5 mT. The oxide etch is followed by a deep silicon trench etch using the STS ICP etcher to release the microstructure. At the end of this step, a 30 μm to 50 μm thick SCS layer remains underneath the CMOS layer, resulting in a flat released microstructure. Finally, a brief isotropic silicon etch is performed to undercut the silicon from under the thin-film bimorph beams. Any beam with a half-width less than the silicon undercut will have no SCS layer underneath. This isotropic silicon etch is attained using the same STS ICP etcher but by reducing the platen power to 2 W. These undercut thin-film beams can be used to form electrically isolated SCS islands, purposely curled-up structures or z-compliant springs. In the micromirrors, these 2- μm -thick thin-film beams form bimorph actuators with an embedded polysilicon heater.

As the top aluminum layer is used as an etching mask, CMOS circuits under it will remain unaffected by the fabrication process. Thus, this maskless post-CMOS process is completely compatible with foundry CMOS processes, and CMOS circuits can be integrated with MEMS devices. When the mirror is released from the substrate during fabrication, the bimorph actuator is no longer constrained and will curl up. This bimorph curling occurs due to the residual tensile and compressive stresses present in the aluminum and silicon dioxide layers, respectively. As a result of the bimorph curvature,

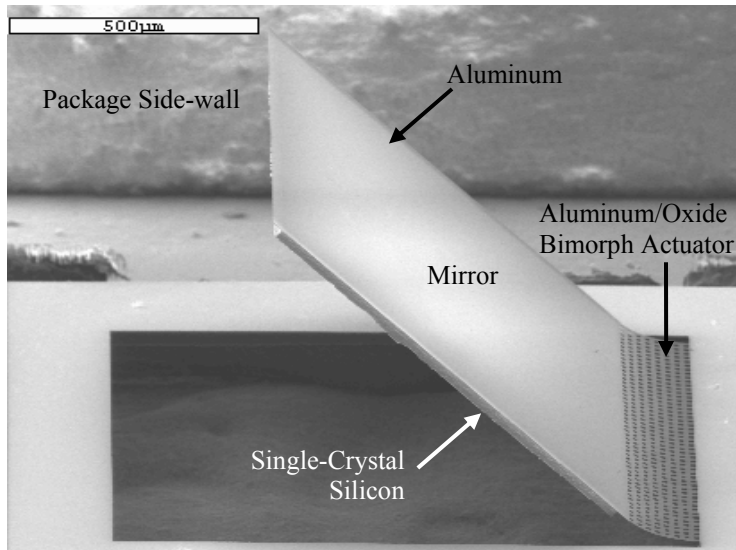


Figure 3-4: SEM of a fabricated 1-D micromirror with initial tilt angle.

the attached mirror tilts upward and away from the substrate with an angle equal to the tangential angle at the end of the bimorph. The SEM of a fabricated 1-D micromirror, demonstrating the initial tilting of the mirror plate, is presented in Figure 3-4.

3.4 Bimorph Actuation and Theoretical Analysis

Before looking into the actual electrothermal micromirrors, bimorph actuation theory and electrothermomechanical analysis are presented in this section.

The electrothermal micromirror is actuated by applying an electrical current to the polysilicon resistor. The electrical power dissipated by the resistor as heat raises the temperature of the bimorph actuator. Since the top Al layer has a greater coefficient of thermal expansion than the bottom SiO_2 layer, the increase in temperature causes the top metal layer to expand more than the bottom SiO_2 layer. This in turn increases the radius of curvature of the bimorph actuator by bending the bimorph in the downward direction. Therefore, the tilt angle of the mirror decreases from its initial value. Side-view schematics illustrating the released micromirror structure and the electrothermal actuation mechanism are shown in Figure 3-5.

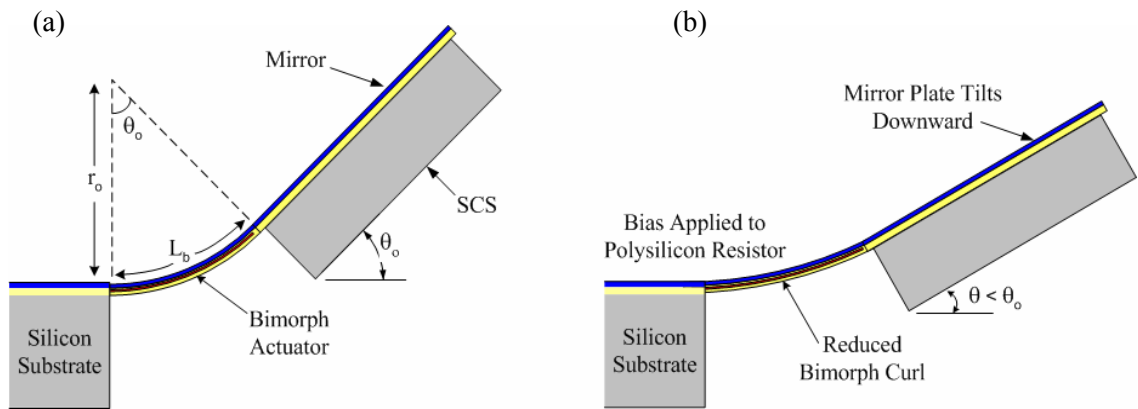


Figure 3-5: Bimorph actuation mechanism. Side views of: (a) Initial position of mirror at zero bias. (b) Downward rotation of mirror plate on application of bias voltage to polysilicon resistor.

The bimorph beam curls up after being released due to the tensile stress in the aluminum layer and compressive residual stress in the bottom silicon dioxide layer. Therefore, the radius of curvature of the bimorph beam is determined by both the initial curling and also due to the temperature change from the polysilicon heating, and is given by [105]:

$$\frac{1}{r} = \frac{1}{r_0} - \frac{1}{r_T} \quad (3-1)$$

where r is the actual radius of curvature, r_0 is the initial radius of curvature and r_T is the radius of curvature due to the temperature change. The minus sign is due to the fact that the initial curling of the bimorph is caused by residual stresses due to cooling from high processing temperature to room temperature, while the thermally induced curvature is caused by thermal heating.

By ignoring the thin polysilicon layer, r_T is readily derived as [127]:

$$\frac{1}{r_T} = \frac{6(t_{Al} + t_{ox})(\alpha_{Al} - \alpha_{ox})\Delta T}{4t_{Al}^2 + 4t_{ox}^2 + 6t_{Al}t_{ox} + \frac{E_{Al}t_{Al}^3}{E_{ox}t_{ox}} + \frac{E_{ox}t_{ox}^3}{E_{Al}t_{Al}}} \quad (3-2)$$

where ΔT is the temperature change of the bimorph beams, t_a , α_a and E_a are the thickness, thermal coefficient of expansion, and Young's modulus of the metal ($a=Al$) and oxide ($a=ox$) layers, respectively.

Equation (3-2) can be rewritten as

$$\frac{1}{r_T} = \beta_r \Delta \alpha_T \Delta T \quad (3-3)$$

where $\Delta \alpha_T = \alpha_{Al} - \alpha_{ox}$ is the difference in the coefficients of thermal expansion of Al and SiO₂, and β_r is the curvature coefficient of the bimorph beam as is given by:

$$\beta_r = \frac{6(t_{Al} + t_{ox})}{4t_{Al}^2 + 4t_{ox}^2 + 6t_{Al}t_{ox} + \frac{E_{Al}t_{Al}^3}{E_{ox}t_{ox}} + \frac{E_{ox}t_{ox}^3}{E_{Al}t_{Al}}} \quad (3-4)$$

As shown in Figure 3-5, the tangential angle at the tip of a curled beam is equal to the arc angle. Using simple geometry, we get

$$\theta_T = \frac{L_b}{r_T} \quad (3-5)$$

$$\text{or } \theta_T = \beta_r L_b \Delta \alpha_T \Delta T \quad (3-6)$$

where L_b is the length of the bimorph beam. Equation (3-6) relates the angular change of the bimorph actuator to its temperature increase.

Using Equations (3-1) and (3-3), we can express both the initial curvature and thermal-induced curvature in terms of the curvature coefficient as:

$$\frac{1}{r} = \beta_r (\Delta \varepsilon_0 - \Delta \alpha_T \Delta T) \quad (3-7)$$

where $\Delta\varepsilon_0$ is the linear strain difference caused by residual stress. Therefore, the actual tilt angle of the beam tip relative to the substrate plane is given by

$$\theta(\Delta T) = \theta_0 - \theta_T = \beta_r L_b (\Delta\varepsilon_0 - \Delta\alpha_T \Delta T) \quad (3-8)$$

where $\theta_0 = \beta_r L_b \Delta\varepsilon_0$ is the initial tilt angle. So, increasing the curvature coefficient will simultaneously increase the actuation angle and the initial tilt angle. Sometimes large initial tilt angle may be undesired, in which case a compromise has to be made.

Equation (3-6) gives the relationship between the actuation angle and the temperature change which is uniform along the entire bimorph beam. However, in most cases, the beam temperature distribution is not uniform, so the radius of curvature varies along the beam. Therefore, the tilt angle at the tip of the bimorph is an accumulation of the gradual curvature changes, *i.e.*,

$$\theta = \int_0^{L_b} \frac{dx}{r(x)} = \int_0^{L_b} \left(\frac{1}{r_0} - \frac{1}{r_T} \right) dx = \theta_0 - \int_0^{L_b} \beta_r \Delta\alpha_T \Delta T(x) dx \quad (3-9)$$

$$\text{or } \theta_T = \theta_0 - \theta = \beta_r L_b \Delta\alpha_T \left[\frac{1}{L_b} \int_0^{L_b} \Delta T(x) dx \right] = \beta_r L_b \Delta\alpha_T \Delta\bar{T} \quad (3-10)$$

where $\Delta\bar{T} = \frac{1}{L_b} \int_0^{L_b} \Delta T(x) dx$ is the average beam temperature difference above the

substrate (or ambient) temperature. Thus, the actuation angle is linearly proportional to the average temperature of the bimorph beam. This is valid as long as the increased temperature does not change the material and mechanical properties of the bimorph layers. This analysis assumes that the width of the bimorph layers is equal for both layers, the materials are isotropic and continuously distributed, and that the radius of curvature is constant along the bimorph beam.

3.5 Electrothermal Micromirrors

3.5.1 One-Dimensional Electrothermal Micromirror

An electrothermal micromirror consists of a thin-film bimorph structure and a bulk-silicon mirror plate. Instead of using a continuous bimorph mesh that was used in the previous designs [19, 28], the bimorph actuator was split into an array of bimorph beams, as shown in Figure 3.1. Since each beam has a relatively small width, the silicon undercut of the structure will remove all of the silicon underneath the beams, leaving a majority of the silicon underneath the mirror. This design was created to further improve the micromirror scanning performance by reducing the overall stress of the bimorph upon actuation. The buckling phenomenon observed by Xie *et al.* [19] is not present in this device. Another difference in the new design is that thermal isolation regions were added to isolate the bimorph beam array from the substrate and mirror plate regions. The thermal isolation regions are useful for two things. First, the thermal isolation region between the bimorph array and the substrate increases the average temperature of the bimorph array for a given bias, yielding a greater angular response of the mirror. Second, the thermal isolation layer between the bimorph and the mirror plate lowers the heat flux between the two regions upon actuation, resulting in a faster thermal response time of the bimorph. A lumped element model of this micromirror has been developed by Todd and Xie, and interested readers may refer to [128].

A single-axis micromirror with a bimorph actuator using this beam design has been fabricated [27]. A scanning electron micrograph (SEM) of a released device is shown in Figure 3-6. The micromirror is 1mm by 1mm in size, coated with aluminum, and thermally actuated by an integrated polysilicon heater.

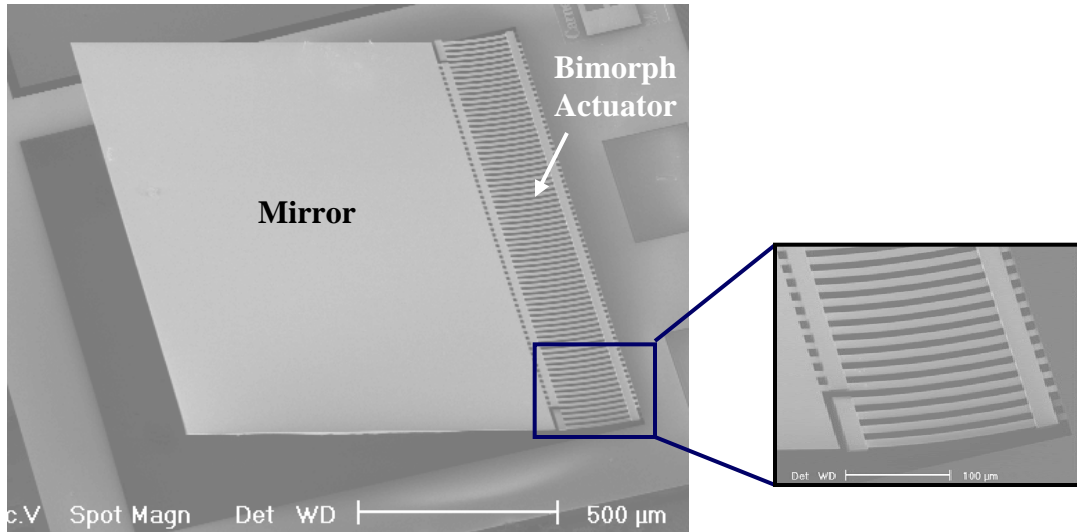


Figure 3-6: SEM of 1-D micromirror. Inset: Close-up of the bimorph actuator beams.

The bimorph beam array consists of 64 beams. The embedded poly-Si resistors of adjacent beams are connected in parallel giving a total of 32 resistors embedded in the bimorph beam array. The 32 resistors are connected in series yielding a total resistance of 1.15 k Ω for the bimorph beam array. Two voltage contacts are present on the furthest right and left resistors of the beam array. Figure 3-7 shows the measured rotation angles at different currents and also the current dependence of the polysilicon resistor. A rotation angle of 31 $^\circ$ is achieved at 9 mA or 18 V. The response curve is smooth over the whole scanning range. Thus, this mirror design also eliminates the discontinuity problem observed in the micromirror design reported by Xie *et al.* [19].

The resistance of the polysilicon resistor changes significantly with current. There are two effects attributed to the resistance change: piezoresistive effect and temperature dependence of polysilicon resistance. The temperature coefficient of the piezoresistivity is given by the product of the coefficient of thermal expansion and the gauge factor which are respectively $\sim 2.5 \times 10^{-6}/\text{K}$ and ~ 30 for polysilicon, while the temperature coefficient of resistivity of the polysilicon used in these micromirrors was measured to be

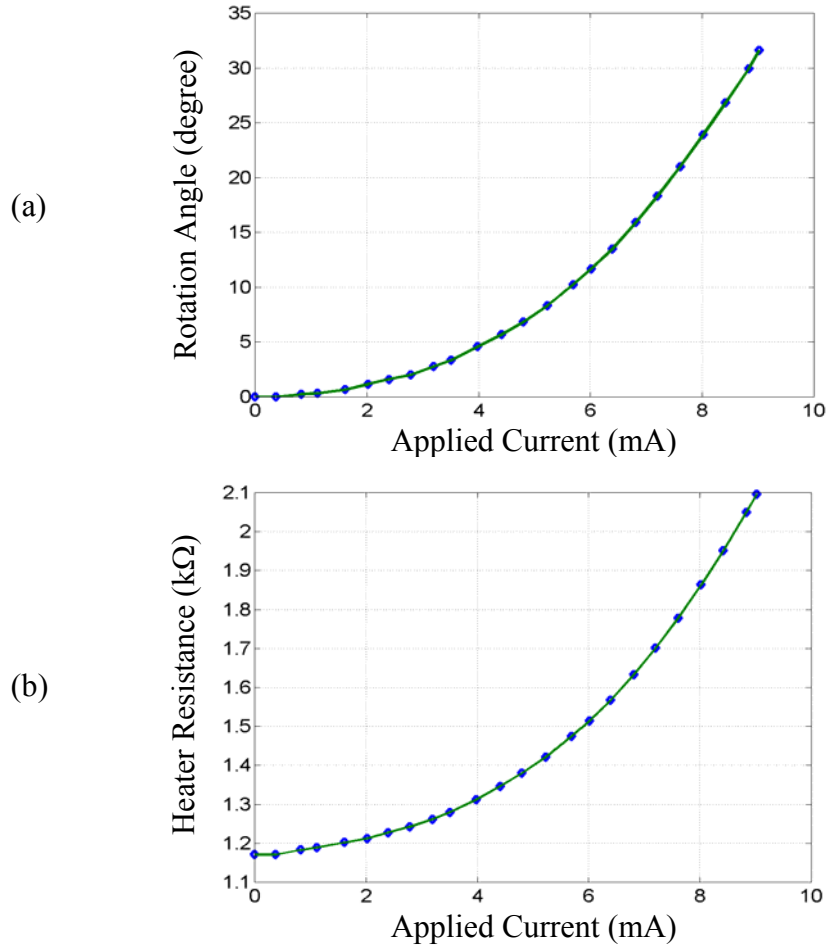


Figure 3-7: 1-D mirror characterization. (a) Rotational static response. (b) Plot of the heater resistance versus applied current.

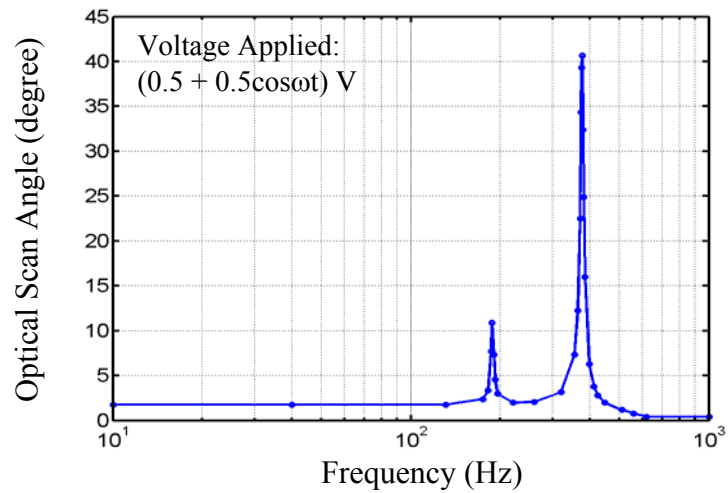


Figure 3-8: Frequency response of the 1-D mirror.

about $5.9 \times 10^{-3}/\text{K}$. Therefore, the piezoresistive effect can be ignored. The resonant frequency of the mirror is 380 Hz, as obtained in the frequency response of Figure 3-8. The radius of curvature of the mirror surface is about 50 cm.

3.5.2 Two-dimensional Electrothermal Micromirror

3.5.2.1 Device design

A two-dimensional (2-D) optical scanner was designed and fabricated by extending the 1-D mirror design concept presented in the previous section. This 2-D mirror uses a combination of two 1-D electrothermal actuators, to provide it two-dimensional scanning capability. The schematic drawing of this 2-D micromirror device is illustrated in Figure 3-9. The mirror is attached to a movable, rigid silicon frame by a set of bimorph aluminum/silicon dioxide thin-film beams. As before, a polysilicon resistor is embedded within the silicon dioxide layer to form the heater for the bimorph actuator. This movable silicon frame is connected to the silicon substrate by another set of identical bimorph thin-film beams that are oriented perpendicular to the first. In order to differentiate between the two actuators, the first set of actuators that rotate the mirror is defined as the *mirror actuator*, while the second set of beams that actuate the rigid silicon frame is defined as the *frame actuator*. The orthogonal orientation of these two actuators results in two perpendicular axes of rotation for the mirror plate.

As shown in the cross-sectional view of the device (Figure 3-9 (b)), the top layer of the mirror is aluminum. Thus, the mirror has high reflectivity. A 40 μm thick SCS layer backing the mirror plate keeps it optically flat. The mirror plate is 1 mm by 1 mm in size. This size is chosen for the micromirror to fit the available space in the OCT imaging probe. Each side of the rectangular frame is 75 μm wide, and it also has a 40 μm thick

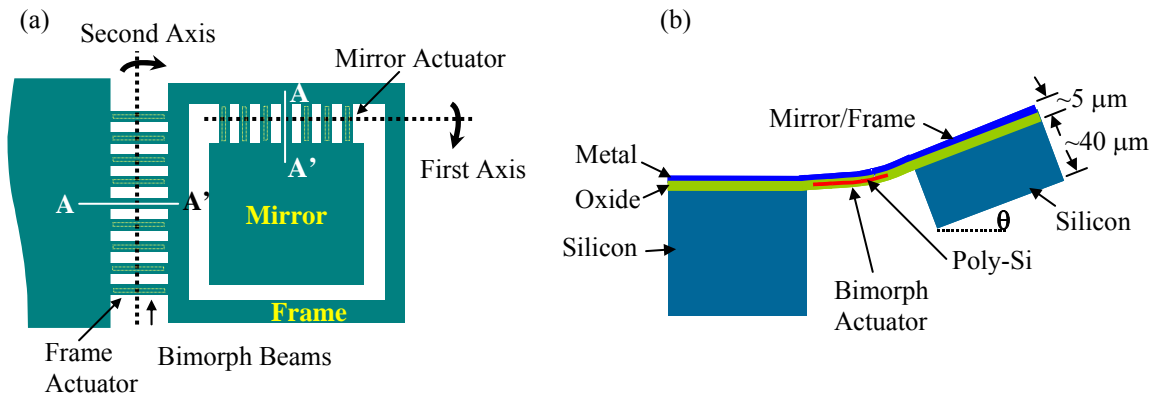


Figure 3-9: Schematic of the 2-D mirror design. (a) Top view showing the axes of rotation. (b) Cross-sectional view of A-A'.

SCS layer under it to provide rigidity to the structure.

The heating element in the bimorph beams is a set of 200 μm long, 7 μm wide, polysilicon strips oriented along the beams. This is the same actuator design used by the 1-D mirror design of Section 3.5.1. The polysilicon layer from the CMOS process permits a maximum current of 1 mA per micron width. Therefore, only a maximum current of 7 mA can flow through the 68 Ω polysilicon heater of each individual bimorph beam. In order to increase this current limit to a higher value, the polysilicon resistors in two adjacent beams are connected in parallel. This reduces the beam pair resistance to 34 Ω and increases the maximum current to 14 mA. The fabricated mirror has 32 and 38 pairs of bimorph beams in the mirror and frame actuators, respectively. This results in mirror and frame actuator resistances of 1.1 kΩ and 1.3 kΩ, respectively.

The SEM of a fabricated micromirror [29, 30] is shown in Figure 3-10. After fabrication, the initial tilt angles of the mirror and frame, with respect to the substrate, are 42° and 16°, respectively. These initial tilt angles are due to the residual stresses present in the bimorph beams. The maximum actuation angles, allowed by this device design, are

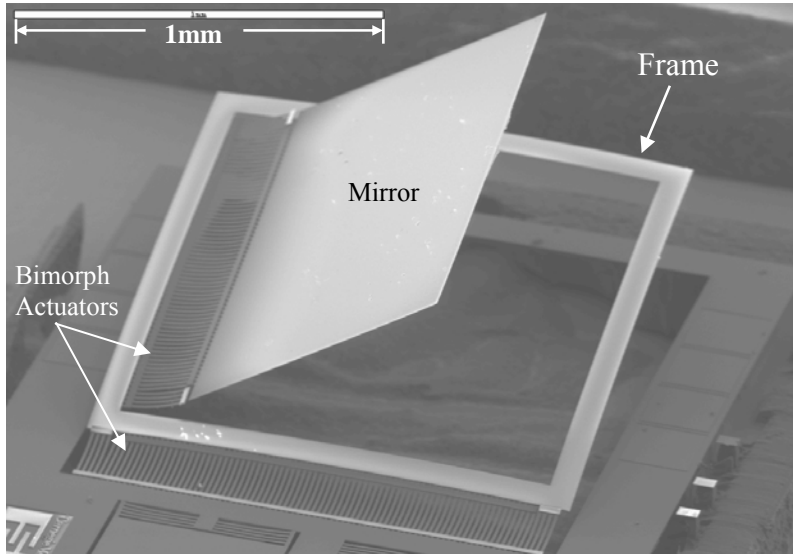


Figure 3-10: SEM of a fabricated 2-D micromirror.

limited by the substrate contact points and also by the maximum electrical current that can be passed through the beams. Calculations based on a 500 μm thick silicon wafer show that the mirror can tilt up to -22° , while the frame can tilt up to -17° below the chip surface. Therefore, the maximum allowed rotation angles for the mirror and frame are 64° and 33° , respectively.

3.5.2.2 Device characterization

Various experiments were performed to determine the characteristics of this device. These experiments include static response, frequency response, long-term stability, and thermal imaging of the device.

A simple experimental setup with a helium-neon (HeNe) laser and a dc current source was used to measure the static deflection angles. The mechanical rotation angle of the mirror was obtained by measuring the displacement of the reflected laser beam on a screen. Figure 3-11(a) shows the measured angles of rotation at different currents for the two independent axes. The mirror rotates 40° at an applied current of 6.3mA (or 15V, corresponding to an applied power of 95 mW), while the frame rotates by 25° at a current

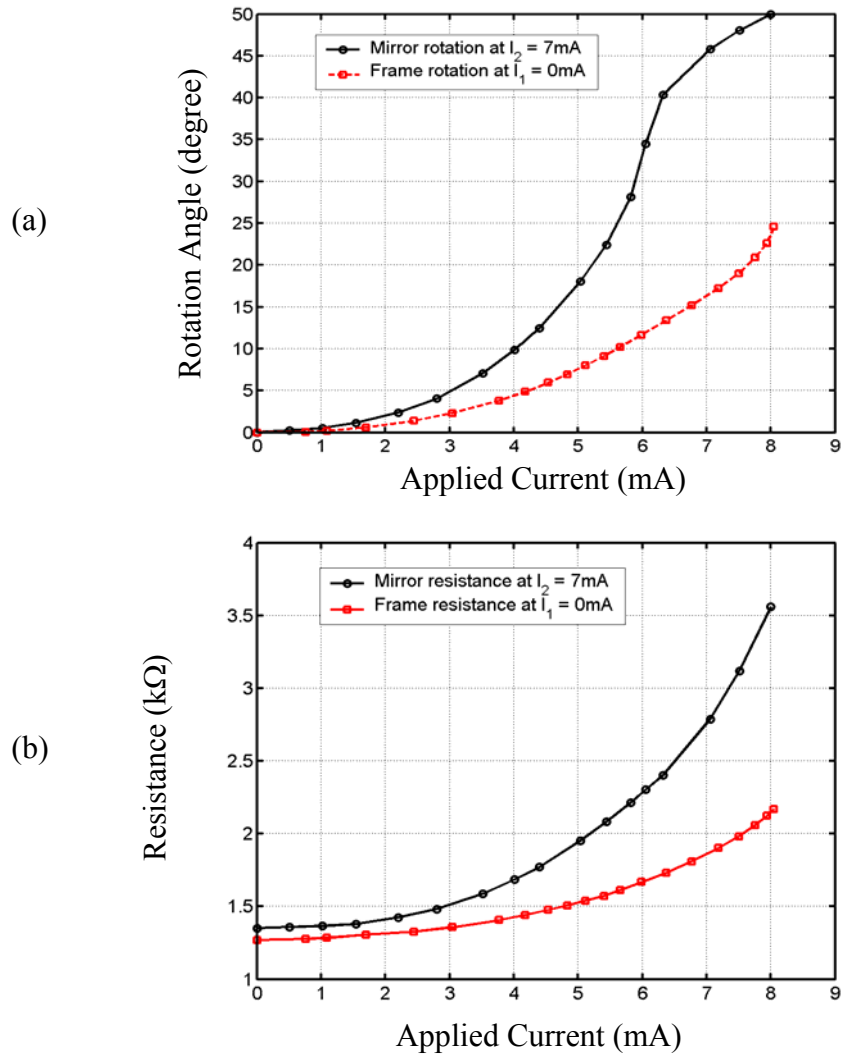


Figure 3-11: 2-D Mirror Characterization. (a) Rotation angle vs. current, and (b) Polysilicon resistance vs. current for the two actuators. I_1 : current in mirror actuator. I_2 : current in frame actuator. A 7 mA frame actuator current is required for aligning the rotation axis of the mirror actuator with the substrate.

of 8mA (or 17V, corresponding to a power of 135 mW). Mirror rotation angles up to 50° have been observed at higher currents, but the high stress induced in the bimorph actuator results in mirror instability. It has been observed that thermal damage in the polysilicon heater occurs at this point. The mirror instability limits the usable scan range of the mirror actuator to 40° . The dc current dependence of the resistors is plotted in Figure 3-11(b). The resistances of the polysilicon heaters change significantly with current because

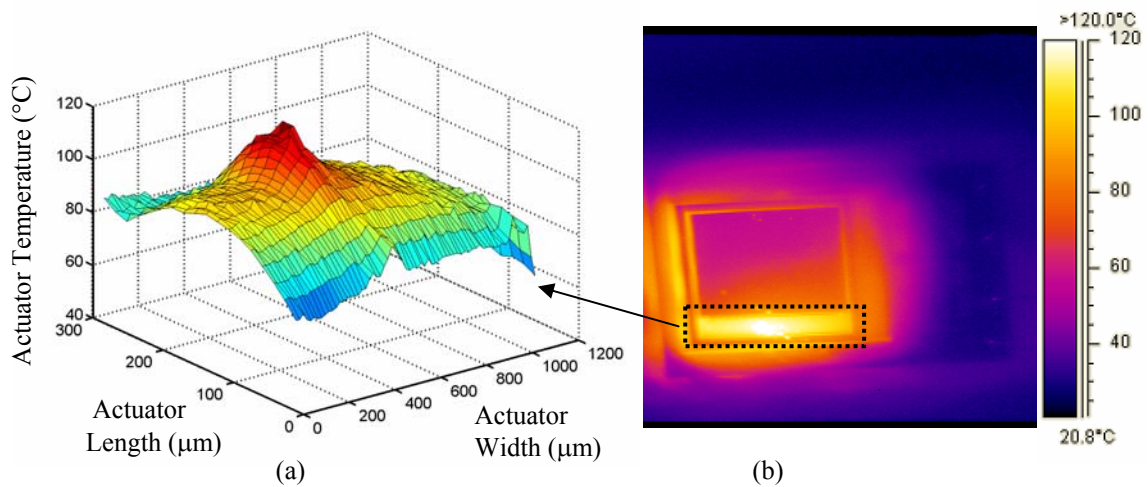


Figure 3-12: Thermal images of a device biased at 10 V. (a) Temperature distribution across the mirror actuator only [highlighted in (b)]. (b) Thermograph of the entire device.

the heating effect of the current causes temperature change, which in turn induces stress change in the bimorph beams. The measured open circuit polysilicon resistances of the mirror and frame actuators at room temperature are 1.09 k Ω and 1.26 k Ω , respectively.

The temperature distribution on the surface of the device was observed using an infrared thermal camera (FLIR ThermoCAM PM290). The temperature distribution profile of the entire mirror actuator is shown in Figure 3-12(a). Figure 3-12(b) shows this distribution over the entire device, and as expected, the mirror actuator has a higher temperature than the frame actuator due to the thermal isolation provided by the frame. Even though the actuator temperatures can be as high as 120°C, the mirror plate and silicon substrate dissipate heat and remain at relatively lower temperatures (~40°C). So there will be no thermal damage to tissue during endoscopic OCT imaging.

The resonant frequencies of the mirror and frame actuator structures were measured to be 445 Hz and 259 Hz, respectively. The radius of curvature of the mirror was measured by a Wyko NT1000 white light profilometer to be 0.33 m. The mirror can be made optically flatter by using a thicker SCS layer backing the mirror plate. The long-term stability of the mirror was evaluated by scanning the mirror to steer a laser beam onto a fixed screen. The mirror was continuously scanned at 5 Hz, and the scan length and angular position of the reflected laser beam were monitored for over 2 million cycles. For the entire duration of the experiment, the observed angular drift was about 0.8° ; which is mostly due to fluctuations in ambient temperature.

3.5.2.3 Laser scanning experiment

To further study the scanning behavior of the 2-D micromirror, a laser scanning experiment was performed, which simulates the 2-D transverse scanning for 3-D OCT imaging [129]. In this experiment, a simple visual display was successfully demonstrated by using this 2-D micromirror. The objective of this beam scanning experiment was to scan a pixel field with the micromirror and then to illuminate the selected pixels with a laser diode, thereby creating a projection display. The experimental setup is shown in Figure 3-13(a). By using a microprocessor to control the mirror and laser, 4×4 pixel-images were obtained at 10 frames per second. A sample image projected on a screen is shown in Figure 3-13(b). An active notch filter was incorporated into the amplifier to remove frequency content from the driving signals which could excite the mirror's resonant vibration modes. The 4×4 pixel resolution is largely limited by attempts to stabilize the mirror for each pixel. These techniques that were developed for a high-resolution projection display can be directly employed to control the laser beam scanning

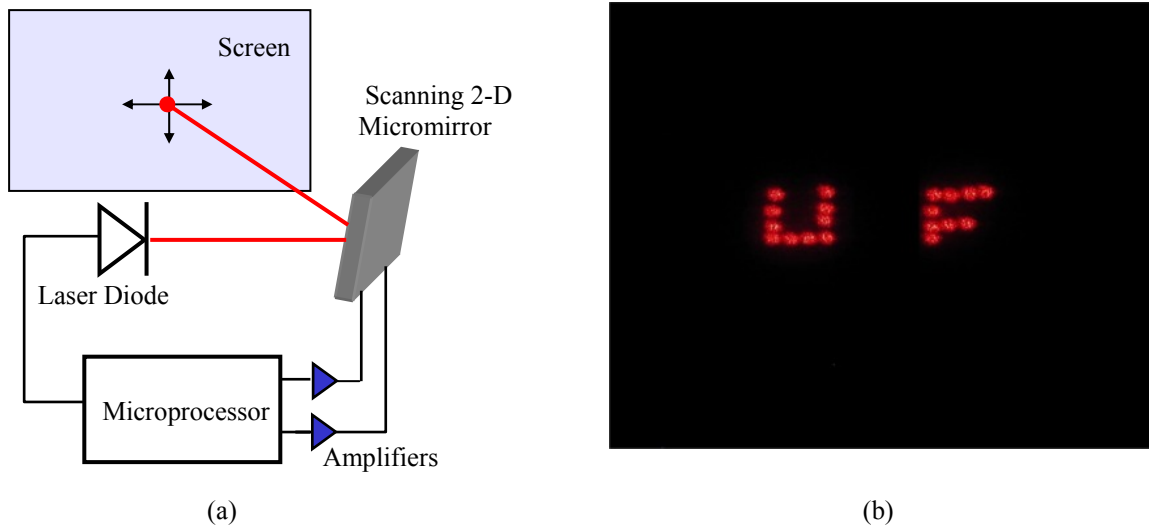


Figure 3-13: Laser scanning using the 2-D mirror. (a) Schematic of experimental setup. (b) 4 x 4 pixel images scanned by the micromirror.

in an endoscopic OCT system because the same basic operation of the device is required for both systems.

Due to the large angular displacements by the two actuators, the center of the mirror plate does not remain stationary in the vertical direction. For example, at a rotation angle of 20° (optical angle of 40°), the center of the mirror plate displaces downwards by $170\ \mu\text{m}$. This vertical displacement of the mirror plate does not affect the working of the laser scanning display, but needs to be accounted for during OCT imaging since it changes the optical path length of the scanning arm of the low-coherence interferometer.

3.6 Micromirror Packaging

For endoscopic OCT imaging, the micromirrors must be packaged inside endoscopes with diameters ranging from 3-5mm. It is proposed to use a similar package design as used by Xie *et al.* for their MEMS-based endoscopic-OCT system [51]. In this packaging scheme, the micromirror is glued onto a semicircular piece of printed circuit board (PCB) using a thermally-conductive epoxy. A picture of this custom-built PCB

package is shown in Figure 3-14. This PCB package has flexible electrical wires soldered to the surface gold-coated contacts. A wire bonder is used to wire-bond gold wire from the bond pads on the micromirror chip to the gold contact area on the PCB. A customized holder has been manufactured to hold the PCB package during this wire-bonding step. The packaged micromirror and PCB are then placed on a machined ferrule. This ferrule provides through holes for passage of the electrical wires from the PCB. The ferrule with the packaged micromirror is then fitted inside a hollow endoscope tube.

There are two primary ferrule placement configurations. For forward-imaging probes, a stationary reflective mirror is required that directs the collimated light beam from the fiber on to the micromirror plate. The reflected light from the micromirror is focused in tissue through an optical window located on the distal end of the probe. The second configuration provides side-imaging OCT probes, in which the light beam exits the cylindrical probe through its side. For this arrangement, the ferrule is fitted into the

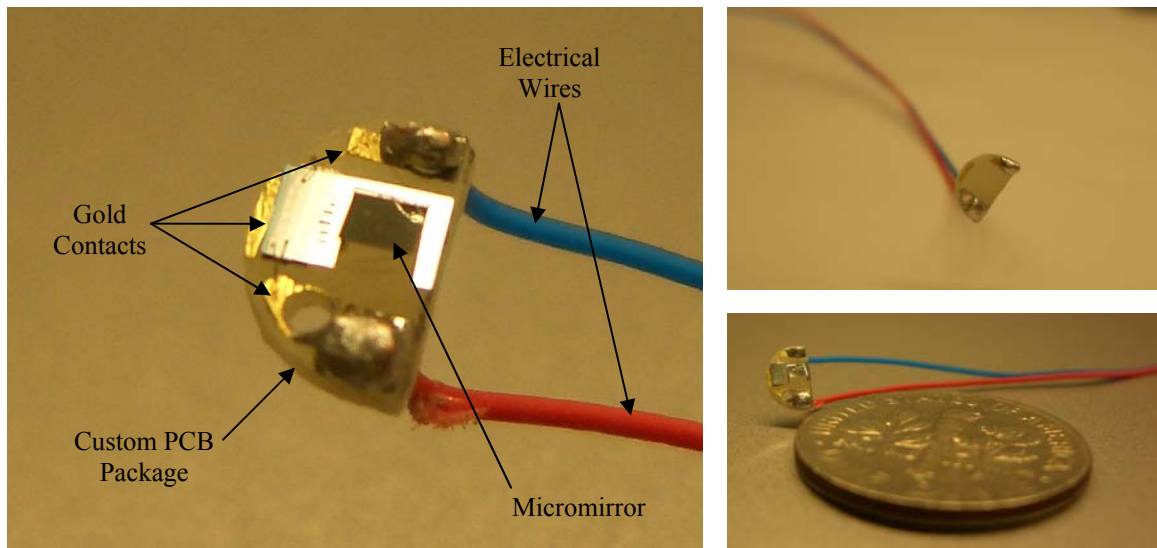


Figure 3-14: Micromirror package. (a) Packaged micromirror on a custom PCB. (b) Picture of the PCB package. (c) Picture of a packaged mirror alongside a US dime coin.

endoscope tube such that the micromirror is placed at an angle of 45° with respect to the optical fiber. The reflected light from the micromirror is scanned on to the tissue through an optical window located on the side of the endoscope. A schematic of these configurations is illustrated in Figure 3-15.

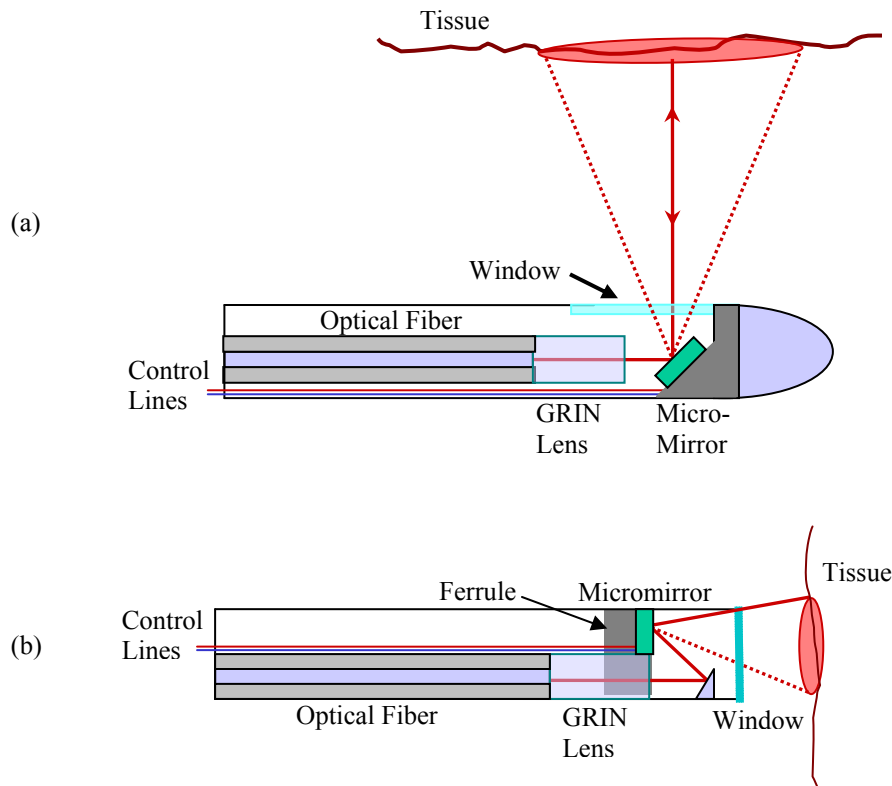


Figure 3-15: Endoscopic OCT probe designs. (a) Side-imaging configuration. (b) Forward-imaging configuration.

3.7 MEMS-based Endoscopic OCT Imaging

3.7.1 MEMS-based OCT System Design

The electrothermal micromirror packaged on the PCB, shown in Figure 3-14, has been installed into a custom-made 5-mm diameter endoscope tube for *in vivo* OCT imaging. The OCT system work was performed in collaboration with Dr. Yingtian Pan

and Zhenguo Wang of the State University of New York at Stony Brook who performed the endoscope system construction and testing.

The schematic of this endoscopic OCT system is shown in Figure 3-16. A high-power, broadband light source (AFC Technology) with an output power of 13 mW, a central wavelength (λ_0) of 1310 nm, and a full width - half maximum (FWHM) spectral bandwidth ($\Delta\lambda$) of 80 nm has been used. The coherence length that determines the axial resolution of the OCT system is 9.7 μm . The pigtailed output from the broadband light

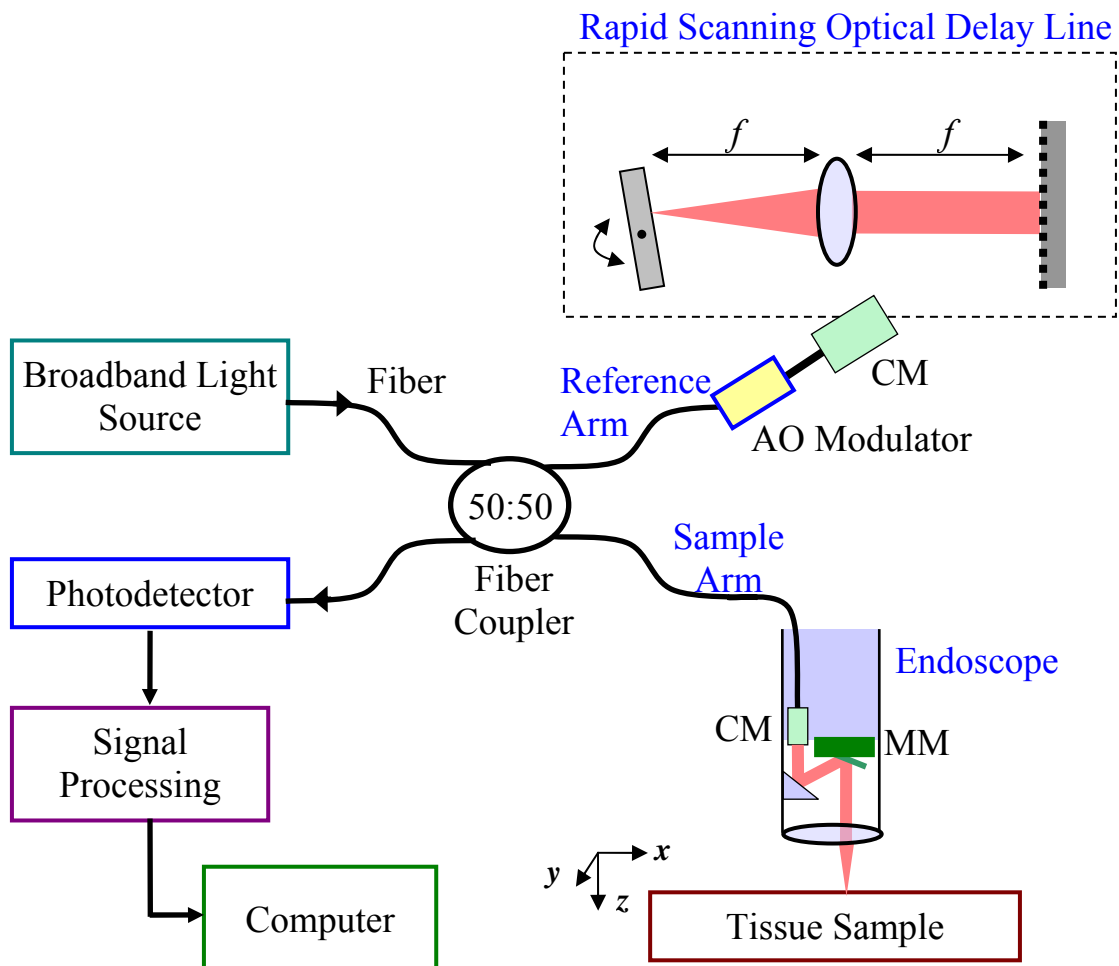


Figure 3-16: Schematic of the MEMS-based endoscopic OCT system. CM: collimating GRIN lens, MM: micromirror, AO: acousto-optic

source is coupled into a fiber optic Michelson interferometer, where the input light beam is equally divided into the two arms of the interferometer using a fiber coupler.

A fiber-optic polarization controller (FPC) in the reference arm of the fiber-optic interferometer ensures that the polarization of the exiting light beam from the non-polarization maintaining, single-mode fiber (SMF-28) is almost linearly polarized. The exiting light from this fiber is collimated into a 2-mm diameter optical beam by an angle-polished GRIN lens used as a collimator (CM). A rapid-scanning optical delay (RSOD) line utilizing a grating, lens and scanning mirror is used for axial scanning.

In the RSOD, the temporal profile of a broadband light is linearly distributed at the Fourier focal plane of a grating-lens pair, and by placing a mirror at the focal plane and tilting it rapidly results in fast group delay. To provide a stable and appropriately elevated Doppler frequency shift, a fiber-optic acousto-optic (AO) modulator is inserted into the reference arm before the RSOD. In this A-O modulator, two crystals are configured with one upshifted to 56 MHz and the other downshifted to 55 MHz to frequency modulate the light to 2 MHz for heterodyne detection. By carefully choosing the parameters of each component (e.g., $f = 80 \text{ mm}/\phi 35 \text{ mm}$ for the scan lens, $g = 450 \text{ lines/mm}$ for the diffraction grating, 4 mm VM500 galvanometric mirror tilted at 4.2° and with 4 kHz repetition rate, and 2 MHz A-O frequency modulation), the high-speed depth scanner allows the acquisition of 4 K axial scans per second with an optical delay window of 2.8 mm (higher path length delay is possible by increasing the tilting angle). The high and stable Doppler frequency shift results in increased signal to noise performance of the signal processing electronics. Moreover, the dispersion induced by unbalanced fiber lengths and optical components between two arms of the Michelson interferometer can be

minimized by slightly moving the grating along the optical axis, which can greatly enhance the axial resolution as has been observed during the alignment.

The sample arm of the Michelson interferometer is connected to the fiber-optic MEMS-based OCT endoscope through FC/APC fiber connector. The design schematic of the forward-imaging MEMS-based OCT endoscope is shown in Figure 3-15(b). The light from the fiber is collimated by a 0.25-pitch selfoc GRIN lens to a 1.1-mm diameter optical beam, which is then reflected by a fixed mirror onto the surface of the tilted micromirror. The MEMS micromirror is used for transversely scanning this light beam onto a fixed laser doublet exit lens. The 5-mm diameter laser doublet has a focal length of 10 mm, and it focuses the light beam into a 12- μm diameter spot at its image plane.

Figure 3-17 shows photographs of the packaged OCT endoscopes.

Since the MEMS mirror has an initial tilt angle of $\sim 20^\circ$, the custom-machined ferrule on which the micromirror sits is tilted by about 10° to keep the reflected beam on the center of the optical axis of the end lens. The backscattered light from tissue is collected by the same sample-arm optical path, and the combined interferometric signal from the sample and reference arms of the interferometer is detected by a photodetector. The detected signal is pre-amplified using a low-noise, transimpedance amplifier (Femto HCA-10M-100K), bandpass filtered and demodulated prior to being digitized by a 5 MHz, 12 bit A/D converter. Both depth scan and lateral MEMS scan are synchronized with the image data acquisition via two 16-bit D/A channels. All these components have been assembled into a readily transportable trolley console of Figure 3-18 to permit portable OCT imaging.

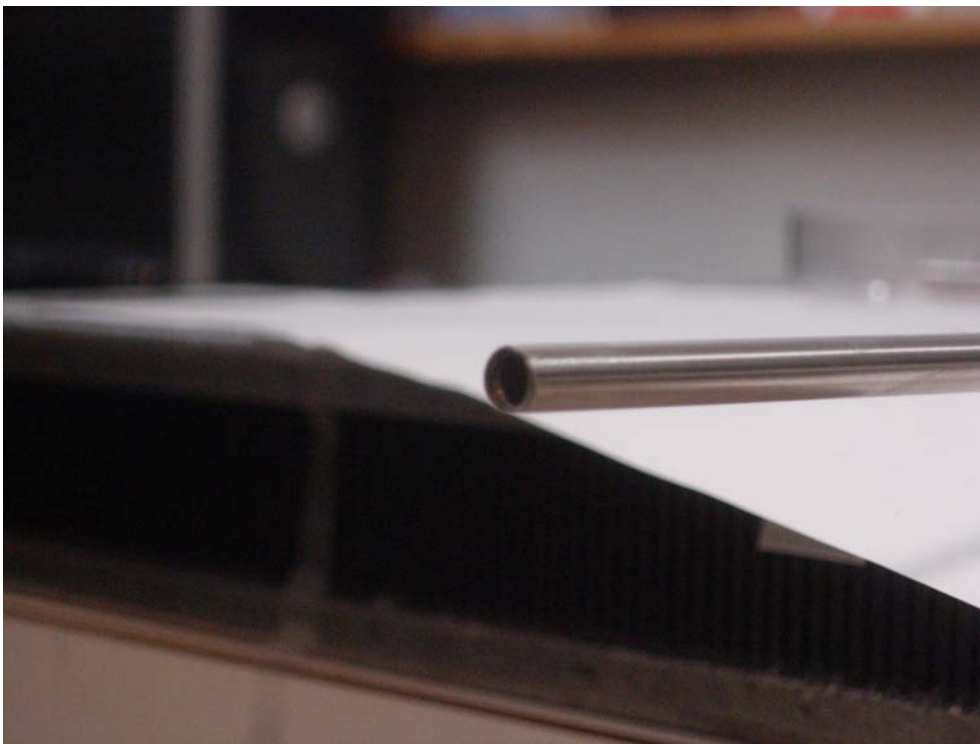
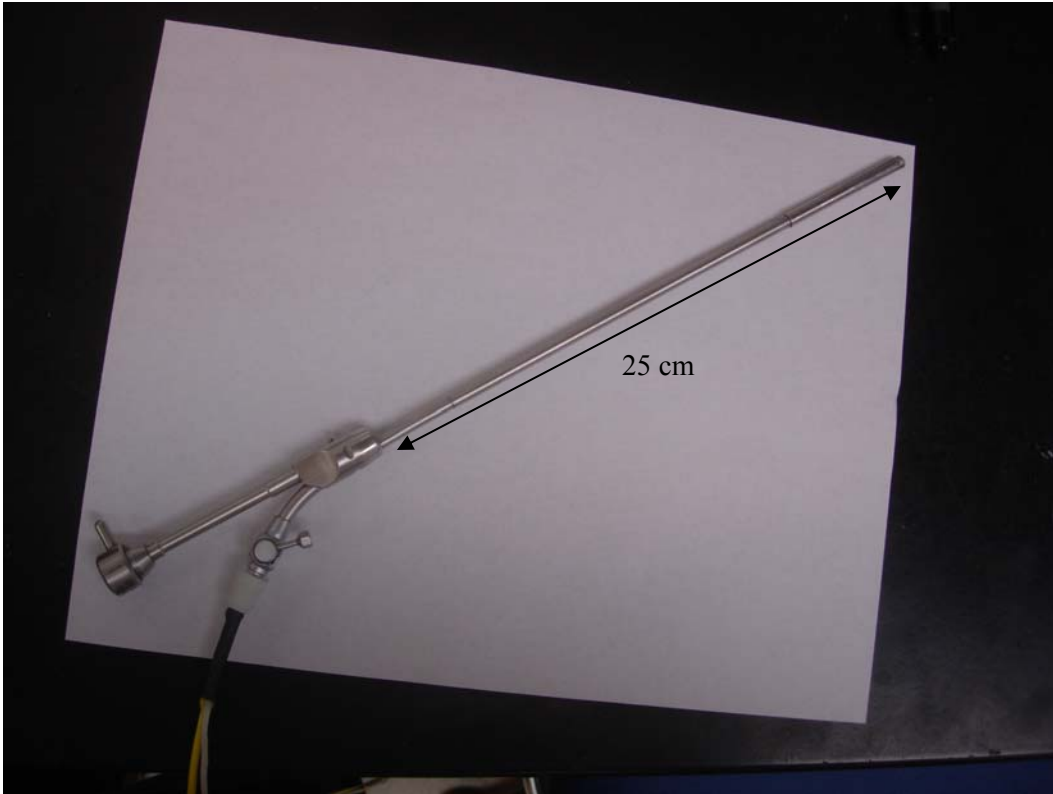


Figure 3-17: Photographs of the 5-mm diameter MEMS-based OCT endoscope at the State University of New York at Stony Brook. Photographs by Z. Wang. Used with permission.

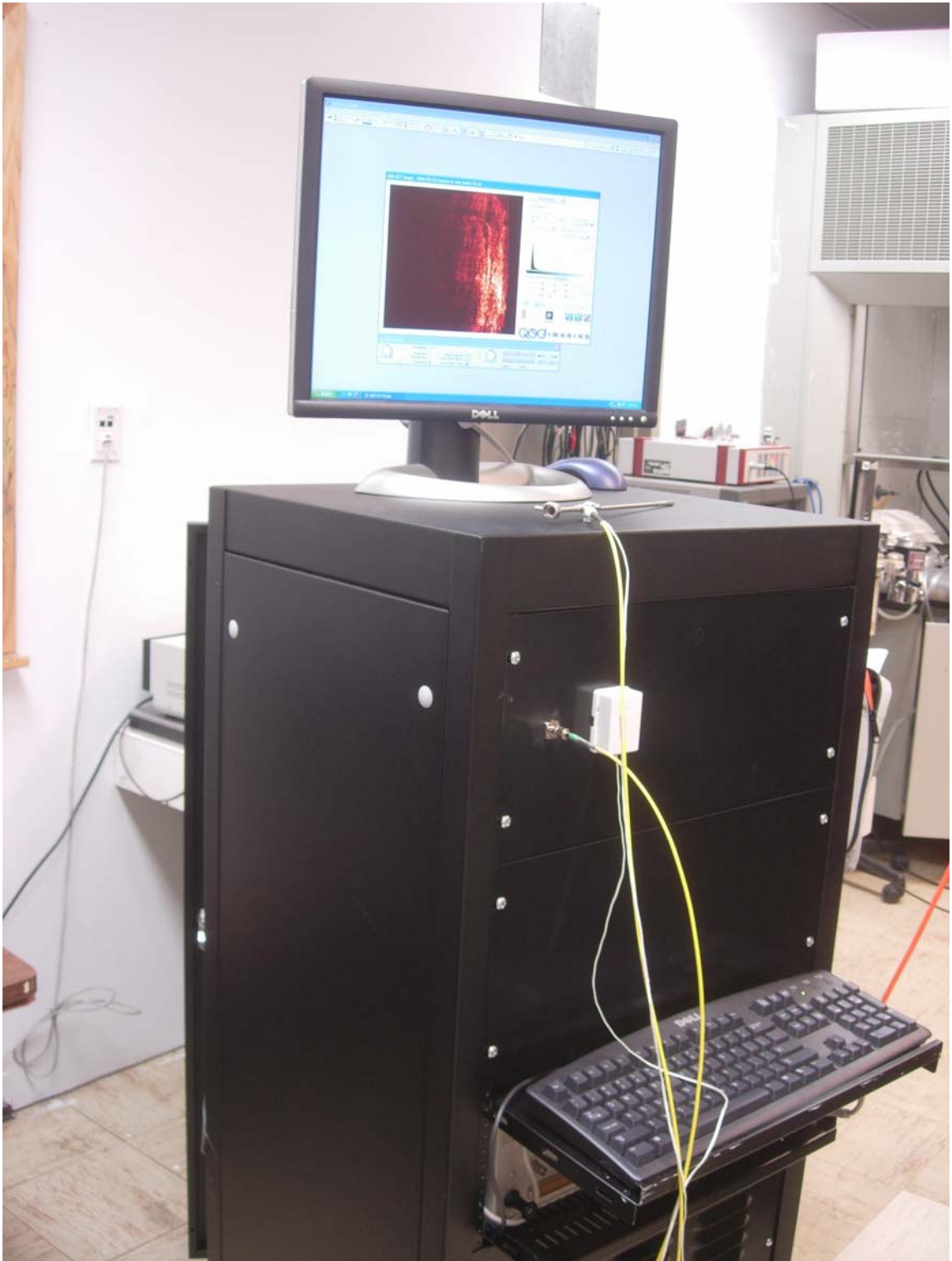


Figure 3-18: Photograph of the portable, MEMS-based endoscopic OCT system at the State University of New York at Stony Brook. Photograph by Z. Wang. Used with permission.

3.7.2 OCT Imaging Results

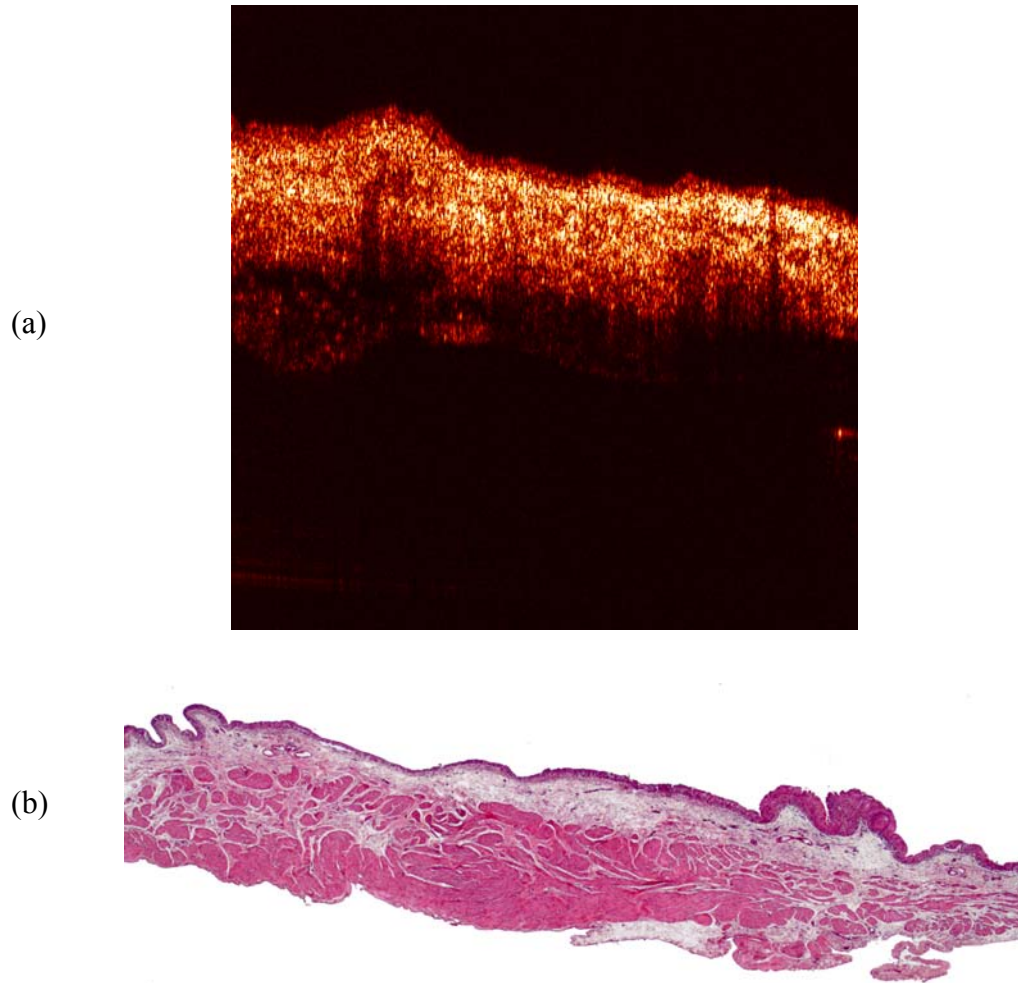


Figure 3-19: Comparison of OCT with histological image. (a) OCT image, and (b) histological image of rat bladder. Imaged by Z. Wang. Used with permission.

To demonstrate the ability of these MEMS mirrors for endoscopic OCT imaging the packaged endoscope shown in Figure 3-17, was connected to the portable OCT system shown in Figure 3-18. Figure 3-19 is a comparison between an OCT image and a histology photograph of a rat bladder. The OCT image was acquired at an imaging speed of 4 frames per second, and covers an area of $2.9 \times 2.7 \text{ mm}^2$ [52, 130]. The lateral and axial resolutions are $15 \text{ }\mu\text{m}$ and $12 \text{ }\mu\text{m}$, respectively. Figure 3-20 compares the OCT image quality for rat bladder tissue imaged using bench-top and endoscopic MEMS-based OCT systems.

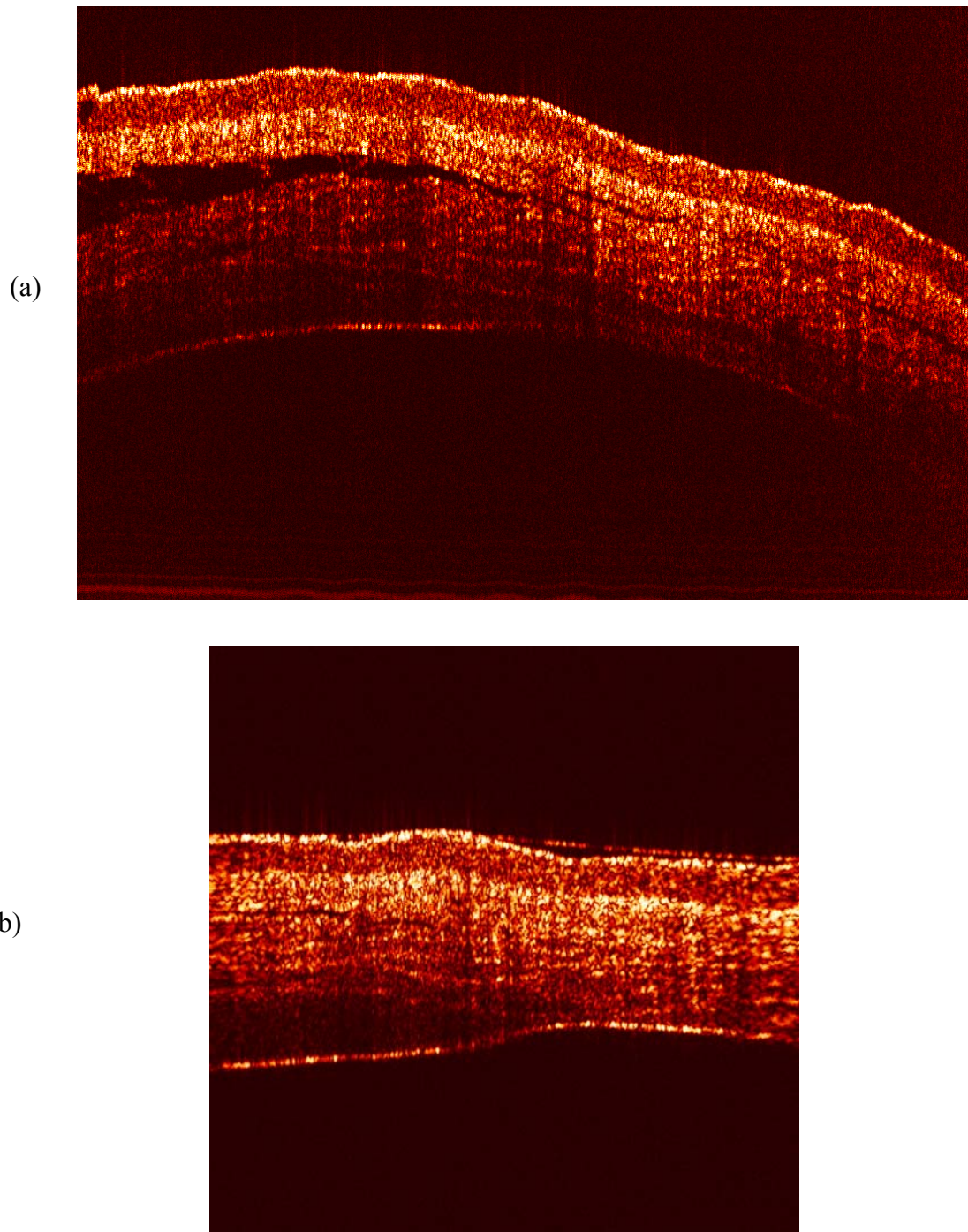


Figure 3-20: Bench-top versus MEMS-based endoscopic OCT imaging of rat bladder. (a) Bench-top OCT image. Size: 6 mm by 2.7 mm. (b) Endoscopic MEMS-based OCT image. Size: 4 mm by 2.7 mm. Imaged by Z. Wang. Used with permission.

As can be seen in these images, the morphological details of the rat bladder wall, e.g., the epithelium, submucosa and the upper muscularis layer are readily delineated. Because most transitional cell carcinomas originate in the epithelium, these results demonstrate the potential of MEMS-based endoscopic OCT for early detection and staging of bladder cancers. Also, as a wide variety of inner organs (e.g., cervix, colon, joints) can be accessed and imaged by front-view endoscopic OCT, the results suggest the potential applications of this technique for noninvasive or minimally invasive imaging diagnosis in these tissues.

3.8 Summary

This chapter reviewed the different types of micromirrors that have been reported in literature. The selection of electrothermal actuation as the technique for micromirror actuation for this research project was justified. Theoretical analysis about electrothermal bimorph actuation, along with the fabrication process used to fabricate these micromirrors was also presented. This chapter also presented 1-D and 2-D electrothermal micromirror designs, along with experimental results. The low driving voltage and large rotation angles of these devices make them very suitable for use in endoscopic OCT imaging systems. A forward-imaging OCT endoscope using an electrothermal MEMS mirror for endoscopic light steering to achieve biomedical imaging at transverse and axial resolutions of roughly 15 μm and 12 μm , respectively, has been demonstrated. Cross-sectional OCT images covering an area of $4.0 \times 2.7 \text{ mm}^2$ can be acquired at 2-16 frames/s and with close to 100 dB dynamic range. The 5-mm diameter large OCT endoscope was chosen to fully use the internal clearance of a 22 Fr endoscope. Smaller OCT scopes can also be developed to accommodate various types of endoscopes.

However, some optical design and packaging issues for these micromirrors include their unidirectional operation mode and non-stationary center of rotation of the mirror plate. These issues can be resolved by using the novel microactuator design presented in the next chapter.

CHAPTER 4 LARGE-VERTICAL-DISPLACEMENT MICROMIRRORS AND NON-LINEAR OPTICAL IMAGING

The 1-D and 2-D scanning micromirrors presented in Chapter 3 provide large rotation angles for transverse scanning in OCT imaging, but the unidirectional operation, non-stationary center of rotation, and large initial tilt angle of those micromirrors complicated the device packaging and optical design. These issues can be resolved by a novel mirror design that uses two complementarily-oriented electrothermal actuators, to keep the mirror surface parallel to the substrate and also to provide it bi-directional scanning capability. This chapter presents a new large-vertical-displacement (LVD) micromirror design that can perform rotational scans, as well as generate large piston motion at low driving voltages. Out-of-plane displacement of the micromirror is provided by a pair of electrothermal actuators. It is well known that there is large z -displacement at the tip of a long rotational beam. The innovation of this LVD device is converting the large tip displacement into a pure z -axis displacement of a flat micromirror. The LVD microactuator design can potentially achieve maximum vertical displacements of a few millimeters with millimeter-sized devices. Since this device can also perform bi-directional scans, it can also be used in the sample arm of an endoscopic OCT system to transversely scan the tissue surface.

Further miniaturization of the OCT system is also possible by using the large piston-motion of LVD micromirrors to perform the millimeter-range axial scans that are currently scanned in the reference arm of Figure 2-7. Piston-motion micromirrors are also

required by various other applications such as wave-front shaping in adaptive optics [131], interferometry systems [132], and spatial light modulators [133]. Numerous piston-motion actuation designs have been reported in literature. An electrostatic deformable micromirror reported by Helmbrecht *et al.* displaced up to 6 μm [131]. Lee *et al.* and Kwon *et al.* presented devices that used electrostatic vertical comb drives (VCDs) to demonstrate maximum static vertical displacements of 7.5 μm [134], and 20 μm [60], respectively. Milanović *et al.* reported an electrostatic VCD micromirror that generated piston motion of 60 μm , but at a high actuation voltage of 130 V [101]. Cugat *et al.* reported a deformable micromirror with electromagnetic actuation that displaced up to 20 μm for use in adaptive optics [135]. Yee *et al.* developed a piezoelectric micromirror for high-precision tracking of a laser beam for high-density optical data storage [136]. Tuantranont *et al.* demonstrated a 2 μm displacement using an electrothermally-actuated trampoline-type micromirror for light phase modulation [137]. Wan *et al.* explored a new type of micromirror which utilized electrocapillary actuation to push a mirror vertically up to 8 μm using a mercury droplet in a metal-plated microhole [138]. However, these actuators can only generate up to a few tens of microns of vertical displacement, and therefore cannot be used to meet the millimeter-range axial scanning requirement of OCT systems.

In this chapter, two novel large-vertical-displacement (LVD) micromirror designs are presented that can generate bi-directional scans, and also perform large out-of-plane vertical displacement. The first mirror design uses one set of LVD microactuators to perform 1-D bi-directional scans. The second mirror design uses two sets of LVD microactuators to enable 2-D bi-directional rotational scanning.

4.1 LVD Microactuator Design

The LVD microactuator consists of two complementary electrothermal actuators in a folded structure which allows a mirror plate to remain parallel to the substrate surface, while still taking advantage of the large stroke lengths provided by the actuators. The schematic drawing of the LVD micromirror is illustrated in Figure 4-1 which is very similar to the 2-D electrothermal micromirror design which was presented in Section 3.5.2. The only difference being that the inner and outer bimorph actuators are aligned along the same axis in the LVD micromirror, instead of orthogonal to each other as in case of the 2-D micromirror. The inner and outer bimorph actuators are still referred to as *mirror actuator* and *frame actuator*, respectively.

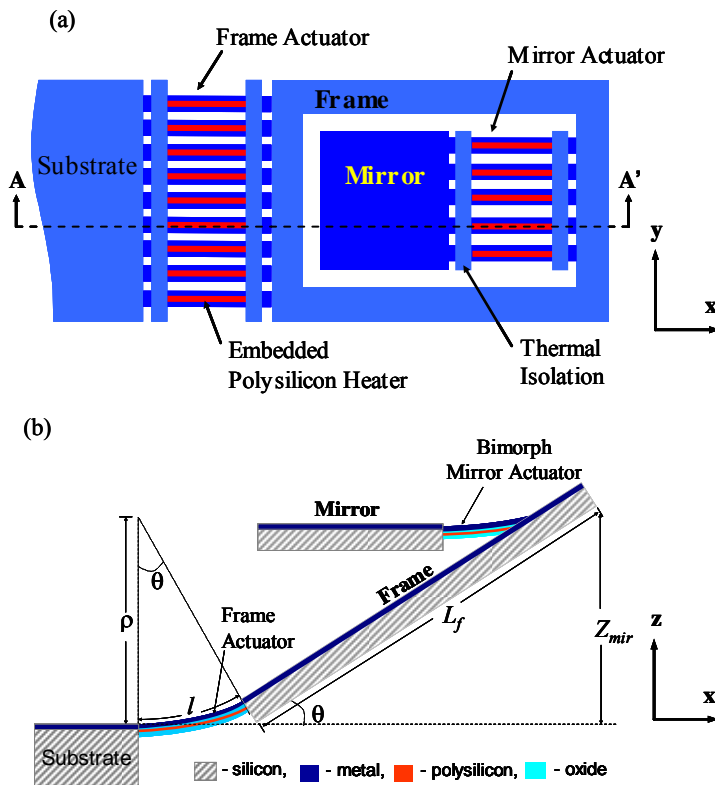


Figure 4-1: Design schematic of the LVD mirror. (a) Top view. (b) Cross-sectional view across A-A'.

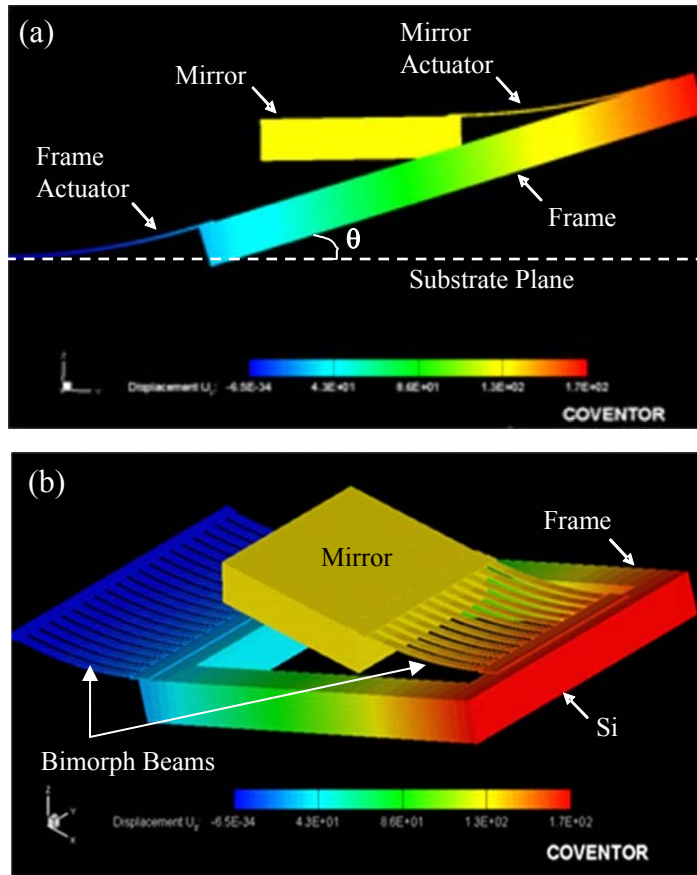


Figure 4-2: Coventor simulations. (a) Device side-view. (b) 3-D model of the LVD micromirror illustrating the initial curling of the bimorph actuators. The mirror surface is parallel to the substrate plane since the curling of the two actuators compensate each other.

FEM thermomechanical simulation was conducted using CoventorWare [139]. The simulation results are shown in Figure 4-2, where the curlings of the two sets of bimorph beams compensate each other resulting in a zero initial tilt. The initial elevation of the mirror plate above the substrate plane, z_{mirror} , due to the curling of the thermal actuators can be calculated from:

$$z_{mirror} = (L_f - W_f) \cdot \sin \theta \quad (4-1)$$

where L_f and W_f are the length and beam width of the frame, respectively. θ , the initial tilt angle of the frame, can be computed from $\theta = l/r$; where l and r are the length and

radius-of-curvature of the thermal actuator, respectively. For a frame with $L_f = 0.5$ mm, $W_f = 40$ μm , and $\theta = 17^\circ$, the initial rest position of the mirror Z_{mirror} is 135 μm . The simulation results in Figure 4-2 show that the mirror plate is located 0.132 mm above and parallel to the substrate plane. There is no substrate underneath the mirror plate.

The mirror and frame actuators rotate the mirror in opposite angular directions. Therefore, there exist two basic modes of operation: (1) Bi-directional scanning by alternatively applying voltages to the mirror and frame actuators; and (2) Large piston motion by simultaneously applying voltages to both actuators. Equal angular rotations by the two actuators will result in pure vertical displacement of the mirror. Large z -axis displacement is achieved via the angular amplification due to the long arm length of the frame.

In order to enable independent electrical excitation for each actuator, a wiring schematic as shown in Figure 4-3 is used. The metal-1 aluminum layer on top of the bimorph beams is electrically divided into several paths to carry the actuation current for the inner actuator. For example, the metal-1 layer on the frame actuator has been divided

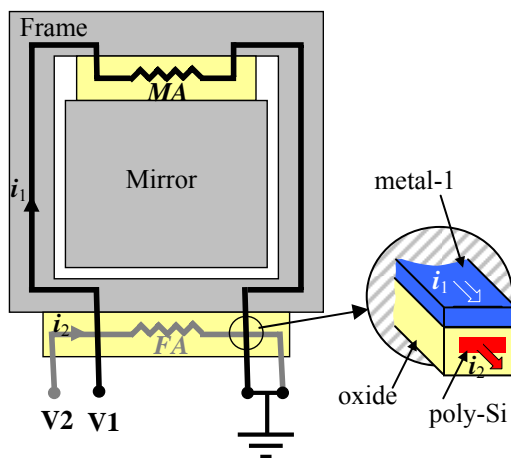


Figure 4-3: Wiring schematic for the LVD actuators. Inset: Section of a frame actuator bimorph beam showing that the mirror actuator current (i_1) is carried by metal-1 layer.

into two electrical paths that carry current in and out for the mirror actuator. As seen in the inset of Figure 4-3, the actuation current which flows through the polysilicon heater is electrically isolated from the current flowing through the metal-1 layer by a thin oxide layer.

4.2 1-D LVD Micromirror

4.2.1 Fabricated Device

A fabricated 0.7 mm by 0.32 mm LVD micromirror device [140-142] is shown in Figure 4-4. The fabrication process is exactly the same as the one described in Section 3.3. This LVD device has its mirror plate elevated about 100 μm above the silicon substrate plane. The initial tilt angle of the frame with respect to the substrate surface is 13°. The heating element in the 10- μm wide bimorph beams is a set of 200 μm long, 7 μm wide, polysilicon strips oriented along the beams. The gaps between the beams are 9 μm and used to undercut silicon to form thin-film bimorph beams. The frame actuator and mirror actuator are constituted of 20 and 12 bimorph beams, respectively. The measured open circuit polysilicon resistances of the mirror and frame actuators are 240 Ω and 365 Ω , respectively.

The mirror plate is 190 μm by 190 μm . This small mirror size is just used to demonstrate the proof of concept. Since the mirror plate is supported by bulk silicon, much larger mirrors can be made. The quality of the mirror surface was determined using a Wyko NT1000 white-light optical profilometer. A line scan of surface heights across the mirror plate is shown in Figure 4-5. The peak-to-valley surface deformations are within 40 nm over the 190 μm mirror plate. The optical quality of the mirror is better than $\lambda/20$ for near-infrared light.

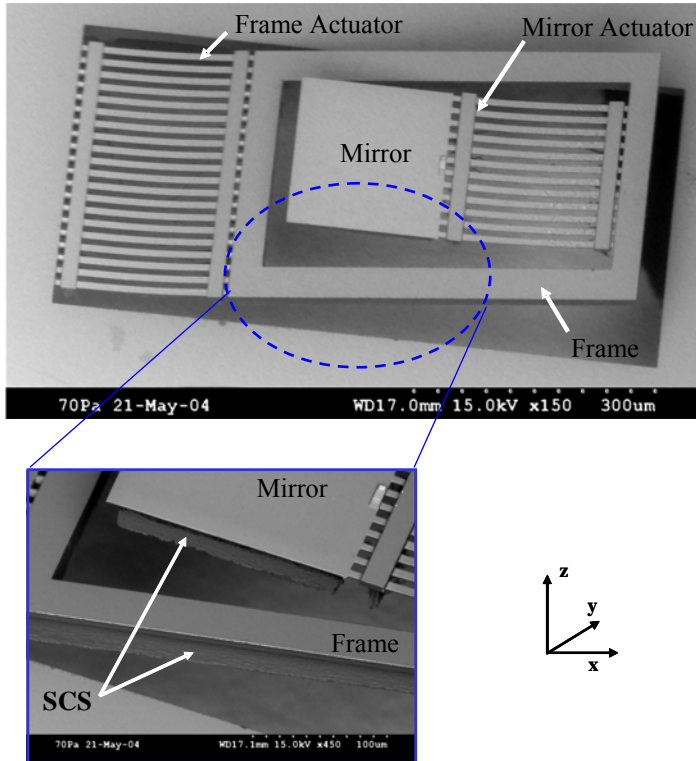


Figure 4-4: SEM images of the LVD micromirror.

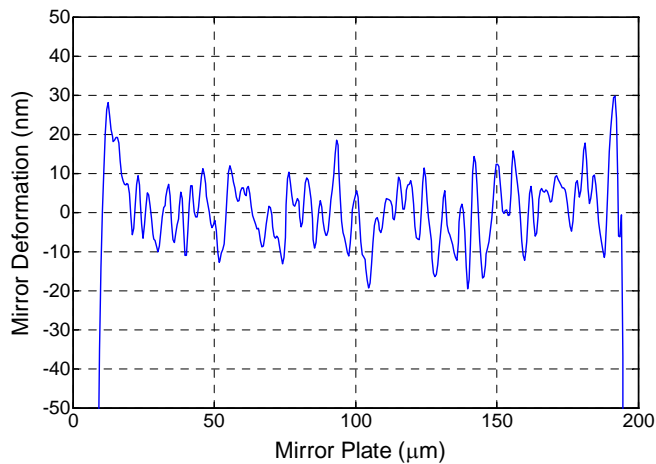


Figure 4-5: Line scan of the surface profile of the LVD micromirror.

4.2.2 Equivalent Circuit Model

Modeling an electrothermal actuator involves multiple domains (*i.e.*, electrical, thermal and mechanical). Since most of the actuator's electrical properties are temperature dependent, electrothermal coupling makes the modeling very challenging especially in the case where self-heating elements are used. For instance, in the case of a

bimorph cantilever beam with an embedded resistor, electrical current causes Joule heating of the resistor which generates a temperature distribution along the beam. Conversely, this temperature gradient along the beam produces non-uniform Joule heating of the resistor due to a finite temperature coefficient of resistance of the resistor material.

The operation of the micromirror has been modeled by using an equivalent electrical circuit, as presented in Figure 4-6, by partitioning the individual components of the device into electrical and thermal domains. This multi-domain model [128] simulates the electro-thermal behavior of the LVD actuators by considering the change in the polysilicon heater resistances, thermal coupling between the actuators, and heat loss by thermal convection. The unit of the product of the across and through variables in the thermal domain is Watts-Kelvin, while the thermal current has dimensions of power. Joule heating generated by the electrical resistor is modeled as a dependent current source in this thermal domain. Additional details about this electrothermal model developed by Todd and Xie are available in [128].

This model is valid when only one of the two actuators is activated. The subscript i in the parameters denotes the actuator that is activated and j denotes the other actuator

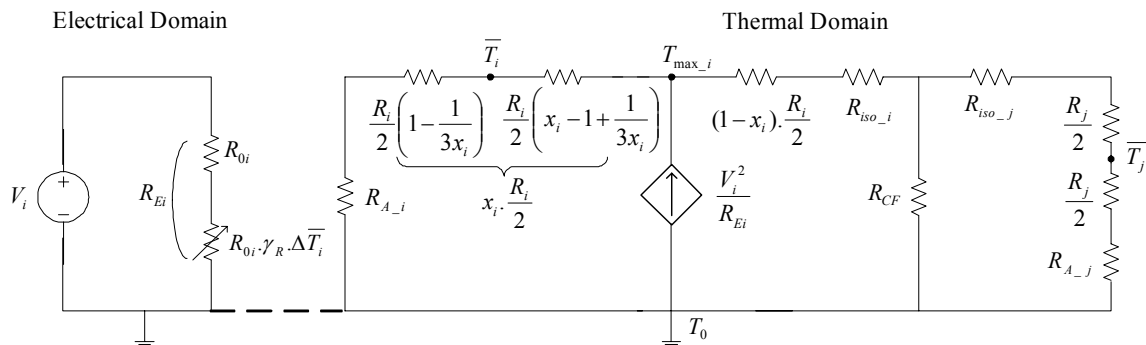


Figure 4-6: Equivalent circuit model of the LVD micromirror device. Voltage is only applied to actuator i , and actuator j is always grounded.

with zero applied voltage. Therefore we just need to consider two cases: 1) the mirror actuator is activated, i.e., $i = \text{MA}$ and $j = \text{FA}$; and 2) the frame actuator is activated, i.e., $i = \text{FA}$ and $j = \text{MA}$.

In the electrical domain, the electrical resistance of actuator i , R_{Ei} is temperature-dependent and is given by

$$R_{Ei} = R_{0i} \left[1 + \gamma_R \Delta \bar{T}_i \right] \quad (4-2)$$

where R_{0i} is the electrical resistance of the polysilicon heater at the substrate temperature T_0 , γ_R is the thermal coefficient of resistance of polysilicon, and $\Delta \bar{T}_i = \bar{T}_i - T_0$, where \bar{T}_i is the average temperature of actuator i .

In the thermal domain, the thermal resistance, R_T , is directly analogous to electrical resistance, and can be computed for different parts of the mirror by using the following expression:

$$R_T = \frac{\ell}{\kappa w t} \quad (4-3)$$

where κ , ℓ , w and t are the thermal conductivity, length, width and thickness of the thermal resistor, respectively. The various thermal resistors used in the equivalent circuit model of Figure 4-6 are defined in Table 4-1.

In the circuit model shown in Figure 4-6, using Kirchoff's current law, it can be easily shown that the average temperature of the bimorph beams of the actuator i is given by:

$$\bar{T}_i = \frac{1}{2\gamma_R} \left(\sqrt{\frac{4\gamma_R \bar{R}_{Ti}}{R_{0i}} x_i V_i^2 + 1} - 1 \right) \quad (4-4)$$

Table 4-1: Parameters used by the equivalent circuit model of the 1-D LVD micromirror.

Parameter	Description
<i>Electrical Domain</i>	
V_i	Voltage applied to actuator i
R_{Ei}	Electrical resistance of actuator i at temperature \overline{T}_i
R_{0i}	Resistance of actuator i at substrate temperature, T_0
γ_R	Thermal coefficient of resistance of polysilicon
<i>Thermal Domain</i>	
R_i	Thermal resistance of actuator i
R_j	Thermal resistance of actuator j
R_{CF}	Resistance of frame due to convection
R_{CM}	Resistance of mirror plate due to convection
R_{iso_i}	Resistance due to thermal isolation of actuator i
R_{iso_j}	Resistance due to thermal isolation of actuator j
T_{max_i}	Maximum temperature of actuator i
\overline{T}_i	Average temperature of actuator i
\overline{T}_j	Average temperature of actuator j
Where: $i = \{m, f\}$, $j = \{f, m\}$, and $i \neq j$	
$x_m = 0.5$	$x_f = 0.66$
$R_{Am} = R_{iso_m} + R_{CM}$	$R_{Af} = R_{iso_f}$

where x_i denotes the position of the maximum temperature of the actuator i . and can be determined by thermal imaging or by the burn pattern of actuator i . Todd and Xie determined the maximum temperature position on the 1-D micromirror actuator by using high-resolution thermal imaging [128]. The value of x_i can also be determined by the position of the burn pattern of actuator i . For this analysis, electrical current flowing through the actuator was increased till burn marks appeared on the surface of the bimorph metal layer.

The value of x_i was obtained from the SEM image of Figure 4-7 as:

$$x_i = \frac{l_i}{L_b} \quad (4-5)$$

where, l_i is the distance of the actuator i burn pattern from its anchor location, and L_b is the length of the bimorph actuator.

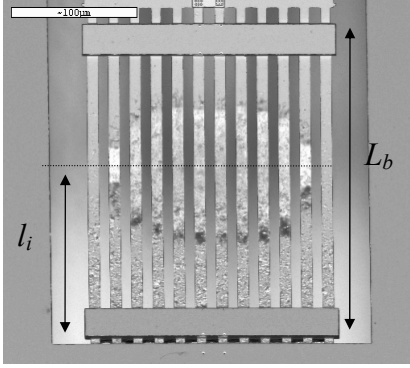


Figure 4-7: SEM of the burn pattern of the mirror actuator. The value of x_i is calculated as: $x_i = l_i/L_b$. [Equation (4-5)]

Using the analysis presented by Todd and Xie [128], \bar{R}_{Ti} , the equivalent average thermal resistance of the actuator i , can be expressed as :

$$\bar{R}_{Ti} = \frac{R_i}{2} \left(1 - \frac{1}{3x_i} \right) + R_{A-i} \quad (4-6)$$

The average temperature, \bar{T}_j , of the inactive actuator j can be computed in a similar manner.

As discussed in Section 3.4, the rotation angle of each actuator is given by:

$$\theta_k = \frac{6l(t_{Al} + t_{ox})(\alpha_{Al} - \alpha_{ox})(\bar{T}_k - T_0)}{4t_{Al}^2 + 4t_{ox}^2 + 6t_{Al}t_{ox} + \frac{E_{Al}t_{Al}^3}{E_{ox}t_{ox}} + \frac{E_{ox}t_{ox}^3}{E_{Al}t_{Al}}} \quad (4-7)$$

where, $k = MA$ or FA , l is the length of the bimorph actuator, and t_a , α_a and E_a are the thickness, thermal coefficient of expansion, and Young's modulus of the metal ($a=Al$) and oxide ($a=ox$) layers, respectively.

Therefore the net rotation of the mirror is obtained by plugging the values of \bar{T}_i and \bar{T}_j into Equation (4-7) and solving as:

$$\theta_{rot} = \theta_i - \theta_j \quad (4-8)$$

As seen in Equation (4-8), this model considers the rotation of the inactive actuator j due to thermal coupling between the two actuators.

From Equation (4-4) it is observed that the average temperature of the bimorph actuator becomes approximately linear with voltage when the applied voltage is above a certain threshold value. This linear relationship between the average temperature change and applied voltage is represented as:

$$\Delta\bar{T}_i(V) = \sqrt{\frac{x_i \bar{R}_{Ti}}{\gamma_R R_{0i}}} \cdot V \quad \text{when} \quad V \gg \sqrt{\frac{R_{0i}}{4\gamma_R \bar{R}_T x_i}} \quad (4-9)$$

Combining Equation (4-9) with Equation (3-6) yields the linear relation between the actuation angle and the applied voltage as given below.

$$\theta_T = \beta_r L_b \Delta\alpha_T \sqrt{\frac{x_i \bar{R}_{Ti}}{\gamma_R R_{0i}}} \cdot V \quad (4-10)$$

where L_b is the length of the bimorph beam. This linear relation is very important for practical use, and experimental verification will be presented in the next section.

4.2.3 Experimental Results

4.2.3.1 Static response

The same experimental setup used for the 2-D micromirror characterization from Section 3.5.2.2 was used to characterize this LVD micromirror. The mirror plate of the LVD micromirror rotates 26.5° when 3 V dc is applied to the mirror actuator. The mirror plate and the frame both rotate when a voltage is applied only to the frame actuator due to

thermal coupling effects. The mirror plate rotates -16.5° when 5.5 V dc is applied to the frame actuator.

As shown in Figure 4-8(a), the rotation angles of the actuators vary linearly with applied voltages after the applied voltages are above the small threshold voltages. The rotation-angle response plot can be explained using Equation (4-4) which was derived from the equivalent circuit model of the device. Rotation by a bimorph actuator is proportional to its applied electrical power, i.e., it is proportional to the square of the applied voltage, V (since $P = V^2/R$). Note that the electrical resistance, R is not constant and increases linearly with increasing temperature due to a non-zero thermal coefficient of resistance of the polysilicon heater. Therefore, the angular response has an initial nonlinear V^2 -like dependence, as seen in Figure 4-8(a) and in Equation (4-4) at low voltages. Consistent with the analysis presented in the preceding section, one can see that after a threshold voltage is crossed (Equation (4-9)), the rotation angle can be approximated to be linearly proportional to the applied voltage. The simulation results using the equivalent circuit model match the experimental data to within 8% in the $\pm 15^\circ$ rotation range, as shown in Figure 4-8(a).

The same actuation voltage causes a larger rotation angle by the mirror actuator than the frame actuator due to the polysilicon resistance difference between the two actuators, and also because the mechanical structure of the frame provides additional thermal isolation to the mirror actuator. The polysilicon resistances of the bimorph actuators change with applied voltages, which are plotted in Figure 4-8(b). The large resistance change is caused by the large temperature coefficient of resistance (TCR) of polysilicon. As evident from Figure 4-8(c), there exists a linear correlation between the

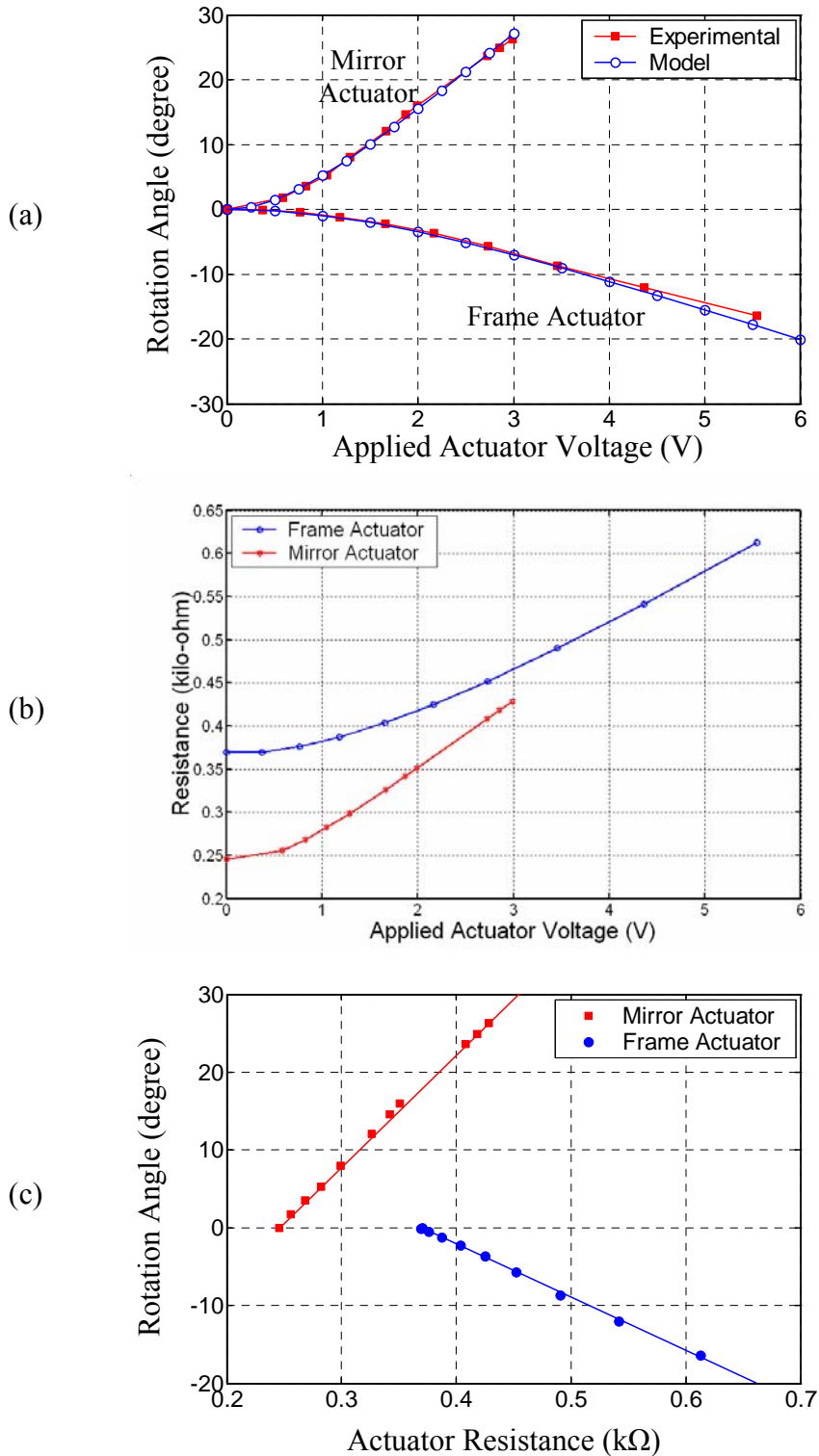


Figure 4-8: LVD mirror characterization. Plots of the (a) rotation angle versus applied voltage, and (b) polysilicon heater resistance versus applied voltage for the two actuators. (c) Plot showing the linear correlation between rotation angle and polysilicon resistance of the actuators.

rotation angle and the polysilicon resistance for each of the two actuators. The nonlinearity is less than 2% and is within the rotation-angle measurement error. This linear relationship allows for independent control of rotation angle of each actuator by monitoring its polysilicon heater resistance. Thermal coupling between the two actuators can also be accounted for by monitoring their individual polysilicon heater resistances.

Large piston motion of the mirror can be achieved by equal but opposite angular rotations of the two actuators. By using the rotation-angle versus actuation-voltage data, a mirror-actuator drive-voltage versus frame-actuator drive-voltage plot for same angular rotation values can be obtained. The slope of this experimentally determined plot provides the driving voltage ratio for the two actuators that would maintain no tilting of the mirror plate. A voltage divider was used to drive the two actuators with a voltage ratio of 3:7 (determined from experiment). A maximum vertical displacement of 200 μm was obtained. The vertical displacement of the mirror as a function of the drive voltage is shown in Figure 4-9(a). By using a linearly-fitted voltage ratio, about 1° tilting of the mirror plate was observed during the full-range vertical actuation. A 2nd-order polynomial-fitting, as shown in Figure 4-9(b), can be used to further reduce the tilting to less than 0.03° . The tilting of the mirror plate during this experiment was monitored by using a quadrant photodetector.

4.2.3.2 Frequency response/resonant scanning

The frequency response of the LVD micromirror was measured using a Polytec OFV-511 laser Doppler vibrometer, as shown in Figure 4-10. Resonant peaks were observed at 1.12 kHz and 2.62 kHz. These results are a close match to the modes observed at 1.14 kHz and 2.76 kHz from simulations using CoventorWare. When current is passed only through the

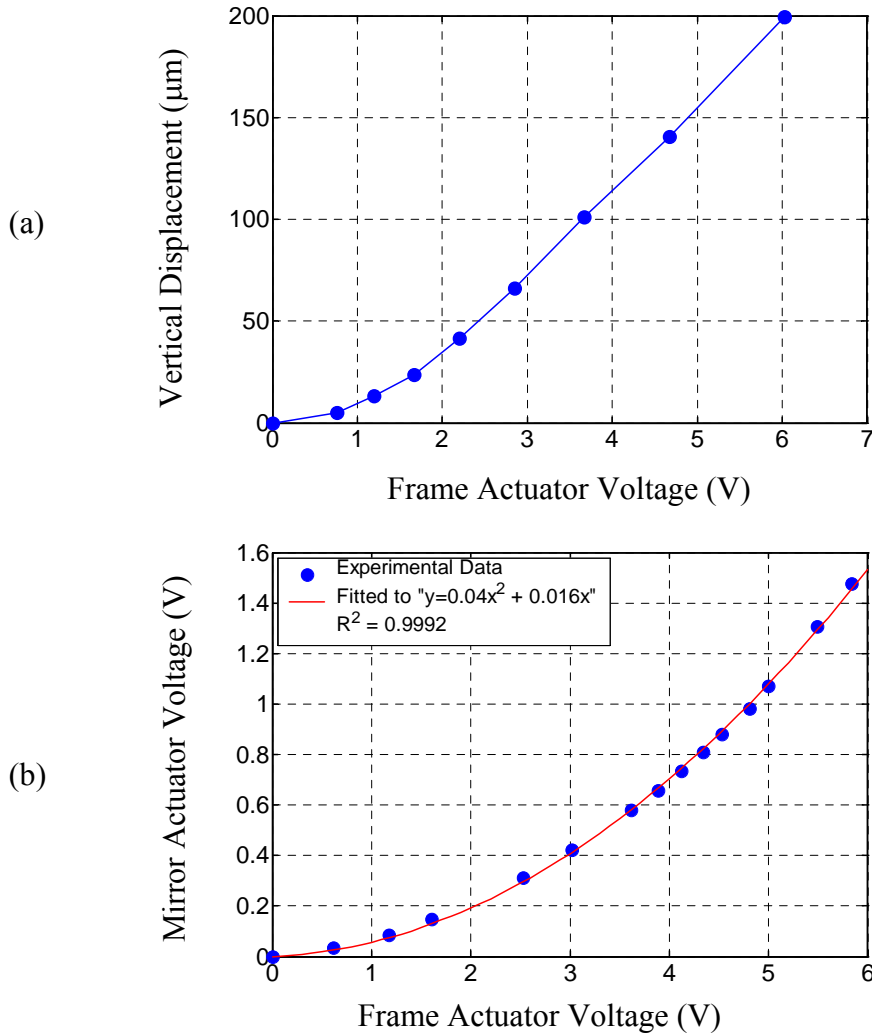


Figure 4-9: Piston motion mode. (a) Vertical displacement of the mirror plate as a function of the frame actuator voltage. (b) Plot of the mirror actuator voltage versus frame actuator voltage that was used to drive the LVD device to obtain less than 0.03° tilting of the mirror plate.

mirror actuator at its resonance, the mechanical resonance of the mirror structure (Q-factor of 25) generates bi-directional scans. At the resonance frequency of 2.6 kHz, the optical angle scanned by the mirror is 170° at a dc plus ac drive voltage of $(0.6 + 0.6\sin\omega t)$ V. Scan angles greater than 170° were observed visually at marginally higher voltages, but could not be monitored since the reflected light beam is blocked by the package sidewall. This large-angle scanning is stable and repeatable.

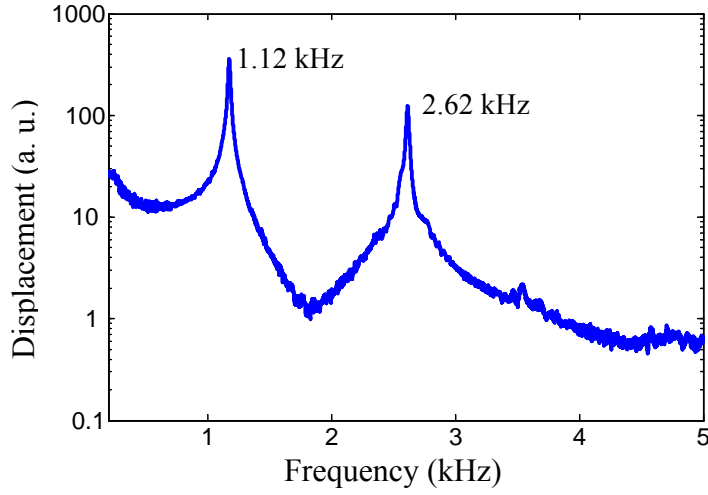


Figure 4-10: Frequency response of the LVD micromirror device.

Frequency doubling: In response to the applied ac voltage signal, the power, P_{ac} dissipated by the actuator is given by:

$$P_{ac} = \frac{\tilde{V}_{ac}^2}{R[T(P_{ac})]} = \frac{V_{ac}^2 \sin^2 \omega t}{R[T(P_{ac})]} = \frac{V_{ac}^2}{2.R[T(P_{ac})]} (1 - \cos 2\omega t) \quad (4-11)$$

where R is the polysilicon resistance of the actuator. Therefore, frequency doubling is observed when the device is actuated by only an ac voltage signal. Note that the polysilicon resistance R does not remain constant, but actually increases with increasing power due to a non-zero thermal coefficient of resistance.

In order to reduce the effect of frequency doubling, a dc bias is added to the applied ac voltage signal, and the power dissipated is given by:

$$P_{ac+dc} = \frac{(V_{dc} + V_{ac} \sin \omega t)^2}{R} = \frac{V_{dc}^2 + V_{ac}^2}{R} + \frac{2V_{dc}V_{ac}}{R} \sin \omega t - \frac{V_{ac}^2}{R} \cos 2\omega t \quad (4-12)$$

By increasing the dc bias V_{dc} above the threshold voltage given in Equation (4-9), the device operates in the linear region. In this operation region, the angular response is

directly proportional to the applied voltage, so the effect of frequency doubling can be significantly reduced.

4.3 2-D LVD Micromirror

4.3.1 Mirror Design

A schematic view of the 2-D micromirror with its nomenclature is illustrated in Figure 4-11. The 0.5mm-by-0.5mm mirror plate is attached to a rigid silicon frame by a set of bimorph aluminum/silicon dioxide thin-film beams. This first set of bimorph beams is referred to as actuator 1 (Act1). As shown in Figure 4-11(c), polysilicon resistors embedded in the bimorph beams are used for electrothermal actuation. This frame is connected to a second outer frame by another set of identical bimorph thin-film beams, known as actuator 2 (Act2). Act1 and Act2 together form a large-vertical-displacement (LVD) microactuator set, in which the curls of the two sets of bimorph beams compensate each other resulting in zero initial tilt of the mirror plate. A detailed analysis on LVD microactuators has already been reported in the preceding sections. Bi-directional 1-D line scanning along the y-axis is possible using this LVD microstructure by alternately applying voltage to actuators Act1 and Act2. In order to enable 2-D scanning, a second set of LVD actuators (Act3 and Act4) is attached to the first, as shown in Figure 4-11(a). The orthogonal orientation of the two sets of LVD actuators results in two perpendicular axes of rotation for the micromirror.

As seen in the SEM of the 2-D LVD mirror [143] in Figure 4-12, the initial tilt angle of a fabricated mirror plate is less than 0.5° , and its rest position is 1.24 mm above the substrate plane. Each side of the three rectangular frames is 40 μm wide, and has a

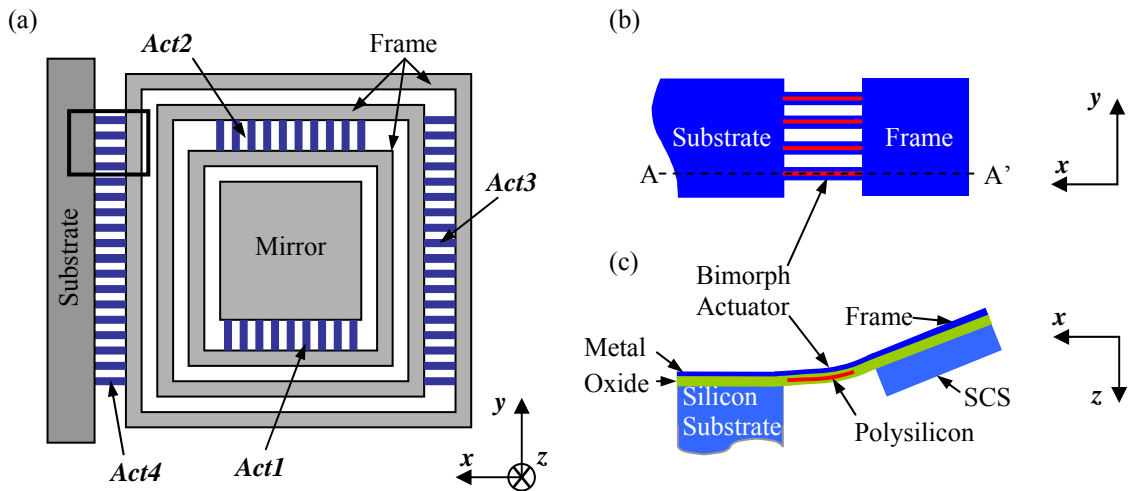


Figure 4-11: 2-D LVD micromirror design. (a) Top view of the 2-D micromirror, highlighting the 4 bimorph actuators. (b) Top view of the actuator area boxed in part (a). (c) Cross-sectional view of the bimorph actuator as seen across A-A'.

40- μm -thick SCS layer under it to provide rigidity and thermal conduction to the substrate. The heating element in the bimorph beams is a set of 200- μm -long, 7- μm -wide polysilicon strips oriented along the beams. The primary mirror-rotation directions for actuators 1, 2, 3, and 4 are along the $+y$, $-y$, $+x$, and $-x$ axes, respectively. However, the

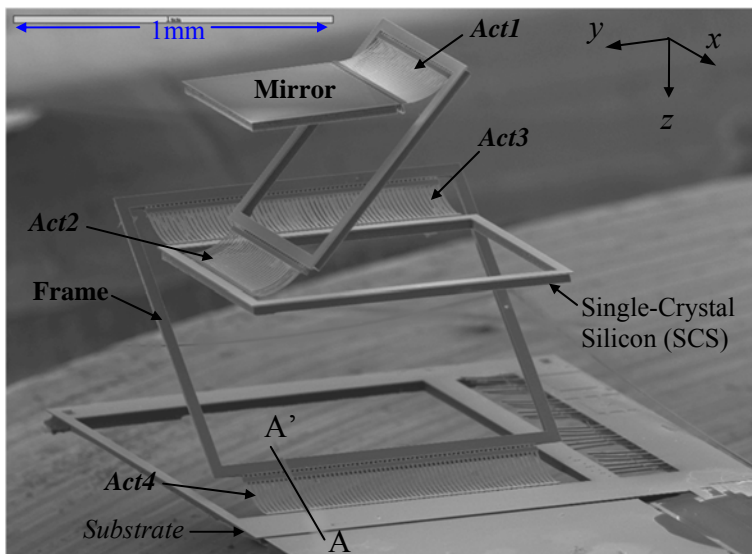


Figure 4-12: SEM of a fabricated 2-D LVD mirror. The cross-sectional view of A-A' is shown in Figure 4-11(c).

heating of the active actuators will cause unwanted rotations by the other actuators due to thermal coupling. This issue will be discussed in the next section.

4.3.2 Experimental Results

4.3.2.1 Bi-directional scanning

An experimental setup with a laser beam incident on the mirror and dc voltages applied to the four actuators was used to determine the static 2-D scanning response of each actuator. The optical angle scanned by the mirror was determined by measuring the displacement of the reflected laser beam on a calibrated x - y screen. Figure 4-13(a) shows the static 2-D line scans obtained by actuating each actuator individually, in which only *Act4* scans along its primary axis while the other scan lines deviate from their primary axes. The corresponding scan-angle versus actuation-voltage characteristics for each of the four actuators are shown in Figure 4-13(b). *Act4* scans along the $-x$ axis, while *Act1*, *Act2* and *Act3* scan 1-D lines angled at $+60^\circ$, -66° , and -28° with respect to the x -axis, respectively. This 2-D micromirror device scans optical angles greater than $\pm 40^\circ$ in the x -direction, and over $\pm 30^\circ$ in the y -direction at dc actuation voltages less than 12 V. The deviation of a line scan from its primary axis in Figure 4-13(a) is caused by thermal coupling between the actuators. Since *Act4* is directly connected to the silicon substrate it is least affected by thermal coupling, and this can be observed in Figure 4-14(a), where *Act4* scanned consistently along the $-x$ direction for different *Act1* bias voltages. The thermal coupling between the actuators can be modeled by extending the LVD electrothermal model reported in Section 4.2.2.

The resistances of the polysilicon heaters embedded in all four actuators increase significantly with applied voltage because of Joule heating. The measured polysilicon

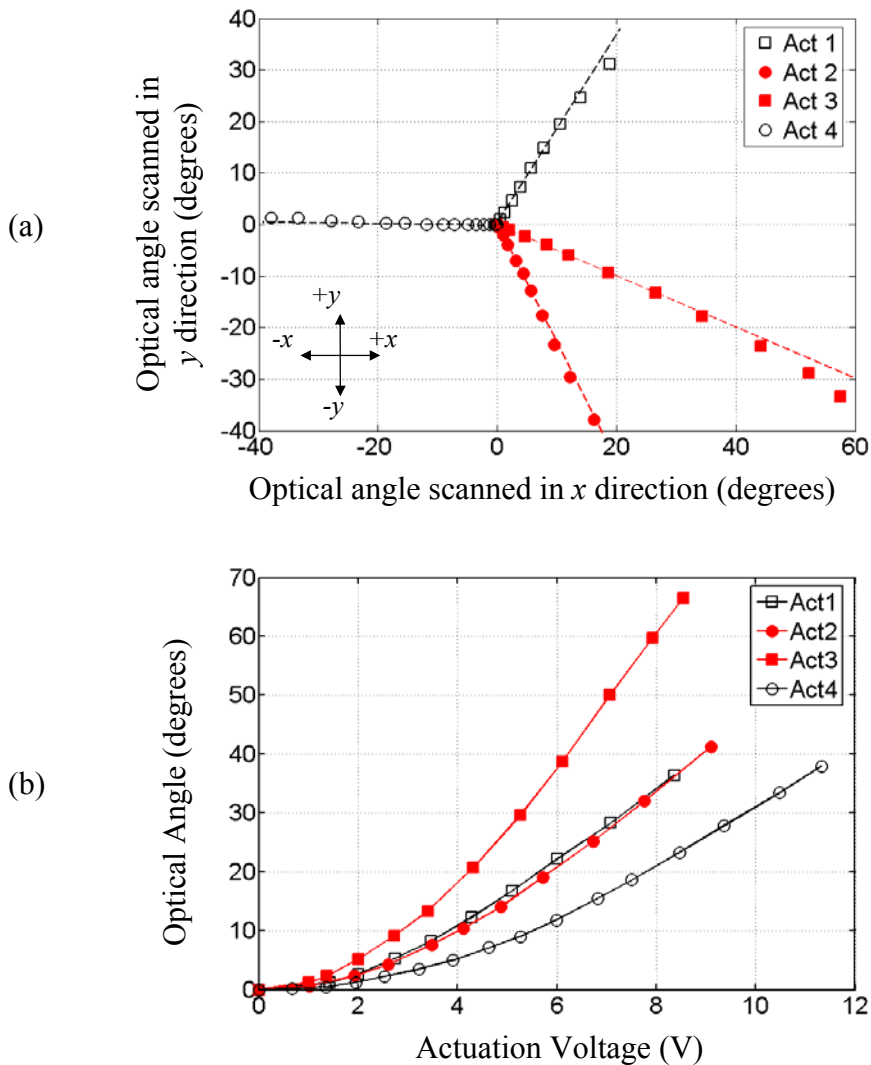


Figure 4-13: Static 2-D line scans. (a) Plot showing the optical angles scanned in 2-D space when each actuator is individually actuated. (b) Plot of the effective optical angle scanned versus actuation voltage for each actuator. *Act4* scans along $-x$, while *Act1*, *Act2* and *Act3* scan at $+60^\circ$, -66° , -28° with respect to the x -axis, respectively.

resistance of each actuator is listed in Table 4-2. A linear correlation between the optical scan angle and the polysilicon resistance for each of the four actuators was observed, as shown in Figure 4-14(b). This correlation allows for independent control of the rotation angle of each actuator by monitoring the resistance of each individual polysilicon heater.

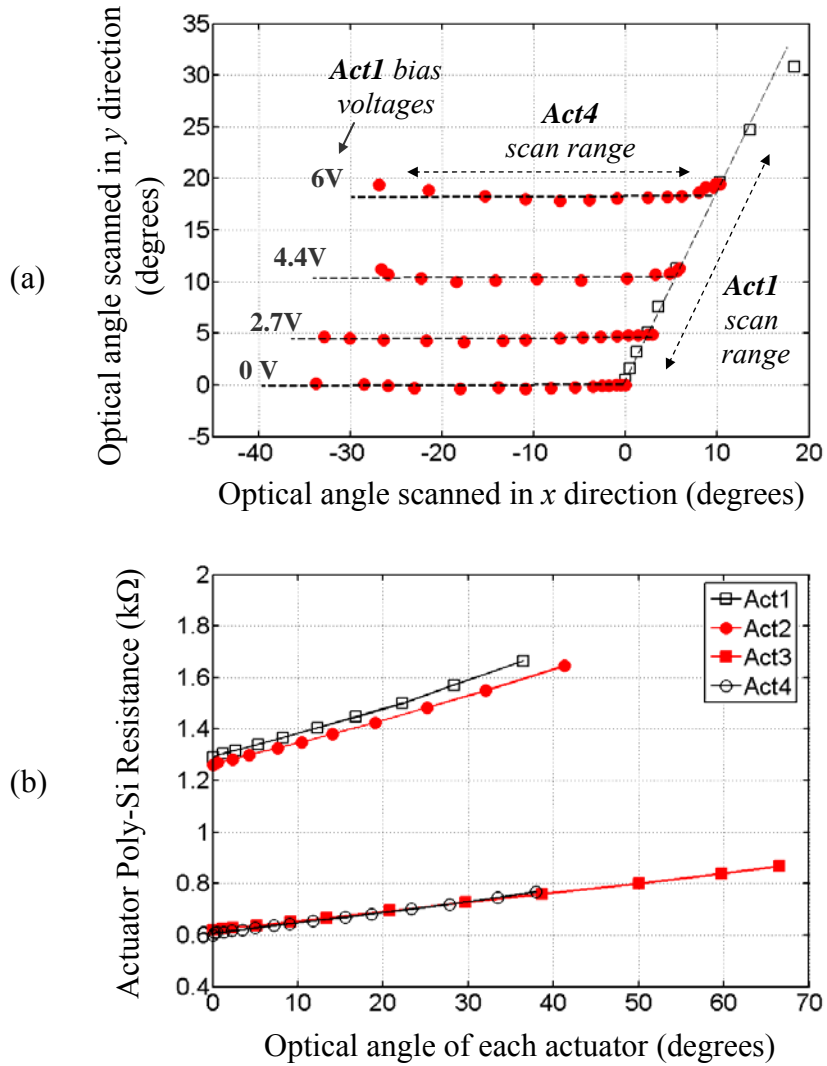


Figure 4-14: Static characterization. (a) Plot showing the linear scan pattern during static 2-D scanning of *Act1* and *Act4* only. *Act4* was actuated at different *Act1* bias voltages. (b) Linear plot of actuator resistance versus optical scan angle for each actuator.

Table 4-2: Actuator characteristics for the 2-D LVD micromirror.

Actuator	Heater Resistance	Maximum Static Optical Scan Angle	Mirror Rotation Direction	Resonant Frequency
<i>Act1</i>	1.3 k Ω	36° at 8.4 V	-30° to +y-axis	870 Hz
<i>Act2</i>	1.3 k Ω	41° at 9.1 V	24° to -y-axis	452 Hz
<i>Act3</i>	0.62 k Ω	66° at 8.5 V	-28° to +x-axis	312 Hz
<i>Act4</i>	0.62 k Ω	38° at 11.4 V	along -x-axis	170 Hz

Thermal coupling between the actuators can also be accounted for by monitoring the individual polysilicon heater resistances.

The angular stability of the micromirror (at its maximum xy tilt angle) was experimentally determined with respect to time, as shown in Figure 4-15. From this plot it was determined that the micromirror stability for *Act1* and *Act4* were within 0.6° and 0.16° , respectively, for their entire optical scan ranges (which are 36° and 38°).

The initial tilt angle of the mirror plate at different environmental temperatures was also documented, and the results are presented in Figure 4-16. For this experiment, the micromirror was heated by a thin-film micro-heater placed under a packaged device, and the tilting of the mirror plate at different temperatures was optically monitored.

Theoretically, a uniform change in device temperature would cause equal rotational displacements by all four actuators, thereby negating any net mirror tilting. However, as observed in Figure 4-16, there is significant mirror tilting in the $-x$ direction and this is

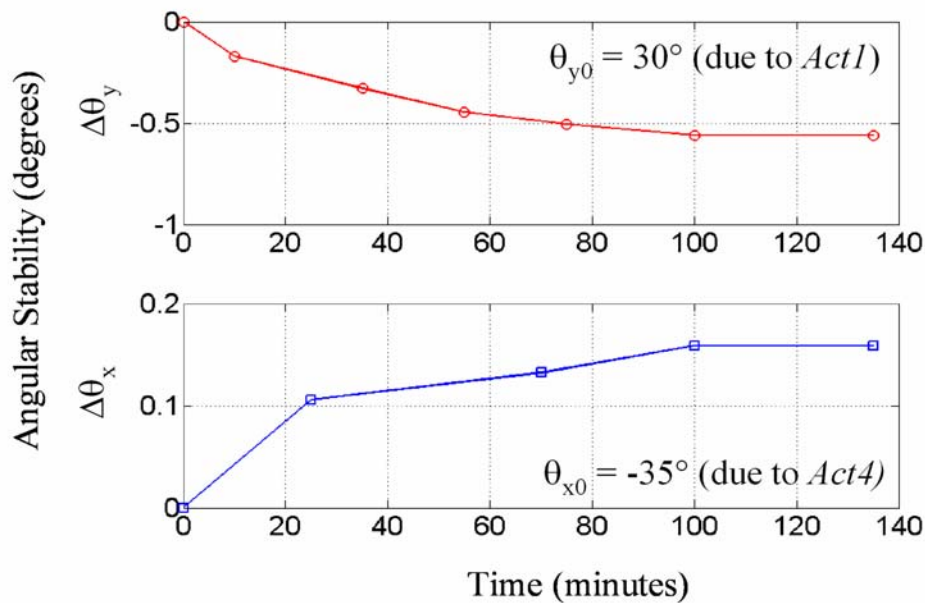


Figure 4-15: Tilt angle stability of the mirror plate versus time. Act1 and Act4 were excited to rotate the mirror to its maximum scan angle.

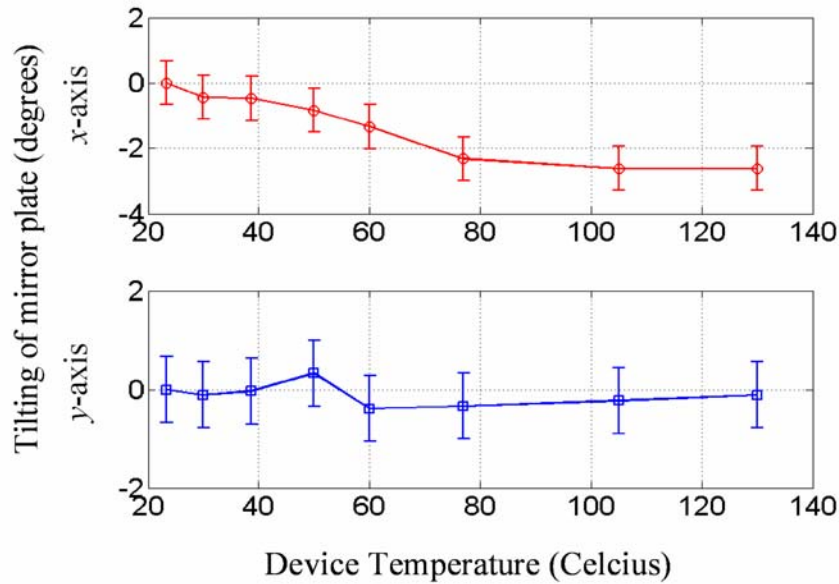


Figure 4-16: Initial tilt angle of the mirror plate in x and y directions at different environmental temperatures.

attributed to the fact that *Act4* is heated more than the other actuators since it is directly connected to the substrate, which in turn is directly connected to the heat source.

4.3.2.2 Two-dimensional dynamic scanning

2-D scanning using this device was demonstrated by simultaneously exciting both *Act1* and *Act4* actuators with small ac voltage signals. The frequency and phase of the ac signals were varied in order to generate the Lissajous figures shown in Figure 4-17. This device exhibits resonant peaks at 870 Hz, 452 Hz, 312 Hz, and 170 Hz due to the different actuators as summarized in Table 4-2.

A 2-D raster-scanning pattern was generated by the micromirror when *Act1* was supplied with 1 Vdc plus 1 Vac at its resonance of 870 Hz, and *Act4* was supplied with 2 Vdc plus 2 Vac at 15 Hz. As shown in Figure 4-18, 58 parallel lines were scanned in a raster-scan pattern by the laser beam covering a 14° by 50° parallelogram angular area.

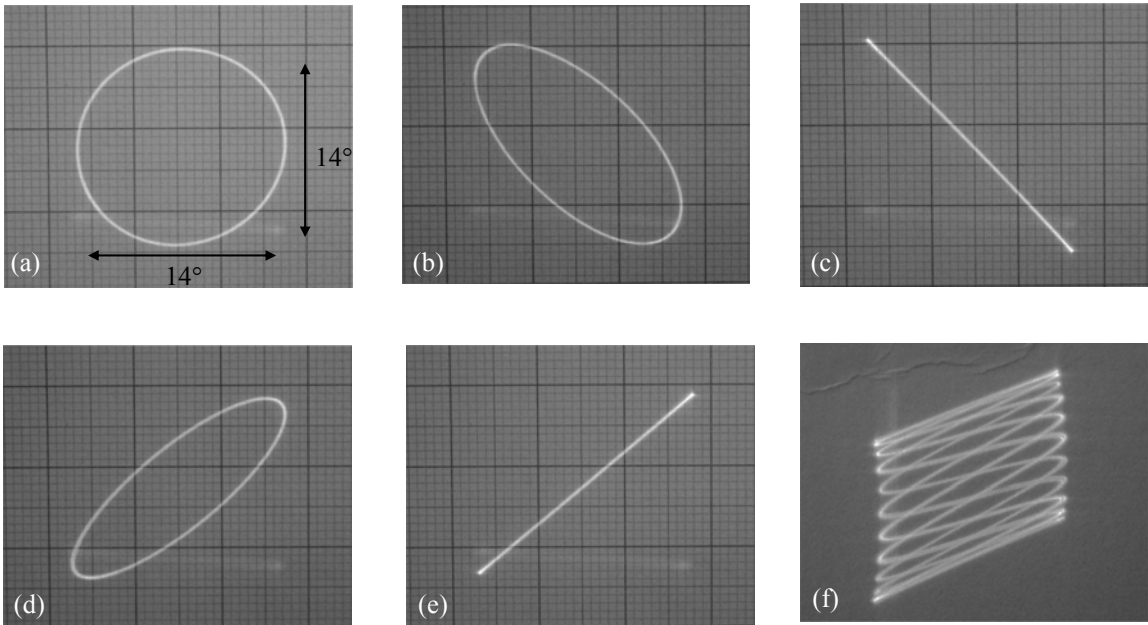


Figure 4-17: Photographs of 2-D scan patterns obtained by exciting actuators 1 and 4 only. (a)-(e) Lissajous figures scanned by the micromirror by varying only the phase of the two excitation signals. (f) Lissajous figure scanned at an excitation frequency ratio of 1:10.

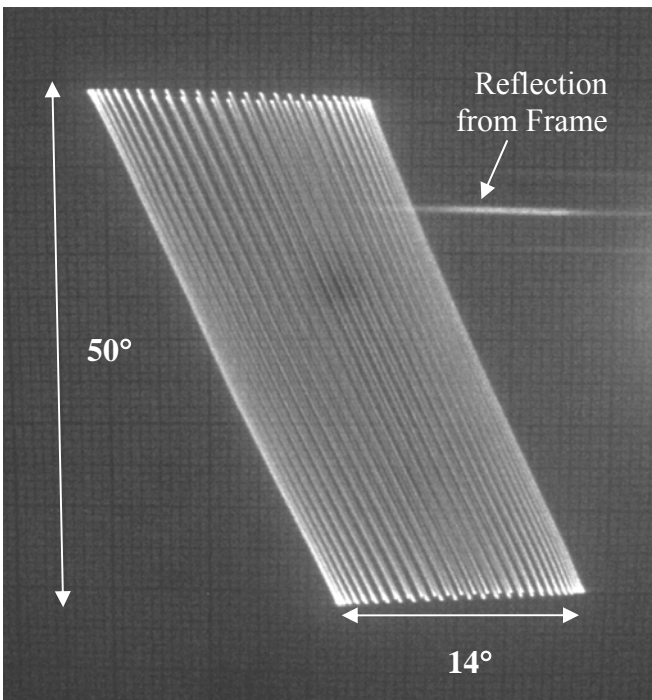


Figure 4-18: 2-D raster scanning pattern obtained using actuators 1 and 4.

4.3.2.3 Vertical displacement motion

Vertical displacement of the mirror plate can be achieved by equal but opposite angular rotations of only one set of LVD microactuators. For this experiment, only actuators 3 and 4 were used. The *Act3* actuation voltage was increased in small increments to rotate the mirror plate in the $+x$ direction. This $+x$ -direction mirror rotation was compensated by supplying voltage to *Act4*, which rotates the mirror along the $-x$ direction. The opposite rotations brought about by actuators 3 and 4, result in pure vertical displacement of the micromirror along the $+z$ direction. It should be noted that due to thermal coupling, the inactive actuators 1 and 2 will tilt the mirror plate along the y direction. The vertical displacement of the center of the mirror plate as a function of *Act4* voltage is shown in Figure 4-19(a). It can be seen that a maximum z -displacement of 0.53 mm was observed at an *Act4* voltage of 15 V. Figure 4-19(b) shows the almost linear relationship between the *Act3* voltage and the corresponding *Act4* voltage that is required to vertically displace the micromirror as obtained in Figure 4-19(a). Using this voltage relationship, the x -axis tilting of the mirror plate was less than 0.8° during the entire 0.53 mm actuation range. An almost linear correlation between the vertical displacement of the mirror plate and the actuator resistances was observed, as shown in Figure 4-19(c). This linear relationship provides a closed-loop feedback path for determining mirror displacement by monitoring the actuator resistances. The z -axis vertical scan provided by actuators 3 and 4, in combination with the y -axis resonance scan provided by *Act1* will generate 2-D scans in the y - z plane.

As mentioned above, thermal coupling between the active *Act3* and *Act4* actuators causes rotation by *Act1* and *Act2* in the orthogonal y -direction. This y -axis tilting of the

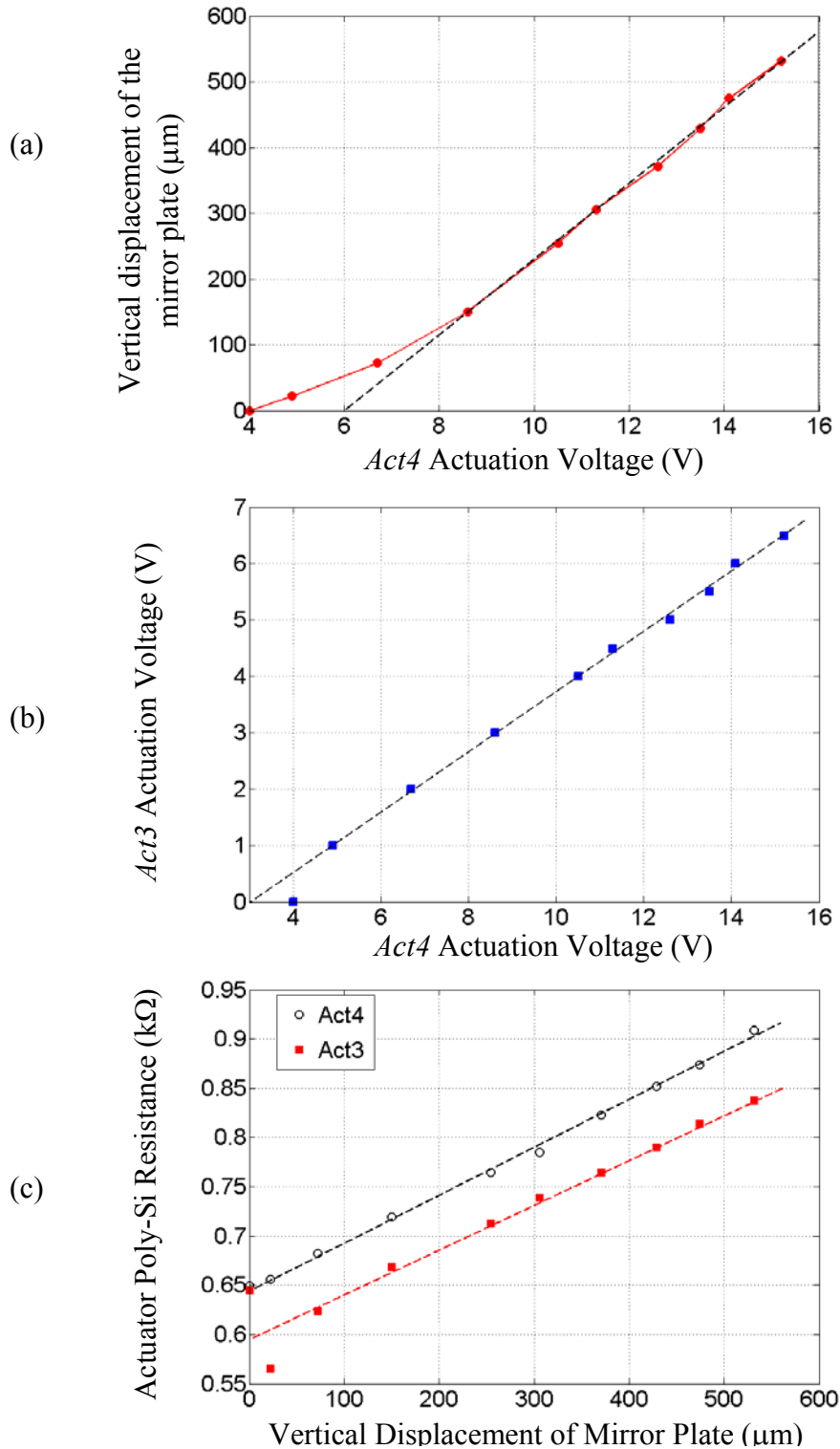


Figure 4-19: Piston motion mode. (a) Vertical displacement of the mirror plate as a function of *Act4* voltage. (b) Corresponding plot of the relationship between *Act3* and *Act4* voltages that is required to generate the vertical displacement. (c) Linear increase of *Act3* and *Act4* resistance with vertical displacement.

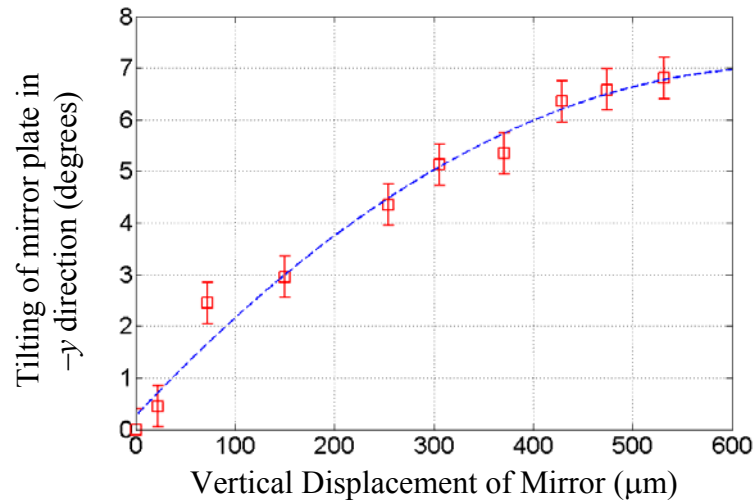


Figure 4-20: Tilting of the mirror plate in the negative y -direction (due to thermal coupling) as a function of vertical position of the mirror.

mirror plate was monitored and is plotted as a function of vertical displacement in Figure 4-20. A maximum y -direction mirror-plate tilting of -7° was observed. This $-y$ mirror tilting is mainly due to the heating of *Act2* by the *Act3* and *Act4* active actuators. Even with thermal coupling it is possible to scan a 2-D depth scan using this mirror; however the scanned area would be displace towards the $-y$ direction with increasing z -displacement (as observed in Figure 4-20).

4.4 MEMS Mirror-based Nonlinear Endoscopy

Using MEMS mirrors for nonlinear optical imaging was demonstrated in collaboration with Ms. Ling Fu and Prof. Min Gu of the Centre for Micro-Photonics, Swinburne University of Technology, Hawthorn, Australia. MEMS mirrors have been used to facilitate endoscopic beam steering because of their small size, potentially low cost and excellent micro beam manipulating capacity.

4.4.1 Nonlinear Optical Imaging System

A schematic of the nonlinear imaging system is depicted in Figure 4-21. A Ti:Sapphire laser source at 800 nm (Spectra Physics Mai Tai) is used to generate ~ 80 fs pulses at a repetition rate of 80 MHz, and an output power of 850 mW. The laser pulses pass through an iris diaphragm, and are focused into a double-clad photonic-crystal-fiber using a microscope objective lens (40x /0.65 NA). The double-clad photonic crystal fiber (Crystal Fiber A/S) has a core diameter of 20 μm , an inner cladding diameter of 165 μm , an outer diameter of 550 μm , and a numerical aperture (NA) of 0.6 at a wavelength of 800 nm. This double-clad photonic crystal fiber is used for two purposes: the central core is used for single-mode propagation of the 800 nm near-infrared light from the laser source to the tissue sample, while the high NA inner cladding is used for efficient multimode propagation of visible light from the sample to the photodetector. The cross-section of this fiber is shown in Figure 4-22.

The excitation laser beam exiting from the double-clad photonic-crystal-fiber is scanned by a MEMS mirror onto the surface of the tissue sample. A 0.2-pitch GRIN lens

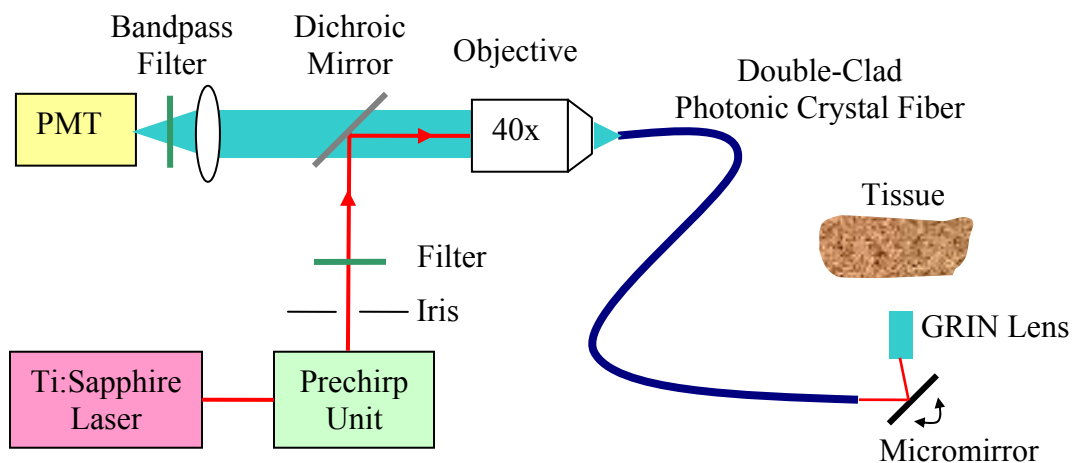


Figure 4-21: Schematic of the nonlinear optical imaging system.

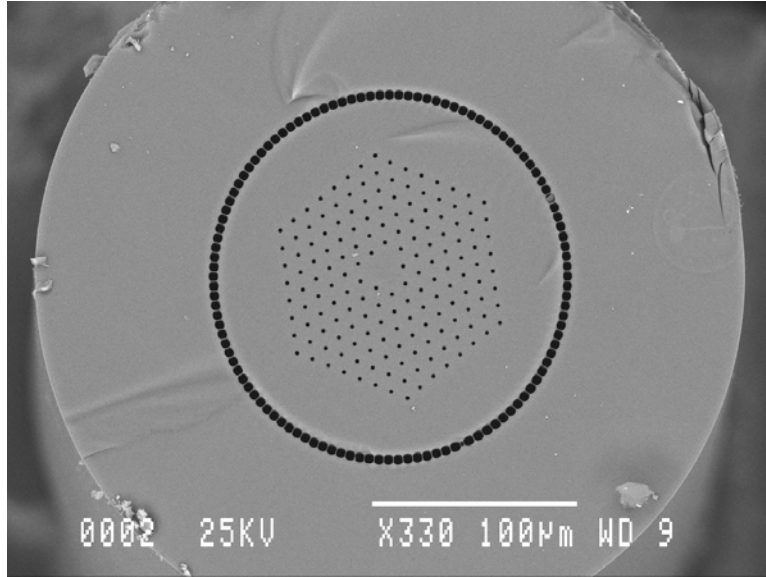


Figure 4-22: Cross-sectional view of the double-clad photonic crystal fiber. Imaged by L. Fu. Used with permission.

with a diameter of 1 mm (GRINTECH) is used to focus the laser beam to a diffraction-limited spot-size of $\sim 1 \mu\text{m}$ onto the tissue sample at a working distance of about 0.15 mm. The two-photon excitation fluorescence and second harmonic generated optical signals from the tissue are collected using the same GRIN lens and micromirror, and this UV/visible spectrum signal propagates through the inner cladding of the double-clad photonic crystal fiber before being detected by a photo multiplier tube (PMT) (Oriel, Model #77348). The detected signal is pre-amplified by an amplifier (Oriel, Model #70710), and then digitized using a data acquisition card. The lateral MEMS scans are synchronized with the image acquisition data through the use of a Labview program.

4.4.2 Experimental Results

The 1-D micromirror was used for SHG imaging as shown in the results of Figure 4-23. In this case, a 0.2-pitch GRIN lens with a diameter of 1 mm was used, and the resulting field-of-view on the sample was $35 \mu\text{m}$. This corresponds to an optical scanning

range requirement of only $\sim 6^\circ$ by the 1-D micromirror. A Labview program provides the 5V actuation signal to the micromirror to perform this angular scan. Since the laser beam is scanned at the back-surface of the GRIN lens, the GRIN lens is under-filled and this results in an axial resolution of about $10\ \mu\text{m}$. The optical power of the excitation laser beam on the tissue is approximately 30 mW. Figure 4-23(a) shows a series of SHG line profiles from the rat tail tendon, which are spaced at $10\ \mu\text{m}$ in the axial direction. A one-dimensional stage (Melles Griot) was used for the axial scanning. Figure 4-23(b) shows a SHG line profile from a rat esophageal tissue which was removed from a euthanized rat, immersed in Hank's balanced salt solution (no phenol red) and imaged directly without any staining.

In order to obtain more meaningful 2-D images, the 2-D LVD micromirror from Section 4.3 was used with the same nonlinear imaging system. The lateral raster scan pattern of this mirror was first characterized. Subsequently, a Labview program was written to supply control voltages to Actuators 1 and 4 only to obtain the 2-D scan

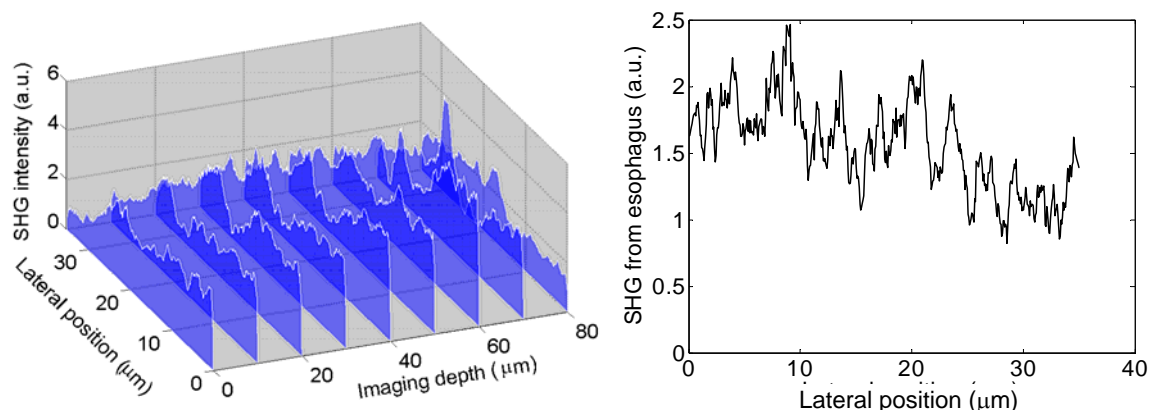


Figure 4-23: Second harmonic generation imaging. (a) Series of SHG line profiles from rat tail tendon taken at $10\ \mu\text{m}$ axial steps. (b) SHG line profile of an unstained rat esophagus tissue. Obtained by L. Fu. Used with permission.

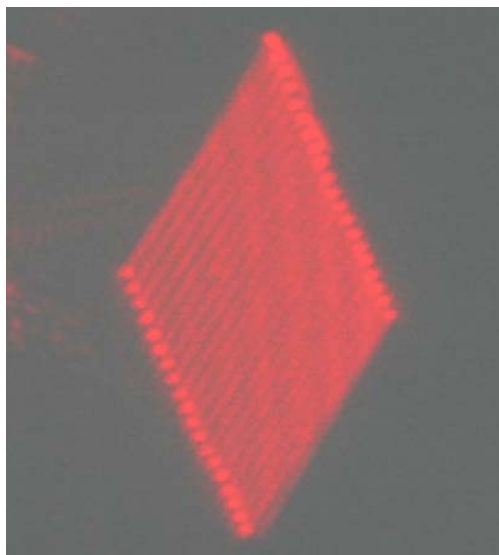


Figure 4-24: 2-D raster scan pattern scanned by actuators 1 and 4 only.

pattern shown in Figure 4-24. The nonlinear optical image was reconstructed according to the scanning calibration data. The 1-D mirror in the setup was replaced by the 2-D LVD mirror, and to demonstrate 2-D TPEF imaging 10 μm diameter fluorescent microbeads were imaged as shown in Figure 4-25. Figure 4-25(a) shows the beads imaged using a bench-top TPEF system, while Figure 4-25(b) is the TPEF image acquired using the 2-D LVD micromirror. This figure has a field of view of 50 μm , and a lateral resolution of 1.5 μm .

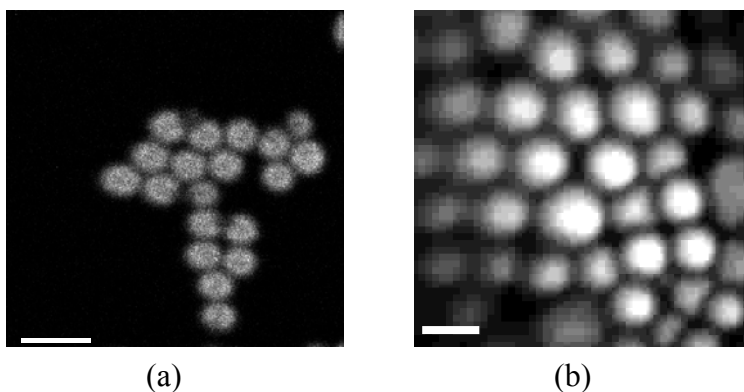


Figure 4-25: TPEF imaging of 10- μm diameter fluorescent microbeads. (a) Bench-top TPEF imaging system. (b) MEMS-based TPEF imaging. Imaged by L. Fu. Used with permission.

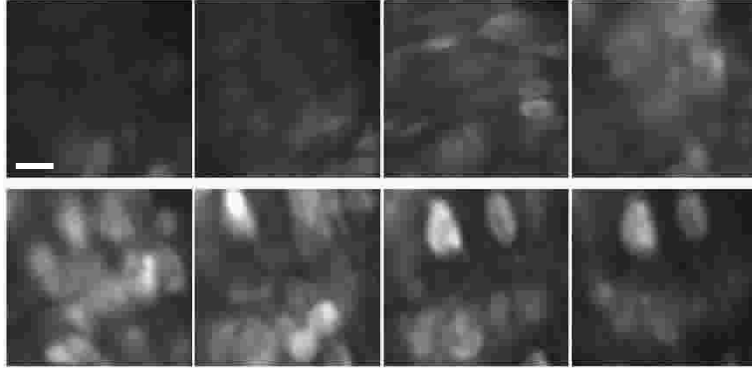


Figure 4-26: *In vitro* imaging of rat stomach epithelial surface stained with 1% acridine orange in Ringer's solution. Scale bar represents 10 μm , and image spacing is 10 μm . Imaged by L. Fu. Used with permission.

There are a number of promising clinical applications for this nonlinear optical endoscope, but its applications in the areas of the gastrointestinal tract and the oral cavity have been highlighted as shown in Figure 4-26. This figure shows the *in vitro* TPEF imaging of rat stomach epithelial surface (stained with 1% acridine orange in Ringer's solution) at different penetration depths. The field of view of these images is 50 by 50 μm^2 , and the lateral imaging resolution is 1.5 μm . The columnar mucosal tissue microstructure of the rat stomach is clearly visible.

These results demonstrate the potential of MEMS-based endoscopic TPEF and SHG imaging systems for the early detection and staging of gastrointestinal cancers. Also, as a wide variety of inner organs (e.g., cervix, colon) can be accessed and imaged by similar endoscopic nonlinear optical imaging systems, the results suggest the potential applications of this technique for noninvasive or minimally invasive imaging diagnosis in these tissues.

4.5 Summary

This chapter presented a novel LVD microactuator design along with experimental verification. This actuator design used a complementary configuration of two actuators

for making micromirrors that are capable of high-speed vertical scanning as well as 1-D bi-directional rotational scanning. A maximum vertical displacement of 200 μm has been achieved with a microdevice of only 0.32mm by 0.7mm in size. Much larger vertical displacements in the millimeter-range can be achieved by simply increasing the length and/or the initial tilt angle of the frame. This 1-D mirror also scanned optical angles greater than 170° at resonance. A 2-D LVD micromirror was also successfully demonstrated to be able to scan optical angles larger than $\pm 30^\circ$ at driving voltages less than 12 V. 2-D dynamic scanning using this device was demonstrated by obtaining a 14° by 50° angular raster scan pattern. Nonlinear optical endoscopy using these micromirrors has been demonstrated, and imaging resolution as high as 1.5 μm has been achieved. This result validates the potential of using these scanners for *in vivo* detection of precancers.

CHAPTER 5 MICROLENS SCANNERS AND OPTICAL CONFOCAL MICROSCOPY

This chapter presents a novel microlens scanner design that can displace its focal point up to a few millimeters. This electrothermally-actuated microlens scanner uses the large-vertical-displacement (LVD) microactuator design, which was introduced in Chapter 4, to generate large out-of-plane displacements at low actuation voltages.

5.1 LVD Microlens Scanner

The electrothermal scanning micromirrors presented in Chapters 3 and 4 cannot be used for ultrahigh-resolution OCT imaging since their transverse resolution was limited by the required depth-of-focus of the optical beam. This is due to the fact that the transverse resolution (spot size of the focused beam) is inversely proportional to numerical aperture (NA), while the depth-of-focus is inversely proportional to the square of NA.

However, in order to obtain high transverse resolution without compromising the axial scanning range and small size requirement of endoscopic OCT/OCM systems, a MEMS microlens can be used to scan along the optical axis. Various microlens scanner designs have been reported in literature. Hoshino and Shimoyama developed a pneumatically-actuated microlens arrays that demonstrated a maximum vertical displacement of 11 μm [144]. Kim *et al.* demonstrated an electrostatically-actuated microlens scanner with a maximum displacement of 7 μm for optical data storage applications [145]. Kwon *et al.* presented a microlens scanner for confocal imaging that

used electrostatic vertical-comb-drives to produce a maximum displacement of 55 μm at resonance [62]. These abovementioned scanners generate vertical displacements only up to a few tens of microns, but OCM imaging typically requires an axial scanning depth of at least a millimeter.

Another method by which the focal point of the microlens can be scanned axially is by varying the focal length of a tunable lens. Graham developed a variable focus lens using a deformable chamber filled with liquids with different refractive indices [146]. Sugiura and Morita also demonstrated a variable-focus, liquid-filled, 27-mm diameter lens that varied its focus by changing the liquid volume in the lens [147]. Berge and Peseux demonstrated a 6-mm diameter, variable lens formed at the interface between two immiscible liquids [148]. By using the principle of electrowetting [149] the contact angle of one of the liquids was changed, thereby changing the focal length of the lens. However, this lens requires a high dc voltage of 210 V in order to double its focal length. Krupenkin *et al.* also used electrowetting to change the curvature of a liquid microlens to vary its focal length [150]. They reported a 0.5 mm increase in focal length at an applied voltage of 80 V. Although these tunable lenses meet the millimeter-range scanning requirement of OCM systems, their bulky-size and/or high operating voltages are a deterring factor in their use for endoscopic imaging applications. Also, liquid lenses may not be suitable for OCM imaging since infrared light may be absorbed by the lenses.

In this section a novel microlens scanner design is presented which can displace its focal point up to a few millimeters. A miniature MEMS scanner that can displace its focal point by up to 280 μm has been fabricated and tested to demonstrate the proof-of-concept

of this scanner design. This microlens scanner design can be easily scaled to meet the 2-mm axial scanning requirement of OCM systems.

5.1.1 Microlens Scanner Design

The schematic of the LVD microlens scanner is illustrated in Figure 5-1. The lens holder consists of a square plate with a circular opening in the middle. A polymer microlens is formed on top of this plate. The lens holder is attached to a rigid silicon frame by a set of aluminum/silicon-dioxide bimorph actuation beams. Since these beams actuate the lens holder plate, they are collectively referred as the *lens actuator*. A 30-50 μm thick single-crystal-silicon (SCS) layer under the lens holder prevents curling of the thin-film layers of the plate. The rigid silicon frame is attached to the substrate by another set of identical bimorph actuation beams, referred to as the *frame actuator*. The lens and frame actuators together form one set of the LVD microactuator, in which the out-of-plane curls of the two sets of bimorph beams compensate each other. Therefore, the lens holder and the lens are parallel to the substrate surface. Polysilicon resistors embedded in the bimorph beams provide heating for electrothermal actuation. As shown in Figure 5-1(b), the initial elevation of the lens holder above the substrate surface is given by: $H = L_f \sin \theta$, where L_f and θ are the length and initial tilt angle of the frame, respectively. Equal angular rotations by the two actuators will result in pure vertical displacement of the microlens. Large z-axis displacement can be achieved via the angular amplification due to the long arm length of the frame.

5.1.2 Fabricated Microlens Scanner

As a proof of concept, a miniature version of the millimeter-range microlens scanner was fabricated [151, 152]. A fabricated lens holder shown in Figure 5-2(a) is

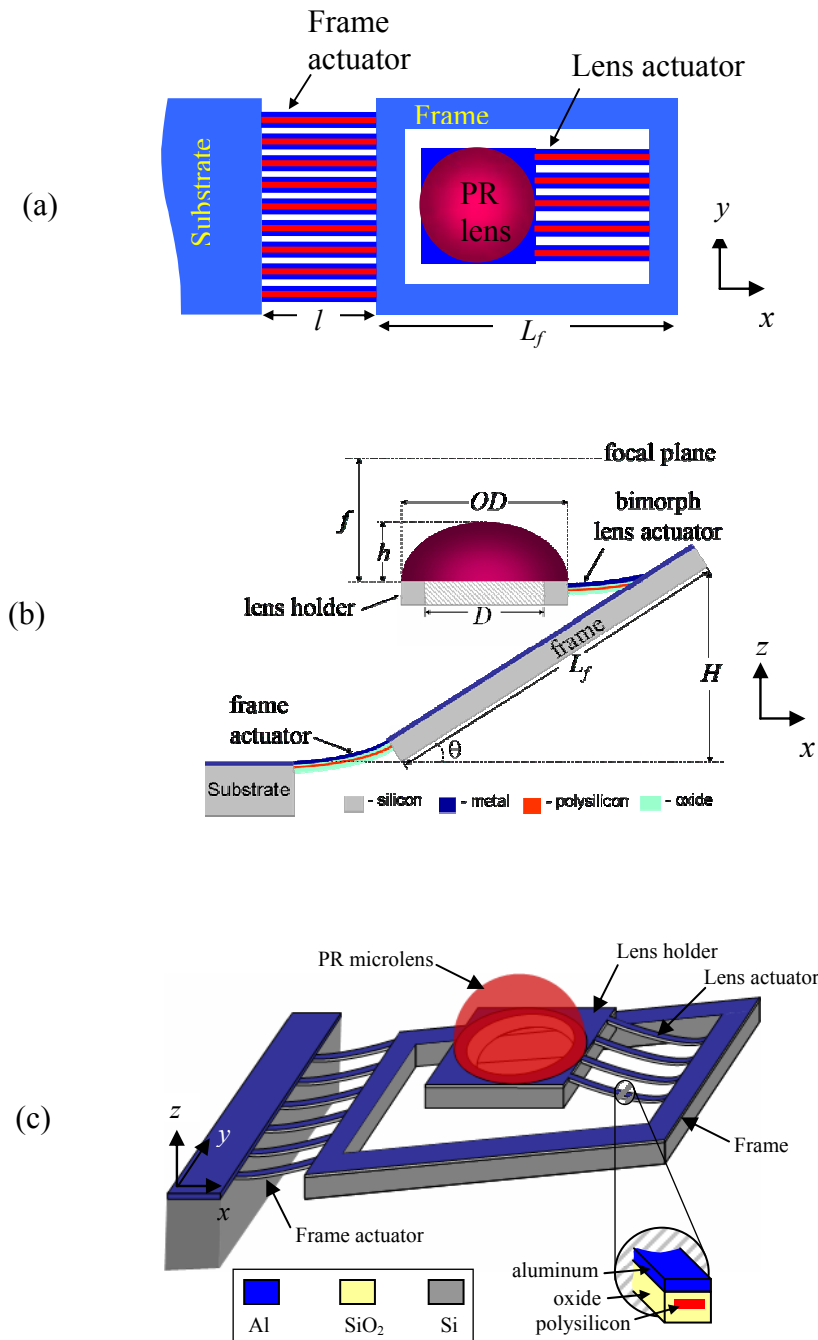


Figure 5-1: Design schematic of the LVD microlens scanner. (a) Top view. (b) Cross-sectional side view. (c) 3-D illustration of the scanner.

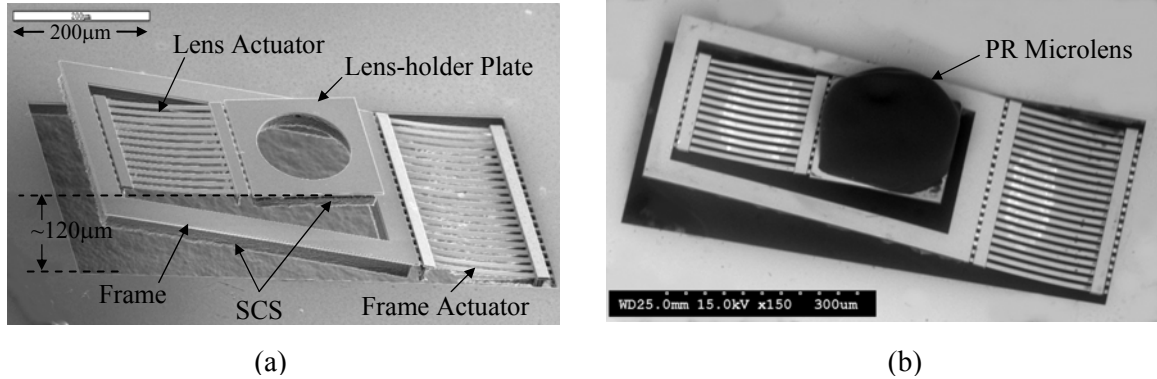


Figure 5-2: SEMs of: (a) Fabricated LVD lens holder, and (b) LVD microlens scanner. only 0.7 mm by 0.32 mm in size. The lens holder plate is 200 μm by 200 μm in size, and it has a circular opening with a diameter of 140 μm , on which a photoresist (PR) microlens is formed. The initial rest position of the lens holder is 120 μm above the substrate surface. This LVD lens holder was fabricated using the same DRIE CMOS-MEMS process presented in Section 3.3, and its processing steps are illustrated in Figure 5-3. After the four DRIE CMOS-MEMS dry etch steps, a fifth step has been added that integrates a polymer microlens with the device. In this final processing step, a droplet of Shipley Microposit 1805 photoresist (PR) is dispensed using a nano-injection system and then baked in an oven (120°C for 30 minutes) to form a microlens due to surface tension. Since there are no substrate or thin-film layers directly above or below the microlens structure, large vertical actuation range is allowed.

Table 5-1: Microlens characteristics

Measured Parameters	
Lens Diameter	210 \pm 1 μm
Lens Height	58 \pm 2 μm
Focal Length, f	188 \pm 2 μm
Estimated Parameters	
Numerical Aperture,	\sim 0.35
Microlens Volume	\sim 1.1 nL
Radius of Curvature	\sim 124 μm

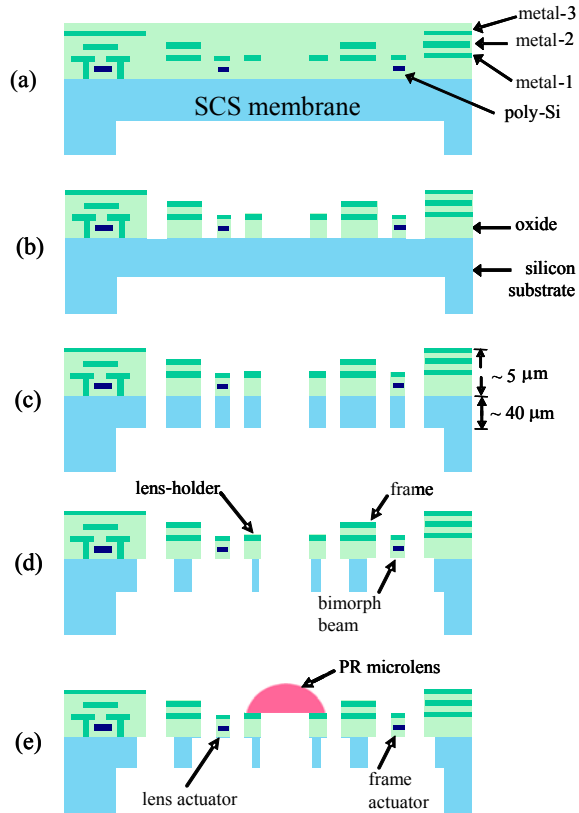


Figure 5-3: Microlens fabrication process. (a) Backside Si etch. (b) Oxide etch. (c) Deep Si trench etch. (d) Si undercut. (e) Microlens formation by reflow of photoresist.

The initial rest position of this fabricated microlens is $120 \pm 2 \mu\text{m}$ above the substrate surface. The weight of the microlens causes less than $1 \mu\text{m}$ vertical displacement of the lens-holder plate. This is attributed to the small volume of the microlens and also due to the large stiffness of the bimorph beams. A fabricated microlens is shown in Figure 5-4. The measured and estimated parameters of the microlens are listed in Table 5-1. Since no curvature was observed on the bottom surface of the microlens within an accuracy of $2 \mu\text{m}$, the estimated parameters were calculated using analysis presented by Daly [153] with the assumption of a flat bottom lens surface. Estimations using the smallest possible value ($\sim 1200 \mu\text{m}$) for the bottom radius-of-curvature increase the focal length by less than 12%. The PR microlens has a diameter of

about 210 μm . Since the circular opening on the lens holder has a smaller diameter of 140 μm , this helps to reduce spherical aberration. The measured focal length of the microlens is about 188 μm . A 0.2 nanoliter variation in the dispensed volume of the PR droplet will change the focal length of the formed microlens to within 10%. Microlenses with longer focal lengths can be fabricated by reducing the volume of the photoresist droplet, or by increasing the size of the lens holder. This fabrication process also allows for the formation of microlenses that are optically transparent for the visible spectrum of light by using UV-curable polymers instead of photoresist.

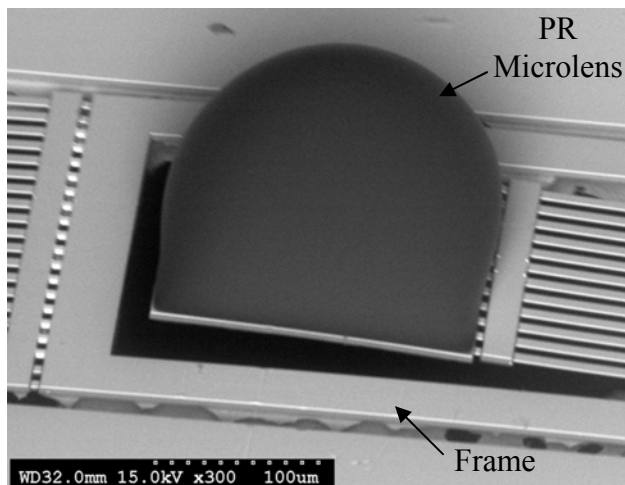


Figure 5-4: SEM of a fabricated PR microlens.

5.1.3 Experimental Results

Vertical displacement of the microlens is accomplished by equal angular rotations of the two actuators. A plot of the vertical displacement of the microlens as a function of the drive voltage of the frame actuator is shown in Figure 5-5(a). A maximum vertical displacement of 280 μm was obtained when a dc voltage of 10V (corresponding to a dc current of 12 mA) was applied. Figure 5-5(b) shows the driving voltage ratios that are needed for the two actuators to generate pure vertical displacement. This plot clearly shows two regions of device operation, which are related to the position of the microlens

with respect to the substrate surface. The voltage ratio increases linearly with displacement until the microlens displaces below the substrate surface, at which point this ratio becomes constant. A voltage divider can be used to drive the lens and frame actuators with a voltage ratio of 1:2.3 after the lens displaces below the substrate surface. The tilting of the microlens is less than 1° during the entire $280\ \mu\text{m}$ vertical scan range.

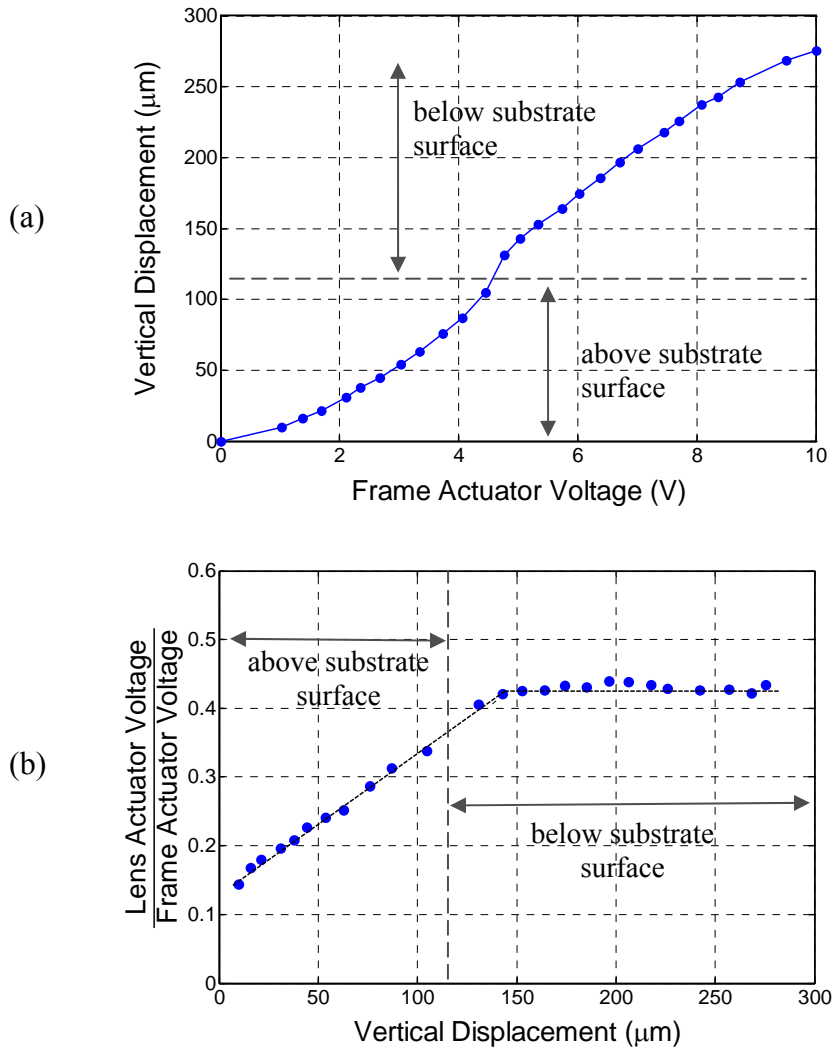


Figure 5-5: Vertical displacement experiment. (a) Vertical displacement of the microlens as a function of frame actuator voltage. (b) Plot of the ratio of the applied voltages to the lens and frame actuators that was used to obtain the vertical displacement shown in (a).

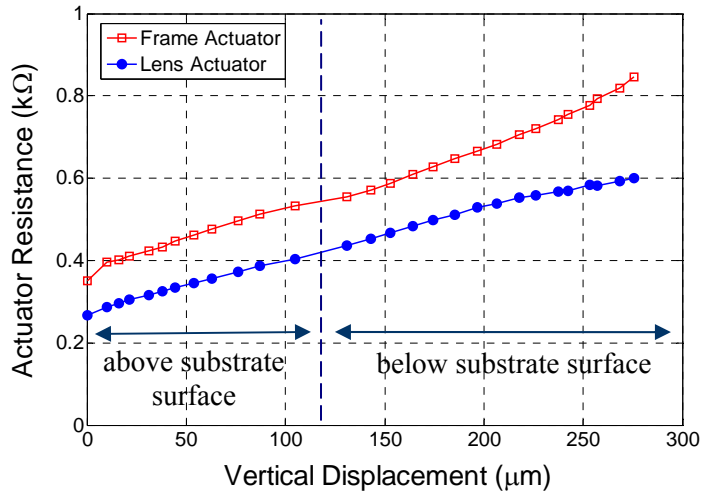


Figure 5-6: Plot showing the increase in polysilicon heater resistances versus vertical displacement for the two actuators.

Since the focal length is smaller than the thickness of the substrate, the incident light beam must enter from the substrate side. Longer focal lengths are possible by reducing the volume of the PR droplet, but at the expense of reduced NA. For example, a 0.3 nanoliter droplet will form a 0.5 mm focal length microlens, but with a reduced NA of 0.14. A longer focal length gives the microlens a larger working distance.

The open circuit polysilicon resistances of the lens and frame actuators are 240Ω and 360Ω , respectively. The electrical resistance of the polysilicon heaters embedded inside the bimorph beams increases with an increase in applied voltage due to Joule heating. A linear correlation between the vertical displacement of the microlens and the polysilicon resistance of the two actuators was observed, as shown in Figure 5-6. This correlation allows for closed-loop control of the vertical position of the microlens by monitoring the resistance change of each individual polysilicon heater. Although researchers have reported significant variations in focal length of polymer lenses with increasing temperature [154], no noticeable change in focal length was observed (within

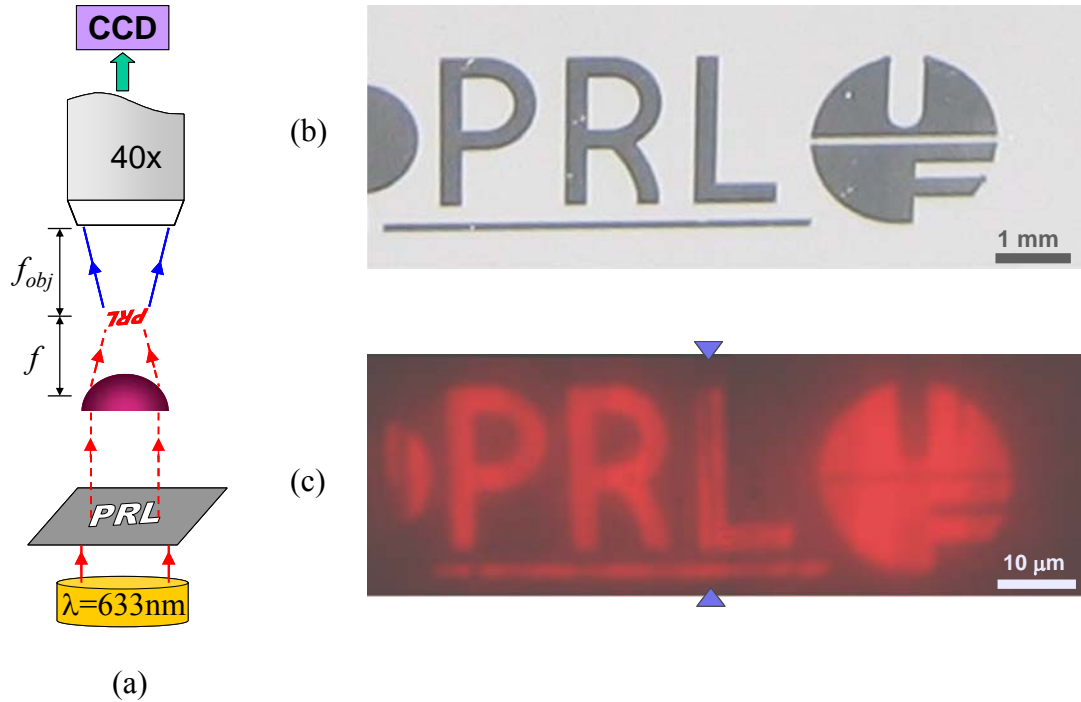


Figure 5-7: Microlens imaging quality. (a) Schematic of the imaging experiment apparatus. (b) Photo of the test pattern. (c) Snap-shot images of the test pattern as obtained through the PR microlens. The triangular markers indicate the location where two images were merged to obtain the complete test pattern.

2 μm) during the actuation range of this device. The LVD actuators exhibited no failure or performance degradation after being scanned at their full actuation range for over 7 billion cycles. The resonant frequencies of the lens and frame actuator structures are 2.15 kHz and 1.1 kHz, respectively.

The imaging quality of the PR microlens was tested using an experimental setup comprising of a microscope, CCD (charge coupled device) camera, chrome photomask and a light source, as shown in Figure 5-7(a). A test pattern on the mask (placed 100 mm below the microlens) was imaged by the microlens. The test-pattern was demagnified by about 100 times, and its image was formed at the focal plane of the microlens as shown in Figure 5-7(a). This image was then captured by the CCD camera installed on the microscope using a 40 \times objective. Figure 5-7(b) shows the pictures of the test pattern,

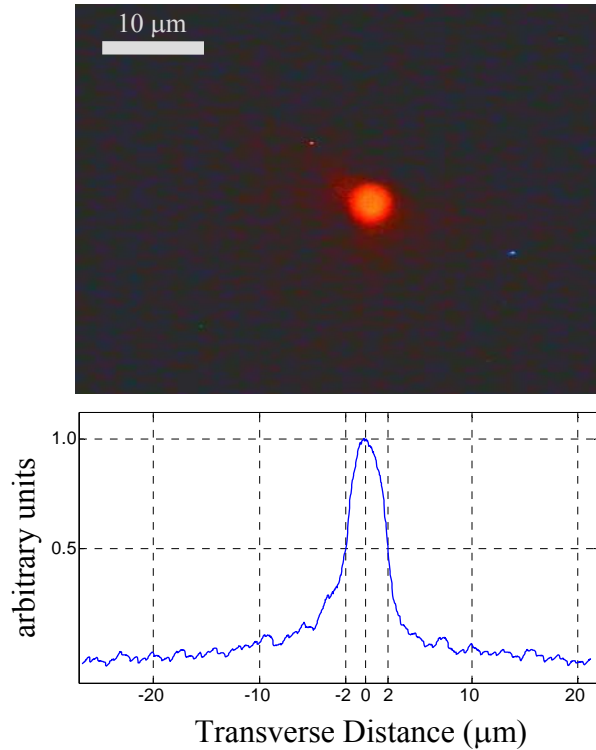


Figure 5-8: CCD image of a 4 μm focused beam spot (top), and its corresponding intensity profile (bottom).

and Figure 5-7(c) shows the photographs of the images captured using the microlens. The field of view of the captured photos is 40 μm by 30 μm , and features smaller than 2 μm can be easily distinguished. The measured spot size when imaging a pinhole is less than 2 μm using a 633 nm collimated light source, which is close to the theoretical resolution ($\sim 1.1 \mu\text{m}$) of this microlens. A CCD image and its intensity profile of a 4 μm sized spot are shown in Figure 5-8.

5.2 Millimeter-Range LVD Microlens Scanner

The LVD microlens scanner presented in Section 5.1 was fabricated to validate the concept of using a LVD microactuator to vertically displace an integrated microlens. As mentioned in Section 2.2, OCM requires vertical displacement of the focused beam-spot by 0.5 mm to 2 mm; therefore the LVD scanner design was scaled to meet this requirement.

The larger version of this scanner (referred to as the mm-LVD microlens device) was fabricated using the AMI 0.5- μm 3-metal CMOS process.

5.2.1 Millimeter-Range Scanner Design

A schematic of the mm-LVD microlens device is shown in Figure 5-9. In order to amplify the vertical displacements generated by the LVD microactuator, the frame length (L_f) was increased to 1.6 mm. The initial tilt angle provided by a 200- μm long bimorph actuator that is fabricated using the AMI 0.5- μm process is $\sim 40^\circ$. This initial tilt angle along with the increased frame length will increase the initial elevation of the microlens holder to an estimated value of about 1 mm. The diameter (D) of the circular opening on the lens holder has been increased to 600 μm , and a transparent silicon dioxide mesh structure has been added in this opening. This oxide mesh was added to prevent the photoresist droplet from falling through the large opening during the microlens formation step of the fabrication process. The fabrication process has been slightly modified to allow for the formation of this oxide mesh.

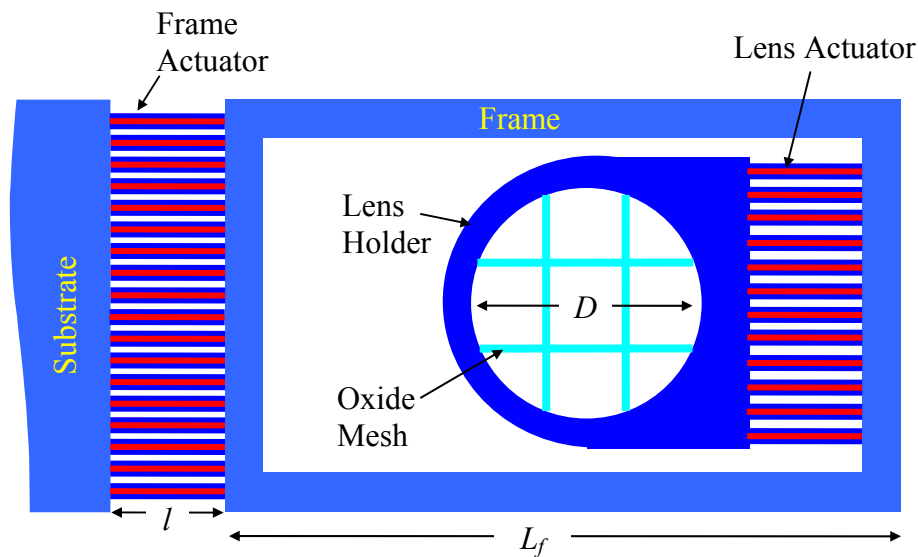


Figure 5-9: Top view of the millimeter-range LVD microlens scanner.

5.2.2 Fabrication Process

The modified wafer-level fabrication process is shown in Figure 5-10. The first step is the backside silicon etch that defines the thickness of the SCS membrane. The next step is the frontside oxide etch which uses the metal layers as an etching mask. After the oxide etch, photoresist is spun on the device as shown in Figure 5-10(c). The photoresist is then etched uniformly across the entire device until the metal-2 and metal-3 layers are completely exposed. This is shown in Figure 5-10(d), where the metal-1 layer is still protected by photoresist. Next, a wet metal etch is done to remove the exposed metal layers. After this, the remaining photoresist is removed using an oxygen plasma clean

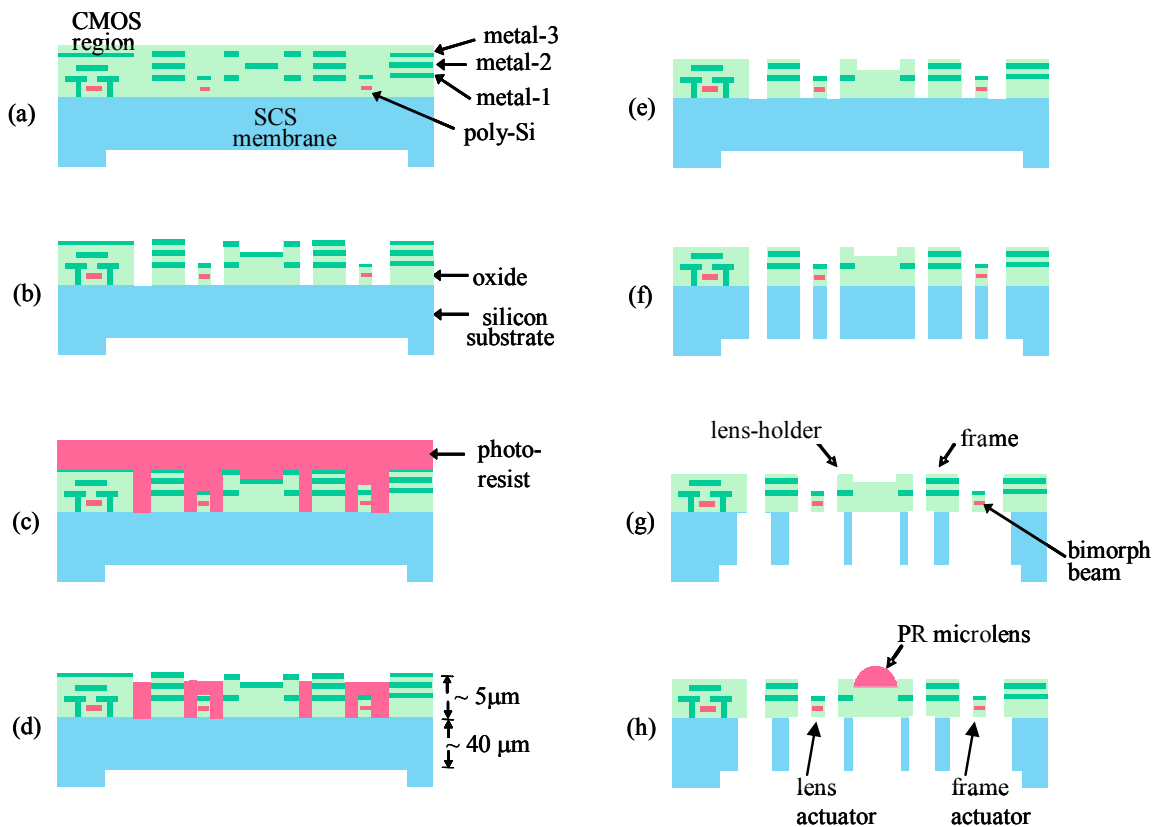


Figure 5-10: Modified fabrication process for mm-LVD microlens scanner. (a) Backside Si etch. (b) Oxide etch. (c) Spin on photoresist. (d) Anisotropic photoresist etch to expose metal-2 layer. (e) Metal wet etch followed by photoresist removal. (f) Deep Si trench etch. (g) Silicon undercut. (h) Microlens formation by reflow of photoresist.

process to obtain the device as shown in Figure 5-10(e). The next 3 steps are exactly the same as before, in which a silicon trench etch is performed followed by a silicon undercut to release the device. The last step involves formation of the microlens by precisely dispensing photoresist onto the oxide mesh of the lens holder.

It is challenging to fabricate millimeter sized CMOS dies using this wafer-level fabrication process because spinning on a planar layer of photoresist is difficult. Therefore, a modified process was used to fabricate on the die level that used one simple lithography step. The die-level fabrication process is illustrated in Figure 5-11. The first few steps are the same, but after spinning on a layer of positive photoresist (which is not required to be planar), a photomask with an 800- μm circular opening is used (Figure 5-11(c)). This circular opening is aligned to the lens holder within a lateral tolerance of about 20 μm . After the metal layers on the mesh and the lens-holder area are exposed, aluminum wet-etchant is used (Figure 5-11(d)). The other steps are exactly the same as before. Figure 5-12 shows the photograph of a device after the lithographic and

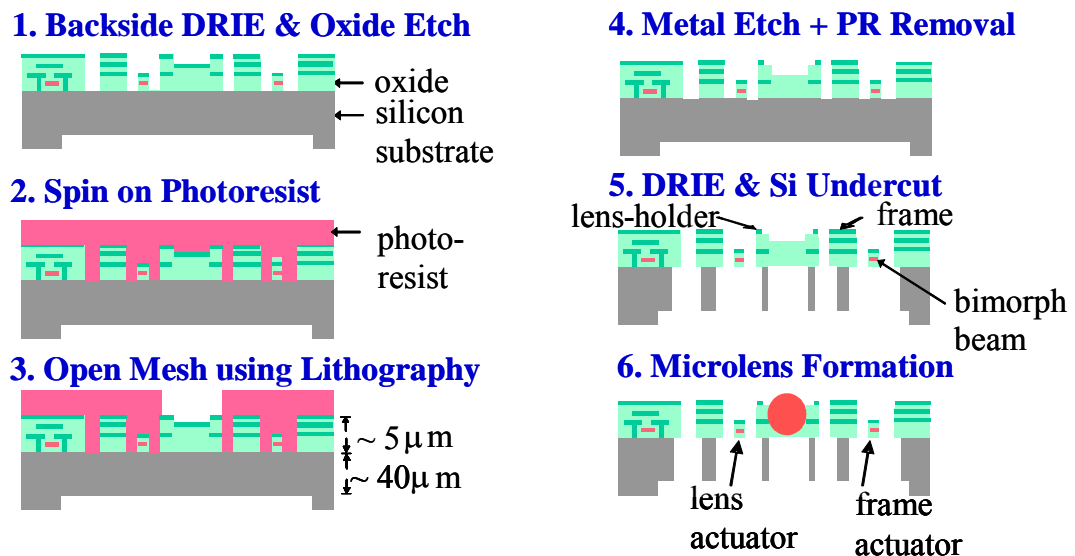


Figure 5-11: Modified process for die-level fabrication of the microlens scanner.

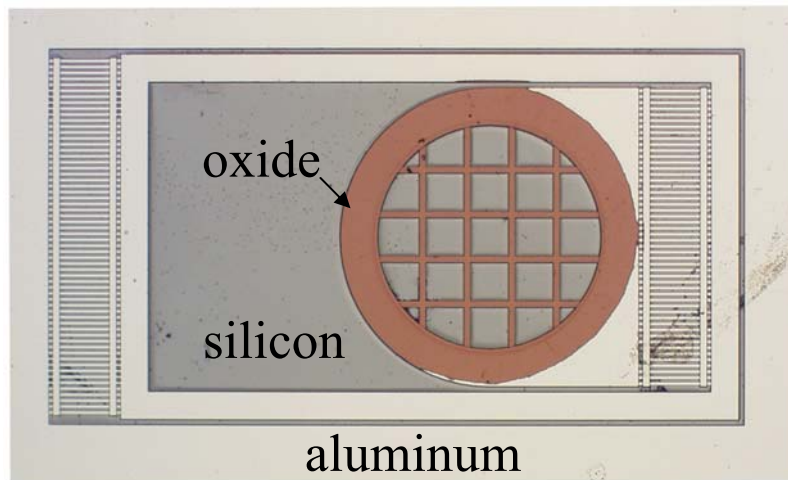


Figure 5-12: Photograph of the CMOS die after the wet etch of lithographically exposed aluminum layers.

aluminum wet-etch steps.

The process modifications allow the use of the metal-2 layer to define the structure for the 3- μm thick oxide mesh within the lens holder. Also, the PR microlens is now formed on a layer of insulating oxide instead of a more thermally-conductive Al metal layer, resulting in better thermal isolation from the electrically-heated lens-actuator. Thermally isolating PR microlenses from heating sources prevents the situations observed by Glebov *et al.* [154], where the focal length of a polymer microlens changed significantly with increasing heat. Thermal isolation also prevents carbonization of the PR microlens, which tends to occur at temperatures greater than 200°C.

The initial rest position of a fabricated microlens [155] is 1.2 mm above the substrate surface, as shown in Figure 5-13. In order to form a polymer microlens on the elevated lens-holder, droplets of PR are first dispensed using a nanoliter-injection system and then baked in an oven to form a microlens due to surface tension. Figure 5-14 shows a fabricated microlens scanner integrated with a photoresist microlens.

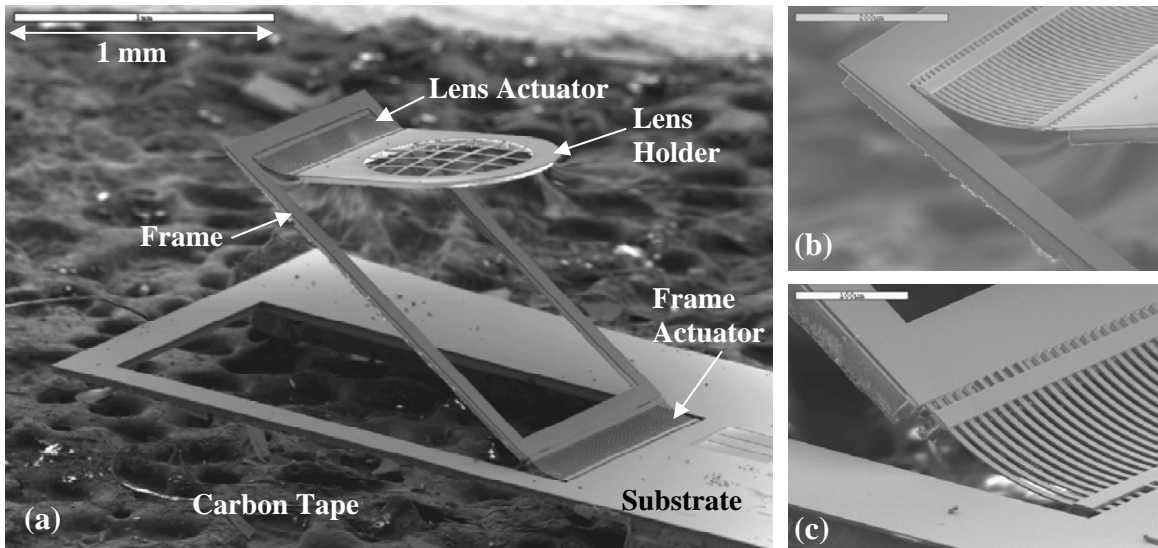


Figure 5-13: (a) SEM of a fabricated scanner before microlens formation. Close-up views of (b) lens actuator; and (c) frame actuator bimorph regions.

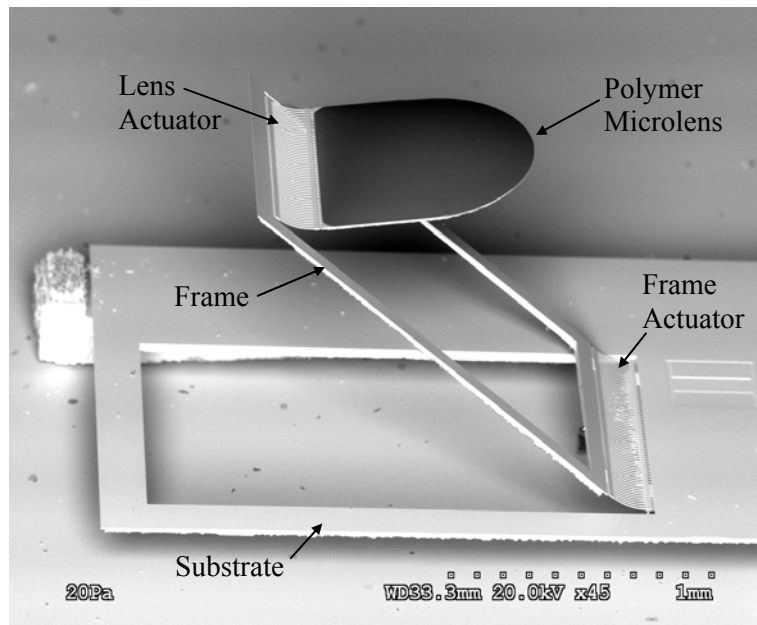


Figure 5-14: SEM of a fabricated microlens scanner with integrated polymer microlens.

Focal length can be controlled by varying the quantity and/or volume of the dispensed dropets. PR microlenses with focal lengths between 0.5 to 3 mm with numerical apertures (NA) ranging from 0.1 to 0.35 have been successfully fabricated.

Figure 5-15 shows two fabricated PR microlenses with different focal lengths and lens

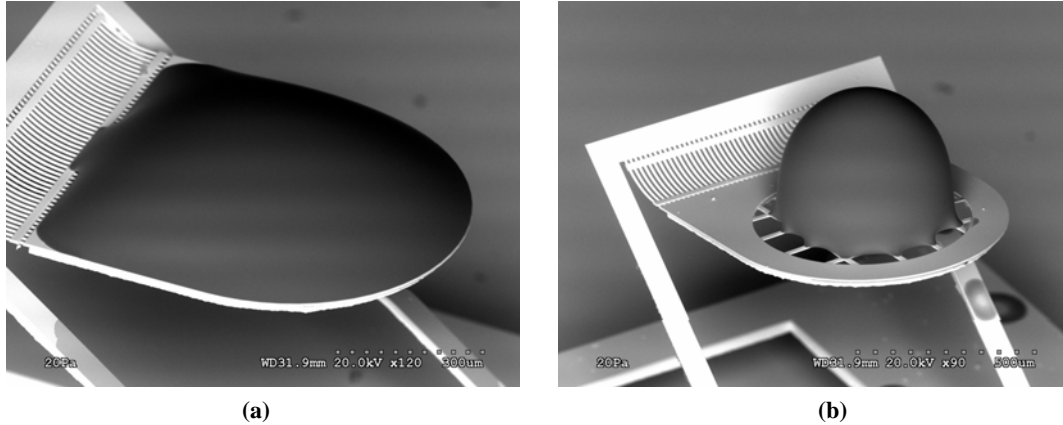


Figure 5-15: SEMs of (a) convex microlens, and (b) ball-type microlens.

sizes. The convex microlens has a focal length of 3 mm, 0.1 NA and a lens diameter of 0.8 mm. The ball-type microlens of Figure 5-15(b), has a focal length ~ 0.5 mm, 0.35 NA, and a diameter of ~ 0.4 mm.

To test the imaging quality of these microlenses, a chrome test mask was placed ~ 100 mm away from the ball-type microlens, and the image at its focal plane (which is de-magnified by about $100\times$) was captured using a CCD microscope camera. The test pattern image obtained by a PR microlens with a numerical aperture of 0.35 is shown in Figure 5-16, where features as small as $1\ \mu\text{m}$ can be resolved.

Table 5-2 provides a theoretical estimate of the optical properties of the microlens for different desired focal length values. The focal length of the microlens in conjunction with the package design determines the working distance between the scanner and *in vivo* tissue. As seen in Table 5-2, a longer focal length (i.e., a longer working distance) reduces the lateral imaging resolution which in turn is determined by the focused spot size. A slight variation in the volume of the dispensed photoresist droplet will change the focal length significantly; therefore a more precise photoresist dispensing technique is required for good repeatability. A commercially available inkjet dispensing system which dispenses droplets

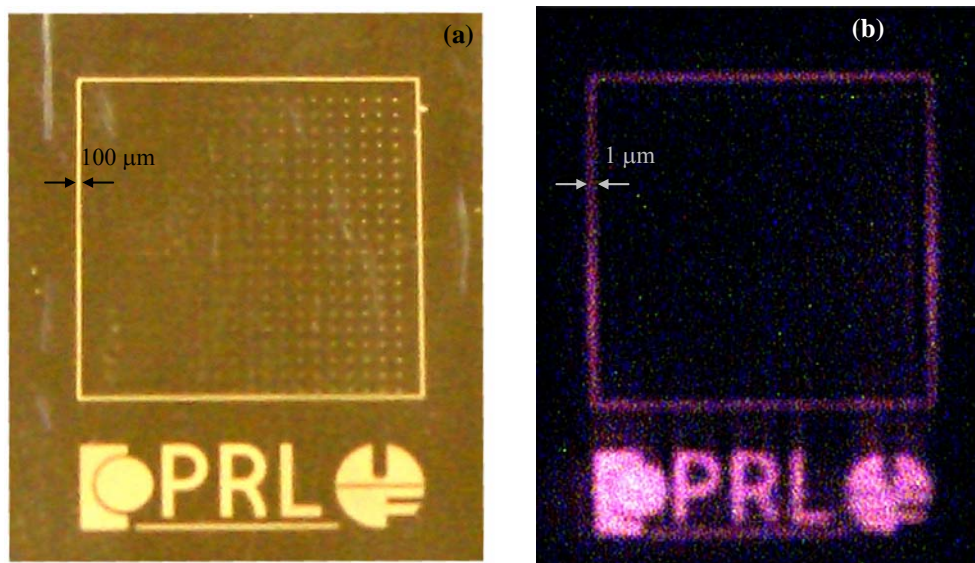


Figure 5-16: Imaging using the photoresist microlens. (a) Photograph of the test pattern on a chrome mask. (b) Corresponding image of the test pattern as seen at the focal plane of the photoresist microlens.

Table 5-2: Estimated microlens parameters for various desired focal lengths.

Targeted Focal Length (mm)	Focused Spot Size (μm)	Depth of Focus (μm)	Numerical Aperture (NA)	Required Photoresist Volume (nL)
1.0	2.8	9.3	0.29	10.6
1.5	4.2	20.8	0.20	6.7
2.0	5.6	37.1	0.15	5.0
2.5	6.9	57.9	0.12	4.0
3.0	8.3	83.4	0.10	3.3

These values were computed for a microlens diameter of 600 μm, and light wavelength of 1310 nm.

with an accuracy of few tens of picoliters may be used.

5.2.3 Experimental Results

Vertical displacement of the PR microlens was achieved by simultaneously exciting both actuators and tuning the actuation voltages such that the opposite angular rotations of the two actuators offset any net tilting of the microlens. The static displacements of the microlens and its corresponding driving voltage plots are shown in

Figure 5-17, where the vertical displacements of the microlens were observed to within an accuracy of $\pm 2 \mu\text{m}$ by using a $40\times$ objective lens (0.65 NA).

Figure 5-17(a) shows that a maximum vertical displacement of 0.71 mm was obtained at a dc voltage of 23 V applied to the frame actuator. Figure 5-17(b) displays the same vertical displacement data, but with respect to the electrical power supplied to the two actuators. The plot of the two driving voltages that are required to obtain this vertical displacement is shown in Figure 5-17(c). The slope of this linear plot yields the driving voltage ratio for the two actuators for LVD actuation. The driving voltage applied to the lens actuator is 43% of the frame actuator voltage, which is provided by a voltage divider. Using this constant voltage ratio, the maximum tilt of the microlens in the entire 0.71mm travel range is less than 0.4° .

The resistances of the polysilicon heaters embedded in both actuators increase significantly with applied voltage due to Joule heating. Joule heating raises the temperature of the bimorphs, which in turn increases the heater resistances due to the thermal coefficient of resistivity of polysilicon. The open-circuit, room-temperature electrical resistances of the lens and frame actuators are 1.17 k Ω and 1.35 k Ω , respectively. A linear correlation between the vertical displacement of the microlens and the heater resistance of the two actuators was observed, as shown in Figure 5-18. This experimentally determined linear relationship between the resistors allows for closed-loop feedback control of the vertical position of the microlens by monitoring the polysilicon resistance change of each actuator.

The initial elevations of the microlens at different operating temperatures were also documented, and the results are presented in Figure 5-19. The initial lens-holder elevation

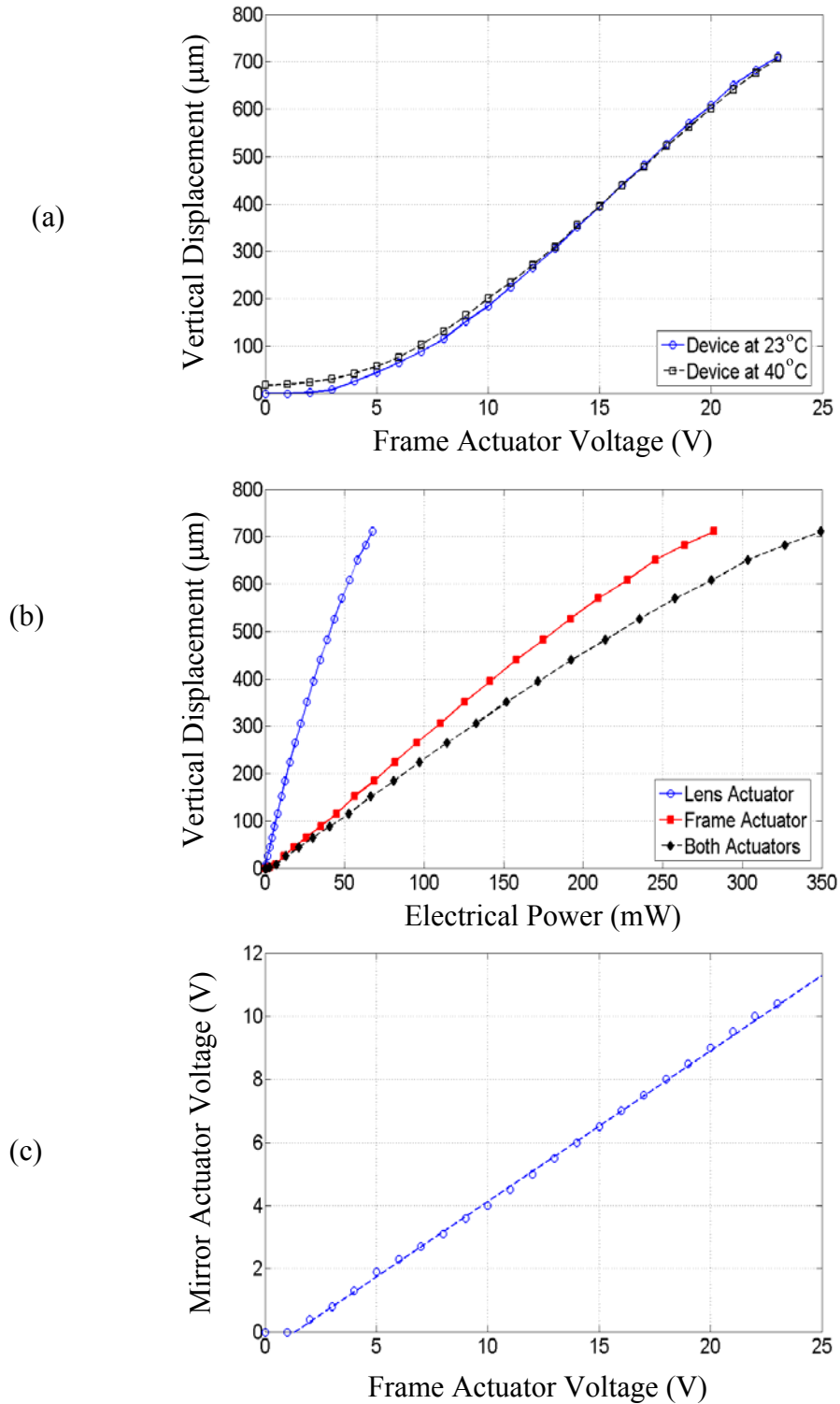


Figure 5-17: Vertical displacement of the microlens scanner. (a) Microlens displacement as a function of frame actuator voltage. (b) Displacement versus applied electrical power. (c) Corresponding linear relationship between the two voltages.

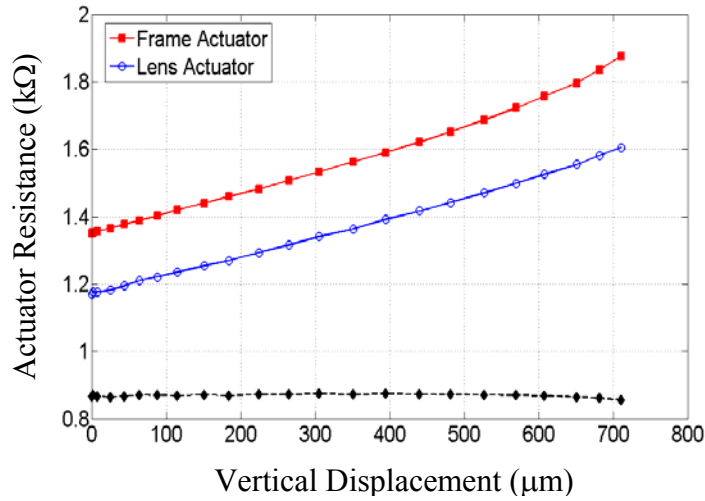


Figure 5-18: Change in resistance versus vertical displacement of the microlens. of a fabricated microlens is 1.2 mm at a room temperature (23°C), and it decreases with increasing temperature. Since this device will be packaged inside an endoscope for *in vivo* OCM imaging, the maximum ambient temperature shall not exceed 40°C. Therefore, the vertical scan range of the device will, in the worst case, be reduced by up to 20 μm, which is less than 3% of the entire scan range. This can be seen in the plots of Figure 5-

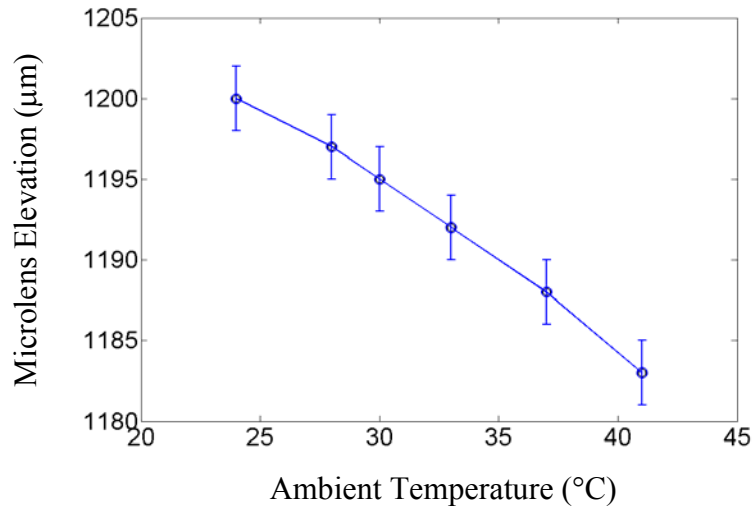


Figure 5-19: Change of initial microlens elevation with ambient temperature.

17(a) where an increase in ambient temperature to 40°C reduced the vertical scan range by $\sim 17 \mu\text{m}$.

There is significant lateral shifting of the microlens during vertical actuation, as shown in Figure 5-20. A maximum lateral shift of $425 \mu\text{m}$ is observed for the entire vertical scan range. This lateral shift is mainly due to the rotational displacement of the

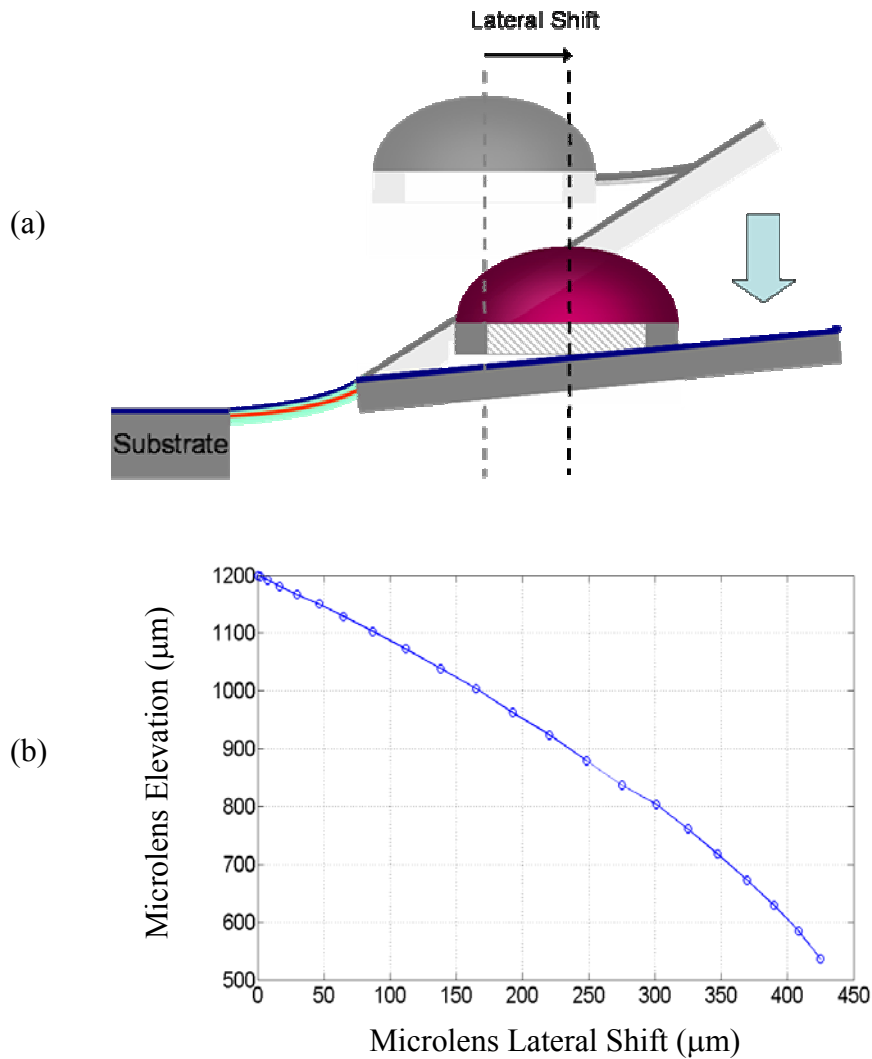


Figure 5-20: Lateral shift of the microlens during vertical displacement actuation. (a) Illustration of the lateral shift. (b) Characterized plot of the lateral shift.

frame actuator, and is amplified by the long length of the silicon frame. This lateral shift will be accounted for and corrected during the OCM image formation stage.

The dynamic response of the device was characterized using the laser Doppler vibrometer. Figure 5-21(a) shows the measured velocity response of the device when a pulse excitation was applied to both actuators at time, $t = 0$. The settling time of this

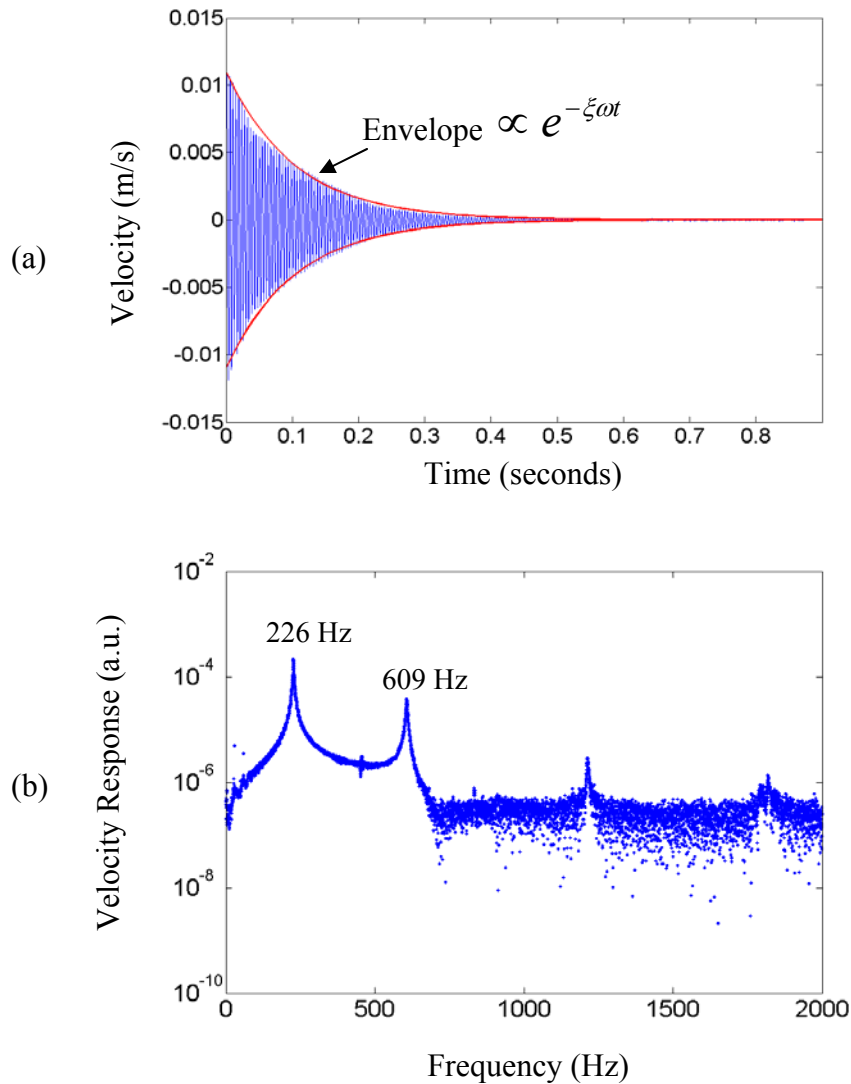


Figure 5-21: Dynamic response of the microlens scanner. (a) Mechanical response when a square excitation was applied to both actuators at $t = 0$. This can be fitted to an exponential envelope using the damping ratio, ξ . (b) Frequency response showing the resonant peaks.

device is around 300 ms, and the quality factor was determined from the envelope by fitting an exponential plot. The Q-factor for this device has been measured to be around 65 to 75. This plot provides the settling time of the device after being subjected to environmental shock and vibrations. Figure 5-21(b) is the frequency response of the device measured using the same laser Doppler vibrometer. Resonant peaks were observed at 226 Hz and 609 Hz, for the frame and lens actuators, respectively.

5.3 LVD Microlens Packaging

To package this microlens scanner into a 5-mm diameter endoscope, a custom holder was fabricated by TMR Engineering, Micanopy, FL. A schematic of this package design is shown in Figure 5-22(a). The LVD microlens scanner was glued on to this hollow cylindrical plastic package. Three copper contacts are available for wire-bonding the microlens to the electrical feed-through wires. The center of the package is machined

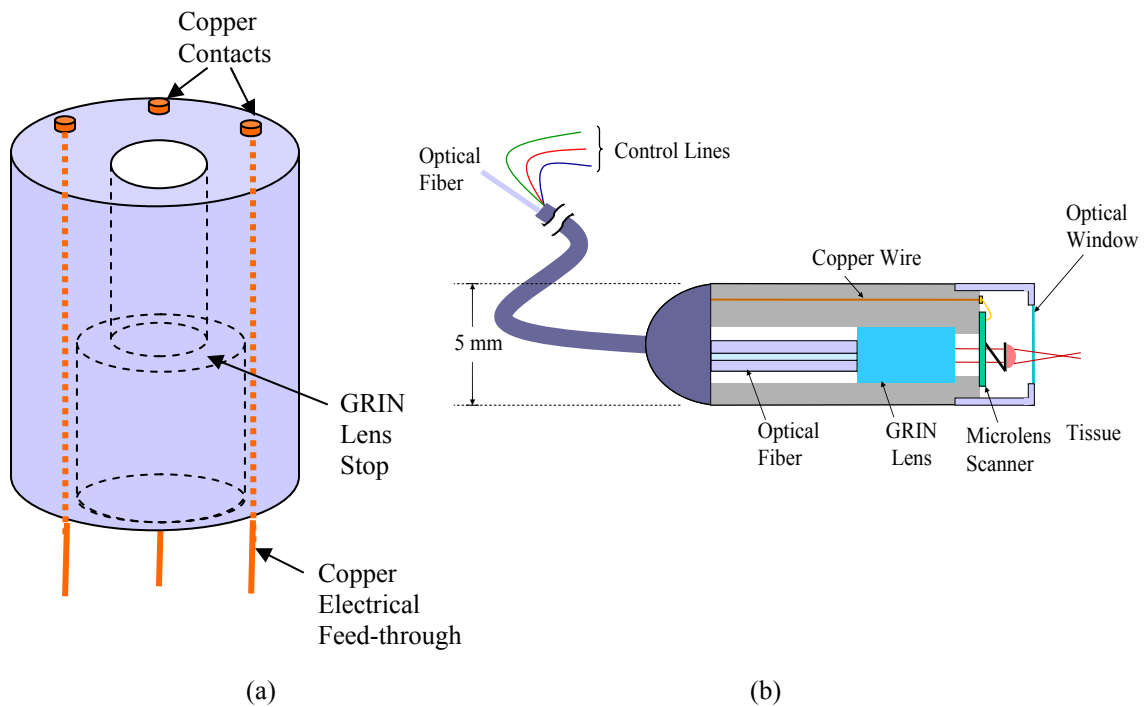


Figure 5-22: Microlens package design. (a) Microlens package schematic. (b) Forward-imaging OCM endoscope.

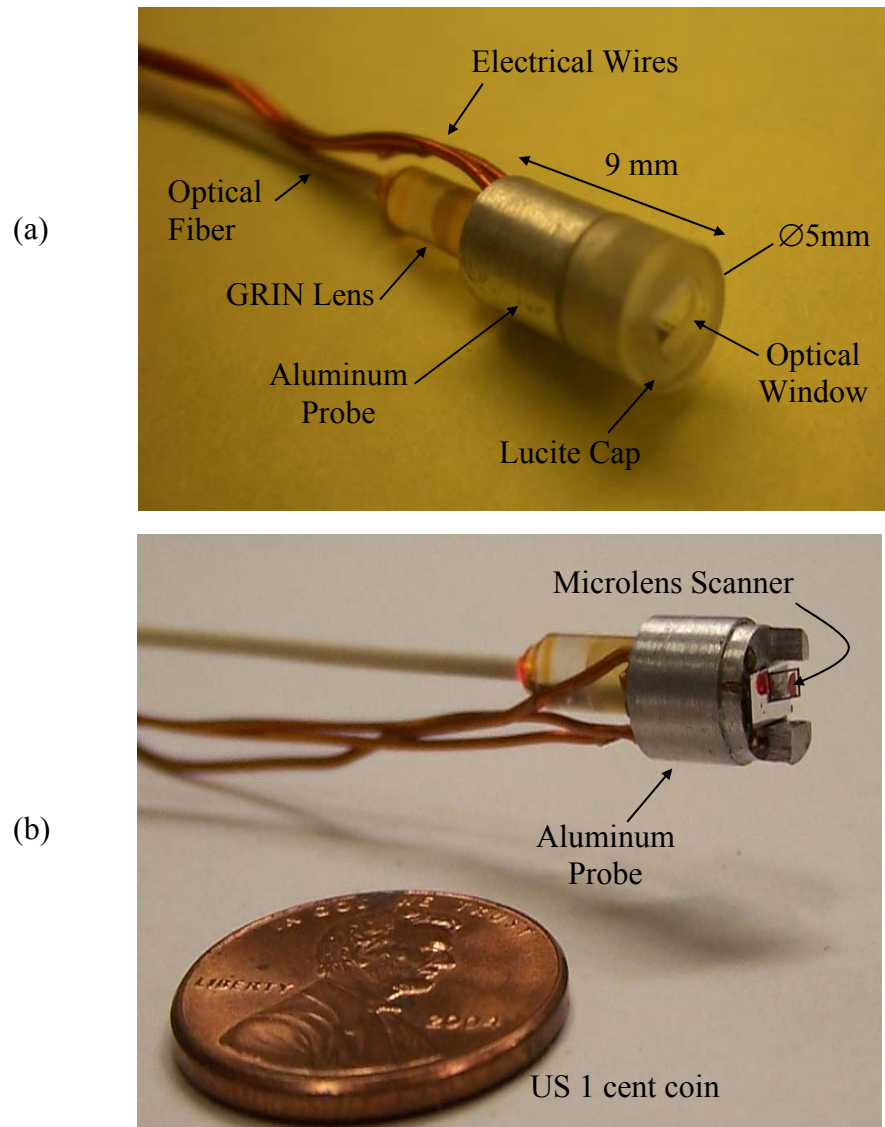


Figure 5-23: Packaged OCM endoscope. (a) With the Lucite end cap. (b) Without the end cap to show the packaged microlens scanner. .

to provide automatic alignment between the collimating lens and the microlens, and also to provide a stop-barrier for the collimating lens. A packaged microlens scanner is then inserted into a forward-imaging endoscope, as shown in Figure 5-22(b).

The packaged OCM endoscope of Figure 5-23 is about 15 mm long, and has a diameter of 5 mm. Figure 5-23(b) shows the inside of the endoscope by removing the

distal Lucite end cap. This Lucite cap has a rectangular optical window that allows the focused light beam to exit this forward imaging endoscope.

5.4 Summary

This chapter presented a tunable microlens scanner which used an LVD microactuator to vertically displace a photoresist microlens by up to 280 μm at a low actuation voltage of 10 V. The CMOS-compatible fabrication process also allows for the formation of optically transparent microlenses by microdispensing ultraviolet-curable polymers instead of photoresist. Microlenses with longer focal lengths can be fabricated by reducing the volume of the dispensed droplet, or by increasing the size of the lens-holder. In order to increase the vertical scanning range of this device, a millimeter-range LVD microlens scanner has been designed and fabricated. A modified fabrication process, along with a packaging scheme for this mm-LVD microlens scanner device was also presented. This device demonstrated vertical displacement of the focal plane of an integrated polymer microlens by up to 0.71 mm at an actuation voltage of 23 V. The lateral imaging resolution can be increased to as high as 1 μm using these devices.

CHAPTER 6 CONCLUSIONS AND FUTURE WORK

This research effort has successfully developed and demonstrated various MEMS optical scanners specifically designed for use in endoscopic biomedical imaging applications. The integration of MEMS-based endoscopes with these bioimaging modalities can potentially detect and diagnose internal cancers at an early stage using minimally invasive techniques.

Reflective micromirror scanners have been presented that used electrothermal actuation to provide large rotational scans at voltages below 20 V. A single-axis micromirror was successfully packaged inside a 5-mm diameter endoscope with other optical components to provide endoscopic laser-beam steering. OCT images obtained using this MEMS-based OCT endoscope achieved imaging resolutions of 15 μm and 12 μm in the transverse and axial directions, respectively. *In vivo* cross-sectional OCT images covering an area of $4.0 \times 2.7 \text{ mm}^2$ were acquired at an imaging speed of 2 to 16 frames per second.

The optical design, alignment, and packaging issues were addressed through the design of another class of electrothermal micromirrors which used the large-vertical-displacement (LVD) microactuator. The LVD microactuator used two complementarily-oriented electrothermal actuators, to keep the mirror surface parallel to the substrate and also to provide it bi-directional scanning capability. LVD micromirrors demonstrated large rotational scans, as well as the ability to generate large vertical piston motion at low

driving voltages. The LVD microactuator design can potentially achieve maximum vertical displacements of a few millimeters with millimeter-sized devices. Scanning LVD micromirrors have demonstrated endoscopic imaging capability through their use in nonlinear optical endoscopy. The micromirrors were scanned in a raster-scan pattern to obtain two-dimensional two-photon excitation fluorescence and second harmonic generation images with very high resolution ($\sim 1.5 \mu\text{m}$).

Finally, a microlens scanner using the LVD microactuator was reported. This device can physically scan the focal plane of an integrated polymer microlens and is therefore suitable for axial focus scanning applications. A fabricated device demonstrated an axial displacement of as high as 0.71 mm at a voltage of 23 V. This microlens scanner was successfully packaged inside a 5-mm endoscope for high-resolution, endoscopic OCM imaging. Till date, OCM imaging has been possible only on bench-top systems. However, the scan-range and imaging resolution provided by the microlens scanner demonstrates the potential of developing endoscopic OCM systems using this technology.

The large actuation range, low driving voltages, and small footprint of these optical microscanners make them very suitable for endoscopic biomedical imaging applications. These experiments show very promising imaging resolution which is critical to enable early detection of cancerous markers. The high resolution along with the scanning speed, open up the possibility to make compact, high-performance endoscopes for future clinical applications through the use of microsystem technology.

6.1 Research Effort Accomplishments

The following tasks have been accomplished for this project:

- Four variations of 1-D micromirror devices were designed, fabricated, characterized and packaged for project collaborators at the State University of New York, Stony Brook, NY.
- The 2-D micromirror devices were characterized, and a 4 by 4 pixel laser scan pattern at 10 frames per second was demonstrated.
- The large-vertical-displacement (LVD) microactuator was invented and designed.
- The 1-D LVD micromirror was developed, and its bi-directional scanning and large piston motion capabilities at low actuation voltages was demonstrated. This device also generated optical scans greater than 170° at its resonance of 2.6 kHz.
- A 2-D LVD micromirror was developed, and static as well as dynamic 2-D bi-directional scanning was demonstrated.
- A LVD microlens scanner was fabricated and this sub-millimeter size prototype device demonstrated a maximum vertical displacement of $280\ \mu\text{m}$ at an actuation voltage of 10 V.
- A millimeter-range LVD microlens scanner has been designed and fabricated, and it demonstrated a vertical displacement of 0.71 mm at 23 V.
- The millimeter-range LVD microlens scanner has been successfully packaged inside a 5-mm diameter endoscope for OCM imaging.
- Endoscopic OCT imaging was demonstrated using the 1-D micromirror scanners to image *in vivo* tissue with resolutions around $10\ \mu\text{m}$.

- Nonlinear optical endoscopy has been accomplished using the 1-D and 2-D micromirrors to obtain images with lateral resolution of about 1.5 μm .

6.2 Future Work

The optical scanners and the endoscopic biomedical imaging techniques demonstrated in this research work show great potential for their intended application of *in vivo* detection of precancerous lesions. However to realize this end goal, additional development and verification is required.

From an imaging standpoint, experimental demonstration is needed to verify the capability of the 2-D micromirrors for lateral scanning in OCT systems to obtain 3D OCT images in real-time. Till date, the 2-D micromirrors have only been demonstrated for nonlinear optical imaging. The mm-range LVD microlens scanner should be integrated with an existing OCT setup to demonstrate OCM imaging capability.

It is possible to design millimeter range LVD scanners that do not suffer from lateral shifting effects. The new design should be able to maintain the lateral position of the microlens for the entire vertical displacement range.

A more comprehensive lumped element model for the LVD microactuation scheme should be developed. The existing static model is valid only when one of the two actuators is electrically activated, and is therefore unsuitable to model the LVD piston motion operation mode. A dynamic model is also needed which will help to design optimized devices in the future.

All MEMS devices presented in this dissertation were fabricated at the die-level using variations of the DRIE CMOS-MEMS process. For commercial volume production, the feasibility of wafer-level processing must be investigated. Since

electronic circuits are not required by these devices, a non-CMOS fabrication process, presented in Appendix A, that uses SOI wafers can be easily developed.

APPENDIX A
NON-CMOS, WAFER LEVEL FABRICATION PROCESS

The MEMS devices presented in this dissertation have been fabricated at the die level using variations of a post-CMOS micromachining process. Since on-chip electrical circuitry is not required for these devices, there is no added advantage in using the CMOS process. From a volume manufacturability point of view, these optical microscanners can be batch fabricated at the wafer level using only five lithography steps. The non-CMOS, wafer level fabrication process is presented in this appendix.

Figure A-1 illustrates the proposed wafer-level fabrication process that uses the device layer of a silicon-on-insulator (SOI) wafer to define the single-crystal-silicon (SCS) thickness under the microstructure. This process uses only 5 lithographic steps, and can simultaneously produce both thin-film and bulk-Si microstructures. All devices presented in this dissertation can be fabricated using this non-CMOS process.

Step 1: Deposit silicondioxide on SOI wafer

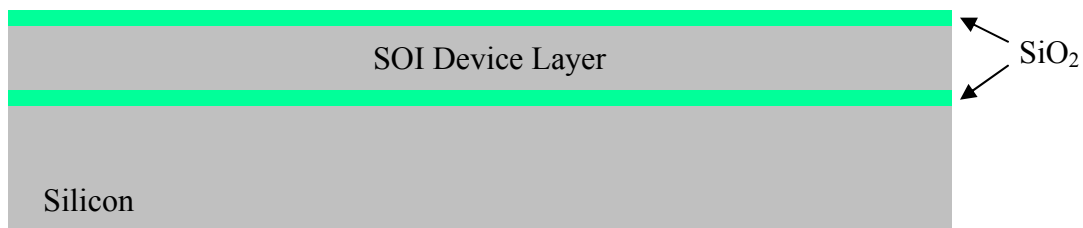
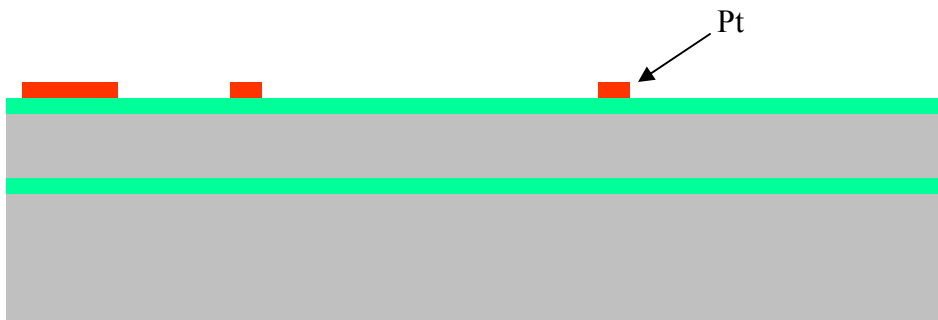
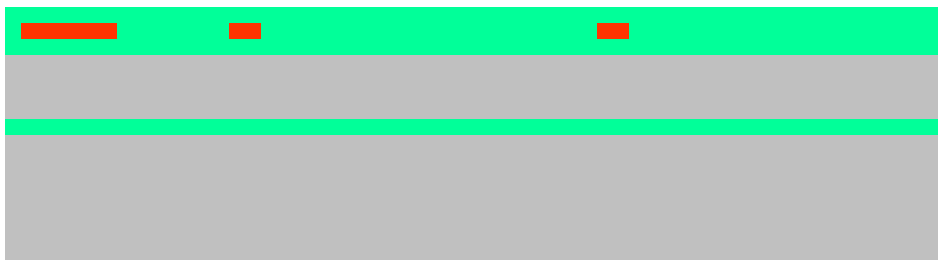


Figure A-1: Non-CMOS, wafer-level fabrication process illustrating the steps required to fabricate the 1-D LVD micromirror device.

Step 2: Deposit platinum layer and pattern (Mask 1)



Step 3: Deposit silicondioxide layer



Step 4: Pattern and etch SiO₂ to open contact to buried Pt layer (Mask 2)

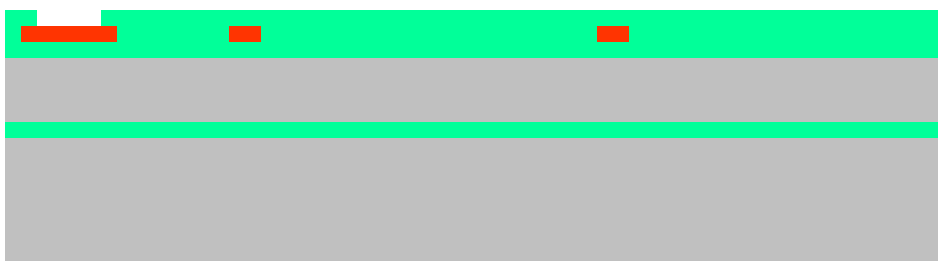
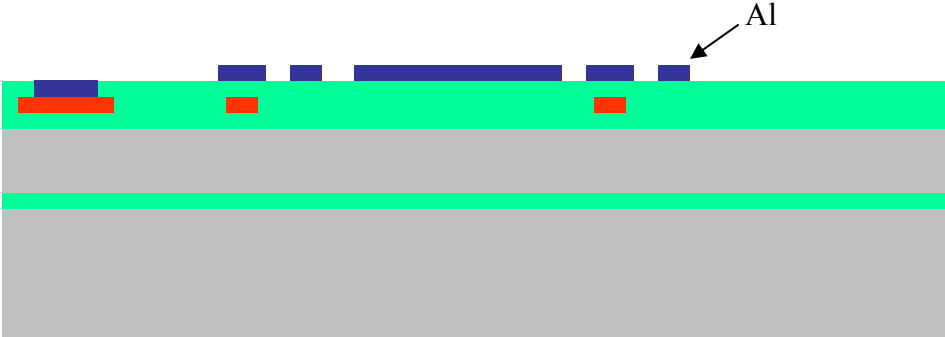
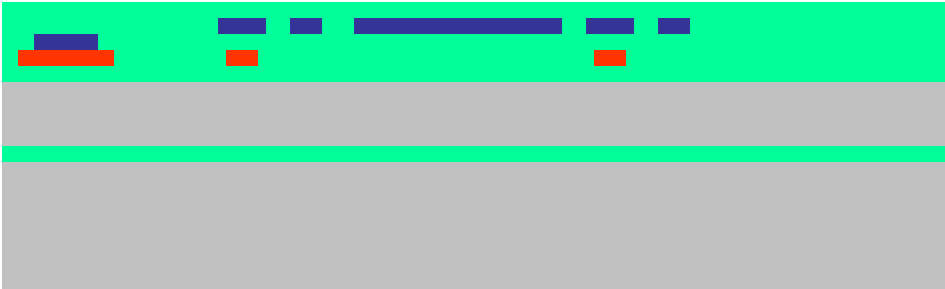


Figure A-1. Continued

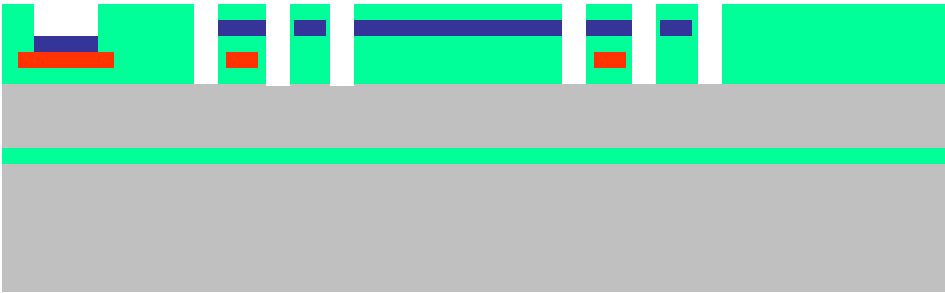
Step 5: Deposit aluminum layer and pattern (Mask 3)



Step 6: Deposit another silicon dioxide layer



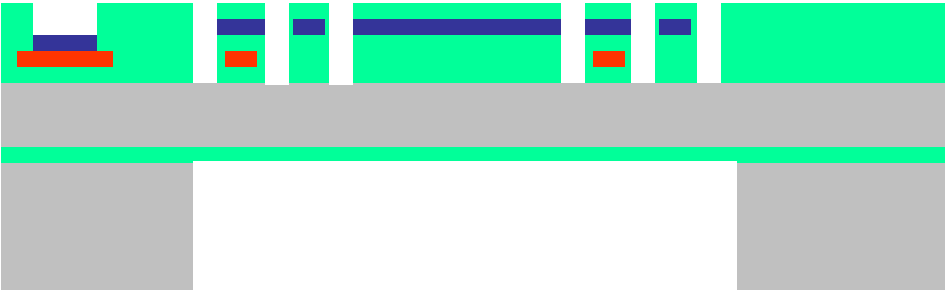
Step 7: Pattern and anisotropically etch SiO₂ till Si is exposed (Mask 4)



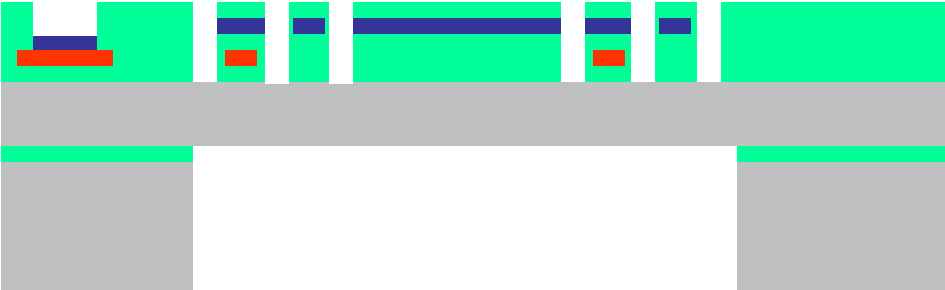
Legend	 : Si	 : SiO ₂	 : Pt	 : Al
--------	--	--	--	--

Figure A-1. Continued

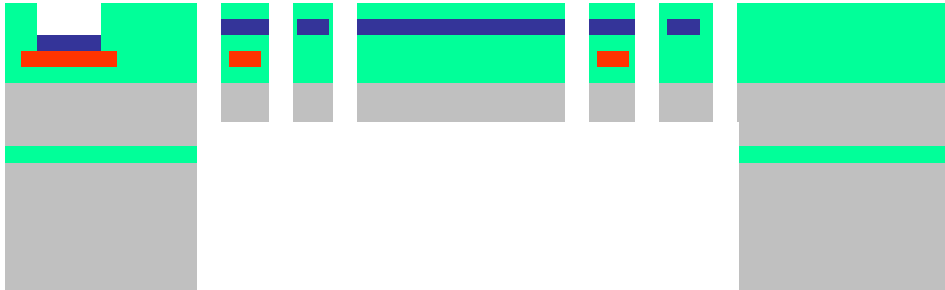
Step 8: Pattern and etch backside Si to stop at the buried SiO₂ layer (Mask 5)



Step 9: Backside etch of the buried SiO₂ layer only



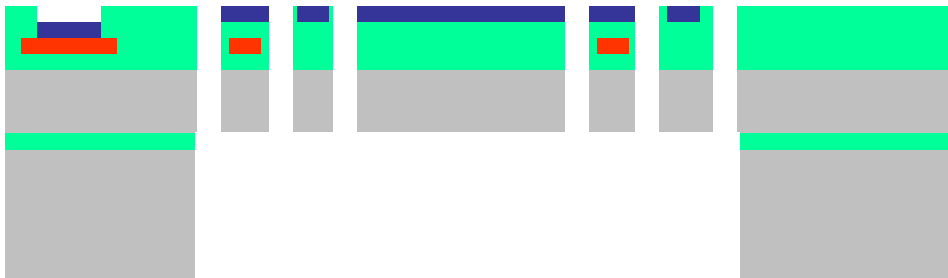
Step 10: Frontside anisotropic etch of Si using the top SiO₂ layer as the etch mask



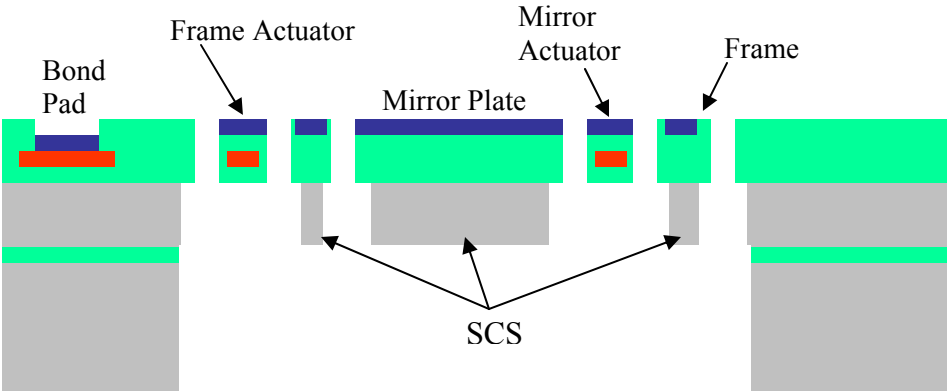
Legend	 : Si	 : SiO ₂	 : Pt	 : Al
--------	--	--	--	--

Figure A-1. Continued

Step 11: Frontside timed dry etch of SiO₂ to expose the Al layer



Step 12: Isotropic etch of Si to form the thin-film bimorph actuator beams



Legend	 : Si	 : SiO ₂	 : Pt	 : Al
--------	--	--	--	--

Figure A-1. Continued

APPENDIX B
ARTICLES GENERATED BY THIS RESEARCH EFFORT

The referred archival journal (J) and conference (C) publications generated by this research effort (for each individual micro-scanner) are listed below:

1-D Micromirror

- C1: A. Jain, S. T. Todd, G. K. Fedder, and H. Xie, "A Large-Scanning-Angle, Electrothermal SCS Micromirror for Biomedical Imaging," *Frontiers in Optics, The 87th OSA Annual Meeting*, Tucson, AZ, October 2003.
- C2: H. Xie, A. Jain, T. Xie, Y. Pan, and G. K. Fedder, "A Single-Crystal Silicon-based Micromirror with Large Scanning Angle for Biomedical Applications," *Conference on Lasers and Electro-Optics (CLEO) 2003*, Baltimore, MD, June 2003.

2-D Micromirror

- J1: A. Jain, A. Kopa, Y. Pan, G. K. Fedder, and H. Xie, "A Two-Axis Electrothermal Micromirror for Endoscopic Optical Coherence Tomography," *IEEE Journal of Selected Topics in Quantum Electronics* 10, pp. 636-642 (2004).
- C3: A. Jain, T. Xie, Y. Pan, G. K. Fedder, and H. Xie, "A Two-Axis Electrothermal SCS Micromirror for Biomedical Imaging," *2003 IEEE/LEOS International Conference on Optical MEMS*, Waikoloa, HI, August 2003.
- C4: A. Kopa, A. Jain, and H. Xie, "Laser Scanning Display using a 2-D Micromirror," *Optics in the South East (OISE) 2003*, Orlando, FL, November 2003.

1-D LVD Micromirror

- J2: A. Jain, H. Qu, S. Todd, and H. Xie, "A Thermal Bimorph Micromirror with Large Bi-Directional and Vertical Actuation," *Sensors and Actuators A* 122, pp. 9-15 (2005).
- C5: A. Jain, H. Qu, S. Todd, G. K. Fedder, and H. Xie, "Electrothermal SCS Micromirror with Large-Vertical-Displacement Actuation," *2004 Solid-State Sensor, Actuator and Microsystems Workshop*, Hilton Head Isl., SC, June 2004.

- C6: A. Jain, S. Todd, and H. Xie, "An Electrothermally-Actuated, Dual-Mode Micromirror for Large Bi-Directional Scanning," *IEEE International Electron Devices Meeting (IEDM) 2004*, pp. 47-50, San Francisco, CA, December 2004.

2-D LVD Micromirror

- J3: A. Jain and H. Xie, "A Single-Crystal-Silicon Micromirror for Large Bi-Directional 2-D Scanning Applications," *Sensors and Actuators A*, 2006 (In press).
- C7: A. Jain and H. Xie, "An Electrothermal SCS Micromirror for Large Bi-Directional 2-D Scanning," *13th International Conference on Solid-State Sensors, Actuators and Microsystems (Transducers '05)*, pp. 988-991, Seoul, Korea, June 2005.

LVD Microlens Scanner

- J4: A. Jain and H. Xie, "An Electrothermal Microlens Scanner with Low-Voltage, Large-Vertical-Displacement Actuation," *IEEE Photonics Technology Letters* 17, pp. 1971-1973 (2005).
- C8: A. Jain and H. Xie, "A Tunable Microlens Scanner with Large-Vertical-Displacement Actuation," *18th IEEE International Conference on Micro Electro Mechanical Systems (MEMS 2005)*, pp. 92-95, Miami, FL, January 2005.
- C9: A. Jain and H. Xie, "Half-Millimeter-Range Vertically Scanning Microlenses for Microscopic Focusing Applications," *2006 Solid-State Sensor, Actuator and Microsystems Workshop*, Hilton Head Isl., SC, June 2006.
- C10: A. Jain and H. Xie, "Endoscopic Microprobe with a LVD Microlens Scanner for Confocal Imaging," *2006 IEEE/LEOS International Conference on Optical MEMS*, Big Sky, MT, August 2006.

Biomedical Imaging

- J5: L. Fu, A. Jain, H. Xie, C. Cranfield, and M. Gu, "Nonlinear Optical Endoscopy based on a Double-clad Photonic Crystal Fiber and a MEMS Mirror," *Optics Express* 14, pp. 1027-1032 (2006).
- C11: Z. G. Wang, H. Adler, D. Chan, A. Jain, H. Xie, Z. L. Wu, and Y. T. Pan, "Cystoscopic Optical Coherence Tomography for Urinary Bladder Imaging in vivo," *Proceedings of SPIE* 6079, pp. 91-99, 2006.
- C12: L. Fu, A. Jain, H. Xie, C. Cranfield, and M. Gu, "Integration of a Double-clad Photonic Crystal Fiber, a GRIN lens and a MEMS Mirror for Nonlinear Optical Endoscopy," *Biomedical Optics 2006*, Ft. Lauderdale, FL, March 2006.

Book Chapter

H. Xie, S. Todd, and A. Jain, "Single-Crystal Silicon Based Electrothermal MEMS Mirrors for Biomedical Imaging Applications," in *MEMS/NEMS Handbook: Techniques and Applications*, edited by C. Leondes, Springer NY, 2005 (In press).

LIST OF REFERENCES

- [1] American Cancer Society, "Cancer Facts and Figures 2005," Atlanta, GA 2005.
- [2] V. Backman, L. T. Perelman, J. T. Arendt, R. Gurjar, M. G. Muller, Q. Zhang, G. Zonios, E. Kline, T. McGillican, T. Valdez, J. V. Dam, M. Wallace, K. Badizadegan, J. M. Crawford, M. Fitzmaurice, S. Kabani, H. S. Levin, M. Seiler, R.R.Dasari, I. Itzkan, and M. S. Feld, "Detection of Preinvasive Cancer Cells," *Nature*, vol. 406, pp. 35-36, 2000.
- [3] B. J. Reid, P. L. Blount, Z. Feng, and D. S. Levine, "Optimizing Endoscopic Biopsy Detection of Early Cancers in Barrett's High-Grade Dysplasia," *The American Journal of Gastroenterology*, vol. 95, pp. 3089-3096, 2000.
- [4] W. Drexler, "Ultrahigh-Resolution Optical Coherence Tomography," *Journal of Biomedical Optics*, vol. 9, pp. 47-74, 2004.
- [5] C. Pitris, M. E. Brezinski, B. E. Bouma, G. J. Tearney, J. F. Southern, and J. G. Fujimoto, "High Resolution Imaging of the Upper Respiratory Tract with Optical Coherence Tomography: A Feasibility Study," *American Journal Of Respiratory And Critical Care Medicine*, vol. 157, pp. 1640-1644, 1998.
- [6] D. Huang, E. A. Swanson, C. P. Lin, J. S. Schuman, W. G. Stinson, W. Chang, M. R. Hee, T. Flotte, K. Gregory, C. A. Puliafito, and J. G. Fujimoto, "Optical Coherence Tomography," *Science*, vol. 254, pp. 1178-1181, 1991.
- [7] B. E. Bouma and G. J. Tearney, *The Handbook of Optical Coherence Tomography*. New York: Marcel Dekker, Inc., 2002.
- [8] J. M. Schmitt, "Optical Coherence Tomography (OCT): A Review," *IEEE Journal of Selected Topics in Quantum Electronics*, vol. 5, pp. 1205-1215, 1999.
- [9] I.-K. Jang, G. Tearney, and B. Bouma, "Visualization of Tissue Prolapse Between Coronary Stent Struts by Optical Coherence Tomography: Comparison with Intravascular Ultrasound," *Circulation*, vol. 104, pp. 2754, 2001.
- [10] W. Drexler, U. Morgner, F. X. Kartner, C. Pitris, S. A. Boppart, X. D. Li, E. P. Ippen, and J. G. Fujimoto, "In vivo Ultrahigh-Resolution Optical Coherence Tomography," *Optics Letters*, vol. 24, pp. 1221-1223, 1999.

- [11] C. Passmann and H. Ermert, "A 100-MHz Ultrasound Imaging System for Dermatologic and Ophthalmologic Diagnostics," *IEEE Transactions on Ultrasonics, Ferroelectrics and Frequency Control*, vol. 43, pp. 545-552, 1996.
- [12] G. J. Tearney, M. E. Brezinski, B. E. Bouma, S. A. Boppart, C. Pitris, J. F. Southern, and J. G. Fujimoto, "In Vivo Endoscopic Optical Biopsy with Optical Coherence Tomography," *Science*, vol. 276, pp. 2037-2039, 1997.
- [13] B. E. Bouma and G. J. Tearney, "Clinical Imaging with Optical Coherence Tomography," *Academic Radiology*, vol. 9, pp. 942-953, 2002.
- [14] A. M. Sergeev, V. M. Gelikonov, G. V. Gelikonov, F. I. Feldchtein, R. V. Kuranov, N. D. Gladkova, N. M. Shakhova, L. B. Snopova, A. V. Shakhov, I. A. Kuznetzova, A. N. Denisenko, V. V. Pochinko, Y. P. Chumakov, and O. S. Streltsova, "In vivo Endoscopic OCT Imaging of Precancer and Cancer States of Human Mucosa," *Optics Express*, vol. 1, pp. 432-440, 1997.
- [15] T.-Q. Xie, M. L. Zeidel, and Y.-T. Pan, "Detection of Tumorigenesis in Urinary Bladder with Optical Coherence Tomography: Optical Characterization of Morphological Changes," *Optics Express*, vol. 10, pp. 1431-1443, 2002.
- [16] S. A. Boppart, B. E. Bouma, C. Pitris, G. J. Tearney, J. G. Fujimoto, and M. E. Brezinski, "Forward-Imaging Instruments for Optical Coherence Tomography," *Optics Letters*, vol. 22, pp. 1618-1620, 1997.
- [17] L. J. Hornbeck, "Digital Light Processing and MEMS: An Overview," Technical Digest of the IEEE/LEOS 1996 Summer Topical Meetings, Keystone, CO, Aug. 5-9, pp. 7-8, 1996.
- [18] D. S. Greywall, P. A. Busch, F. Pardo, D. W. Carr, G. Bogart, and H. T. Soh, "Crystalline Silicon Tilting Mirrors for Optical Cross-Connect Switches," *Journal of Microelectromechanical Systems*, vol. 12, pp. 708-712, 2003.
- [19] H. Xie, Y. Pan, and G. K. Fedder, "A SCS Micromirror for Optical Coherence Tomographic Imaging," Technical Digest of the 15th IEEE International Conference on Micro Electro Mechanical Systems (MEMS '02), Las Vegas, NV, Jan 20-24, pp. 495-499, 2002.
- [20] J. M. Zara, J. A. Izatt, K. D. Rao, S. Yazdanfar, and S. W. Smith, "Scanning Mirror for Optical Coherence Tomography Using an Electrostatic MEMS Actuator," Technical Digest of the 2002 IEEE International Symposium on Biomedical Imaging, Washington, DC, Jul. 7-10, pp. 297- 300, 2002.
- [21] J. T. W. Yeow, V. X. D. Yang, A. Chahwan, M. L. Gordon, B. Qi, I. A. Vitkin, B. C. Wilson, and A. A. Goldenberg, "Micromachined 2-D Scanner for 3-D Optical Coherence Tomography," *Sensors and Actuators A*, vol. 117, pp. 331-340, 2005.

- [22] L. S. Fan, W. Piyawattanametha, M. C. Wu, A. D. Aguirre, P. R. Herz, Y. Chen, and J. G. Fujimoto, "High-resolution 3D OCT Imaging with a MEMS Scanning Endoscope," *Proceedings of the SPIE*, vol. 5719, pp. 140-143, 2005.
- [23] D. T. McCormick, W. Jung, Z. Chen, and N. C. Tien, "3-D MEMS Based Minimally Invasive Optical Coherence Tomography," Technical Digest of the 13th International Conference on Solid-State Sensors, Actuators and Microsystems (Transducers 2005), Seoul, Korea, Jun. 5-9, pp. 1644-1648, 2005.
- [24] J. M. Zara, S. Yazdanfar, K. D. Rao, J. A. Izatt, and S. W. Smith, "Electrostatic Micromachine Scanning Mirror for Optical Coherence Tomography," *Optics Letters*, vol. 22, pp. 628-630, 2003.
- [25] P. H. Tran, D. S. Mukai, M. Brenner, and Z. Chen, "In vivo Endoscopic Optical Coherence Tomography by use of a Rotational Microelectromechanical System Probe," *Optics Letters*, vol. 29, pp. 1236-1238, 2004.
- [26] P. R. Herz, Y. Chen, A. D. Aguirre, K. Schneider, P. Hsiung, J. G. Fujimoto, K. Madden, J. Schmitt, J. Goodnow, and C. Petersen, "Micromotor Endoscope Catheter for invivo, Ultrahigh-Resolution Optical Coherence Tomography," *Optics Letters*, vol. 29, pp. 2261-2263, 2004.
- [27] H. Xie, A. Jain, T. Xie, Y. Pan, and G. K. Fedder, "A Single-Crystal Silicon-Based Micromirror with Large Scanning Angle for Biomedical Applications," Technical Digest of the Conference on Lasers and Electro-Optics (CLEO 2003), Baltimore, MD, Jun. 1-6, 2003.
- [28] A. Jain, S. T. Todd, G. K. Fedder, and H. Xie, "A Large-Scanning-Angle, Electrothermal SCS Micromirror for Biomedical Imaging," Technical Digest of the 2003 OSA Annual Meeting, Tuscon, AZ, Oct. 6, 2003.
- [29] A. Jain, T. Xie, Y. Pan, G. K. Fedder, and H. Xie, "A Two-Axis SCS Electrothermal Micromirror for Biomedical Imaging," Technical Digest of the 2003 IEEE/LEOS International Conference on Optical MEMS, Waikoloa, Hawaii, Aug. 18-21, pp. 14-15, 2003.
- [30] A. Jain, A. Kopa, Y. Pan, G. K. Fedder, and H. Xie, "A Two-Axis Electrothermal Micromirror for Endoscopic Optical Coherence Tomography," *IEEE Journal of Selected Topics in Quantum Electronics*, vol. 10, pp. 636-642, 2004.
- [31] H. Xie, *Gyroscope and Micromirror Design Using Vertical Axis CMOS-MEMS Actuation and Sensing*, Ph.D. Dissertation, Carnegie Mellon University, Pittsburgh, PA, 2002
- [32] R. C. Youngquist, S. Carr, and D. E. N. Davies, "Optical Coherence-Domain Reflectometry: A New Optical Evaluation Technique," *Optics Letters*, vol. 12, pp. 158-160, 1987.

- [33] K. Takada, I. Yokohama, K. Chida, and J. Noda, "New Measurement System for Fault Location in Optical Waveguide Devices Based on an Interferometric Technique," *Applied Optics*, vol. 26, pp. 1603-1606, 1987.
- [34] P. Beaud, J. Schutz, W. Hodel, H. P. Weber, H. H. Gilgen, and R. P. Salathe, "Optical Reflectometry with Micrometer Resolution for the Investigation of Integrated Optical Devices," *IEEE Journal of Quantum Electronics*, vol. 25, pp. 755-759, 1989.
- [35] Y. Pan, E. Lanckenau, J. Welzel, R. Birngruber, and R. Engelhardt, "Optical Coherence-Gated Imaging of Biological Tissues," *IEEE Journal of Selected Topics in Quantum Electronics*, vol. 2, pp. 1029-1034, 1996.
- [36] J. M. Schmitt and A. Knüttel, "Model of Optical Coherence Tomography of Heterogeneous Tissue," *Journal of Optical Society of America A*, vol. 14, pp. 1231-1242, 1997.
- [37] J. Welzel, "Optical Coherence Tomography in Dermatology: A Review," *Skin Research and Technology*, vol. 7, pp. 1-9, 2001.
- [38] A. G. Podoleanu, J. A. Rogers, D. A. Jackson, and S. Dunne, "Three Dimensional OCT Images from Retina and Skin," *Optics Express*, vol. 7, pp. 292-298, 2000.
- [39] I.-K. Jang, B. E. Bouma, D.-H. Kang, S.-J. Park, S.-W. Park, K.-B. Seung, K.-B. Choi, M. Shishkov, K. Schlendorf, E. Pomerantsev, S. L. Houser, H. T. Artez, and G. J. Tearney, "Visualization of Coronary Atherosclerotic Plaques in Patients Using Optical Coherence Tomography: Comparison With Intravascular Ultrasound," *Journal of the American College of Cardiology*, vol. 39, pp. 604-609, 2002.
- [40] J. A. Izatt, M. R. Hee, G. M. Owen, E. A. Swanson, and J. G. Fujimoto, "Optical Coherence Microscopy in Scattering Media," *Optics Letters*, vol. 19, pp. 590-592, 1994.
- [41] J. Schmitt, M. Yadlowsky, and R. Bonner, "Subsurface Imaging of Living Skin with Optical Coherence Microscopy," *Dermatology*, vol. 191, pp. 93-98, 1995.
- [42] F. I. Feldchtein, V. M. Gelikonov, R. R. Iksanov, G. V. Gelikonov, R. V. Kuranov, A. M. Sergeev, N. Gladkova, M. N. Ourutina, D. H. Reitze, and J. A. Warren, "In vivo OCT Imaging of Hard and Soft Tissue of the Oral Cavity," *Optics Express*, vol. 3, pp. 239-250, 1998.
- [43] B. M. Hoeling, A. D. Fernandez, R. C. Haskell, E. Huang, W. R. Myers, D. C. Peterson, S. E. Ungersma, R. Wang, M. E. Williams, and S. E. Fraser, "An Optical Coherence Microscope for 3-Dimensional Imaging in Developmental Biology," *Optics Express*, vol. 6, pp. 136-146, 2000.

- [44] J. G. Fujimoto, M. E. Brezinski, G. J. Tearney, S. A. Boppart, B. Bouma, M. R. Hee, J. F. Southern, and E. A. Swanson, "Optical Biopsy and Imaging Using Optical Coherence Tomography," *Nature Medicine*, vol. 1, pp. 970-972, 1995.
- [45] J. M. Schmitt, S. L. Lee, and K. M. Yung, "An Optical Coherence Microscope with Enhanced Resolving Power in Thick Tissue," *Optics Communications*, vol. 142, pp. 203-207, 1997.
- [46] R. Windecker, M. Fleischer, and B. Franze, "Two Methods for Fast Coherence Tomography and Topometry," *Journal of Modern Optics*, vol. 44, pp. 967-978, 1997.
- [47] X. Li, C. Chudoba, T. Ko, C. Pitris, and J. G. Fujimoto, "Imaging Needle for Optical Coherence Tomography," *Optics Letters*, vol. 25, pp. 1520-1522, 2000.
- [48] X. Li, T. H. Ko, and J. G. Fujimoto, "Intraluminal Fiber-Optic Doppler Imaging Catheter for Structural and Functional Optical Coherence Tomography," *Optics Letters*, vol. 26, pp. 1906-1908, 2001.
- [49] B. E. Bouma and G. J. Tearney, "Power-Efficient Nonreciprocal Interferometer and Linear Scanning Fiber-Optic Catheter for Optical Coherence Tomography," *Optics Letters*, vol. 24, pp. 531-533, 1999.
- [50] X. D. Li, X. M. Liu, Y. C. Chen, M. J. Cobb, and M. B. Kimmey, "Development of a Fast Scanning Miniature Probe and Methods of Dispersion Management for High-Resolution Optical Coherence Tomography," Technical Digest of the 26th Annual International Conference of the IEEE EMBS, San Francisco, CA, Sep. 1-5, pp. 5289-5291, 2004.
- [51] H. Xie, Y. Pan, and G. K. Fedder, "Endoscopic Optical Coherence Tomography Imaging with a CMOS-MEMS Micromirror," *Sensors and Actuators A*, vol. 103, pp. 237-241, 2003.
- [52] T. Xie, H. Xie, G. K. Fedder, and Y. Pan, "Endoscopic Optical Coherence Tomography with a Modified Microelectromechanical Systems Mirror for Detection of Bladder Cancers," *Applied Optics*, vol. 42, pp. 6422-6426, 2003.
- [53] Y. Pan, H. Xie, and G. K. Fedder, "Endoscopic Optical Coherence Tomography Based on a Microelectromechanical Mirror," *Optics Letters*, vol. 26, pp. 1966-1968, 2001.
- [54] B. Qi, A. P. Himmer, L. M. Gordon, X. D. Yang, L. D. Dickensheets, and I. A. Vitkin, "Dynamic Focus Control in High-Speed Optical Coherence Tomography Based on a Microelectromechanical Mirror," *Optics Communications*, vol. 232, pp. 123-128, 2004.

- [55] F. Lexer, C. K. Hitzinger, W. Drexler, S. Molebny, H. Sattmann, M. Sticker, and A. F. Fercher, "Dynamic Coherent Focus OCT with Depth-Independent Transversal Resolution," *Journal of Modern Optics*, vol. 46, pp. 541-553, 1999.
- [56] J. A. Izatt, M. D. Kulkarni, H.-W. Wang, K. Kobayashi, and J. M. V. Sivak, "Optical Coherence Tomography and Microscopy in Gastrointestinal Tissues," *IEEE Journal of Selected Topics in Quantum Electronics*, vol. 2, pp. 1017-1028, 1996.
- [57] J. W. Hettinger, M. d. I. P. Mattozzi, W. R. Myers, M. E. Williams, A. Reeves, R. L. Parsons, R. C. Haskell, D. C. Petersen, R. Wang, and J. I. Medford, "Optical Coherence Microscopy. A Technology for Rapid, in vivo, Non-Destructive Visualization of Plants and Plant Cells," *Plant Physiology*, vol. 123, pp. 3-16, 2000.
- [58] A. D. Aguirre, P. Hsiung, T. H. Ko, I. Hartl, and J. G. Fujimoto, "High-Resolution Optical Coherence Microscopy for High-Speed, in vivo Cellular Imaging," *Optics Letters*, vol. 28, pp. 2064-2066, 2003.
- [59] Z. Ding, H. Ren, Y. Zhao, J. S. Nelson, and Z. Chen, "High-resolution Optical Coherence Tomography Over a Large Depth Range with an Axicon Lens," *Optics Letters*, vol. 27, pp. 243-245, 2002.
- [60] S. Kwon, V. Milanovic, and L. P. Lee, "Vertical Microlens Scanner for 3D Imaging," Technical Digest of the 2002 Solid-State Sensor and Actuator Workshop, Hilton Head Isl., SC, Jun. 2-6, pp. 227-230, 2002.
- [61] S. Kwon and L. P. Lee, "Stacked Two Dimensional Micro-Lens Scanner for Micro Confocal Imaging Array," Technical Digest of the 15th IEEE International Conference on Micro Electro Mechanical Systems (MEMS 2002), Las Vegas, NV, Jan. 20-24, pp. 483-486, 2002.
- [62] S. Kwon, V. Milanovic, and L. P. Lee, "Large-Displacement Vertical Microlens Scanner with Low Driving Voltage," *IEEE Photonics Technology Letters*, vol. 14, pp. 1572-1574, 2002.
- [63] D. F. Eaton, "Nonlinear Optical Materials," *Science*, vol. 253, pp. 281-287, 1991.
- [64] A. Diaspro, *Confocal and Two-Photon Microscopy: Foundations, Applications, and Advances*. New York: Wiley-Liss, 2002.
- [65] W. R. Zipfel, R. M. Williams, and W. W. Webb, "Nonlinear Magic: Multiphoton Microscopy in the Biosciences," *Nature Biotechnology*, vol. 21, pp. 1369-1377, 2003.
- [66] W. Denk, J. H. Strickler, and W. W. Webb, "Two-Photon Laser Scanning Fluorescence Microscopy," *Science*, vol. 248, pp. 73-76, 1990.

- [67] G. Marriott and I. Parker, "Biophotonics, Part B," in *Methods in Enzymology*, vol. 361, J. N. Abelson and M. I. Simon, Eds. San Diego: Academic Press, 2003.
- [68] P. J. Campagnola and L. M. Loew, "Second-Harmonic Imaging Microscopy for Visualizing Biomolecular Arrays in Cells, Tissues and Organisms," *Nature Biotechnology*, vol. 21, pp. 1356-1360, 2003.
- [69] M. C. Skala, J. M. Squirrell, K. M. Vrotos, J. C. Eickhoff, A. Gendron-Fitzpatrick, K. W. Eliceiri, and N. Ramanujam, "Multiphoton Microscopy of Endogenous Fluorescence Differentiates Normal, Precancerous, and Cancerous Squamous Epithelial Tissues," *Cancer Research*, vol. 65, pp. 1180-1186, 2005.
- [70] J. C. Jung and M. J. Schnitzer, "Multiphoton Endoscopy," *Optics Letters*, vol. 28, pp. 902-904, 2003.
- [71] F. Helmchen, M. S. Fee, D. W. Tank, and W. Denk, "A Miniature Head-Mounted Two-Photon Microscope: High-Resolution Brain Imaging in Freely Moving Animals," *Neuron*, vol. 31, pp. 903-912, 2001.
- [72] B. A. Flusberg, J. C. Jung, E. D. Cocker, E. P. Anderson, and M. J. Schnitzer, "In vivo Brain Imaging Using a Portable 3.9 gram Two-Photon Fluorescence Microendoscope," *Optics Letters*, vol. 30, pp. 2272-2274, 2005.
- [73] W. Gobel, J. N. D. Kerr, A. Nimmerjahn, and F. Helmchen, "Miniaturized Two-Photon Microscope Based on a Flexible Coherent Fiber Bundle and a Gradient-Index Lens Objective," *Optics Letters*, vol. 29, pp. 2521-2523, 2004.
- [74] D. Bird and M. Gu, "Two-Photon Fluorescence Endoscopy with a Micro-Optic Scanning Head," *Optics Letters*, vol. 28, pp. 1552-1554, 2003.
- [75] M. T. Myaing, D. J. MacDonald, and X. Li, "Fiber-Optic Scanning Two-Photon Fluorescence Endoscope," *Optics Letters*, vol. 31, pp. 1076-1078, 2006.
- [76] L. Fu, A. Jain, H. Xie, C. Cranfield, and M. Gu, "Nonlinear Optical Endoscopy Based on a Double-Clad Photonic Crystal Fiber and a MEMS Mirror," *Optics Express*, vol. 14, pp. 1027-1032, 2006.
- [77] L. Fu, A. Jain, H. Xie, C. Cranfield, and M. Gu, "Integration of a Double-clad Photonic Crystal Fiber, a GRIN Lens and a MEMS Mirror for Nonlinear Optical Endoscopy," Technical Digest of the Biomedical Optics 2006, Ft. Lauderdale, FL, Mar. 19-22, 2006.
- [78] W. Piyawattanametha, R. P. J. Barretto, T. H. Ko, B. A. Flusberg, E. D. Cocker, H. Ra, D. Lee, O. Solgaard, and M. J. Schnitzer, "Fast-Scanning Two-Photon Fluorescence Imaging Based on a Microelectromechanical Systems Two-Dimensional Scanning Mirror," *Optics Letters*, vol. 31, pp. 2018-2020, 2006.

- [79] J. M. Bustillo, R. T. Howe, and R. S. Muller, "Surface Micromachining for Microelectromechanical Systems," *Proceedings of the IEEE*, vol. 86, pp. 1552-1574, 1998.
- [80] G. T. A. Kovacs, N. I. Maluf, and K. E. Petersen, "Bulk Micromachining of Silicon," *Proceedings of the IEEE*, vol. 86, pp. 1536-1551, 1998.
- [81] P. F. V. Kessel, L. J. Hornbeck, R. E. Meier, and M. R. Douglass, "A MEMS-Based Projection Display," *Proceedings of the IEEE*, vol. 98, pp. 1687-1704, 1998.
- [82] R. A. Conant, P. Hagelin, U. Krishnamoorthy, O. Solgaard, K. Y. Lau, and R. S. Muller, "A Raster-Scanning Full-Motion Video Display Using Polysilicon Micromachined Mirrors," *Sensors and Actuators A*, vol. 83, pp. 291-296, 2000.
- [83] T. W. Yeow, K. Y. Lim, B. Wilson, and A. A. Goldenberg, "A Low-Voltage Electrostatically Actuated MEMS Scanner for in vivo Biomedical Imaging," Technical Digest of the 2nd Annual International IEEE-EMB Special Topic Conference on Microtechnologies in Medicine & Biology, Madison, WI, May 2-4, pp. 205-207, 2002.
- [84] S. Schweizer, P. Cousseau, G. Lammel, S. Calmes, and P. Renaud, "Two-Dimensional Thermally Actuated Optical Microprojector," *Sensors and Actuators A*, vol. 85, pp. 424-429, 2000.
- [85] M.-H. Kiang, O. Solgaard, K. Y. Lau, and R. S. Muller, "Electrostatic Combedrive-Actuated Micromirrors for Laser-Beam Scanning and Positioning," *Journal of Microelectromechanical Systems*, vol. 7, pp. 27-37, 1998.
- [86] J. J. Bernstein, W. P. Taylor, J. D. Brazzle, C. J. Corcoran, G. Kirkos, J. E. Odhner, A. Pareek, M. Waelti, and M. Zai, "Electromagnetically Actuated Mirror Arrays for use in 3-D Optical Switching Applications," *Journal of Microelectromechanical Systems*, vol. 13, pp. 526- 535, 2004.
- [87] A. Baba, H. Okano, H. Uetsuka, and M. Esashi, "2 Axes Optical Switch with Holding Mechanism," Technical Digest of the 16th IEEE International Conference on Micro Electro Mechanical Systems (MEMS 2003), Kyoto, Japan, Jan. 19-23, pp. 251-254, 2003.
- [88] S. J. Kim, Y. H. Cho, H. J. Nam, and J. U. Bu, "Piezoelectrically Pushed Rotational Micromirrors for Wide-Angle Optical Switch Applications," Technical Digest of the 16th IEEE International Conference on Micro Electro Mechanical Systems (MEMS 2003), Kyoto, Japan, Jan. 19-23, pp. 263-266, 2003.
- [89] H. Schenk, P. Durr, T. Haase, D. Kunze, U. Sobe, H. Lakner, and H. Kuck, "Large Deflection Micromechanical Scanning Mirrors for Linear Scans and Pattern Generation," *IEEE Journal of Selected Topics in Quantum Electronics*, vol. 6, pp. 715-722, 2000.

- [90] G.-D. Su, H. Toshiyoshi, and M. C. Wu, "Surface-Micromachined 2-D Optical Scanners with High-Performance Single-Crystalline Silicon Micromirrors," *IEEE Photonics Technology Letters*, vol. 13, pp. 606-608, 2001.
- [91] L. Fan and M. C. Wu, "Two-Dimensional Optical Scanner with Large Angular Rotation Realized by Self-Assembled Micro-Elevator," Technical Digest of the 1998 IEEE/LEOS Summer Topical Meetings, Monterey, CA, Jul. 20-24, pp. II/107-II/108, 1998.
- [92] T. Kudrle, C. Wang, M. Bancu, J. Hsiao, A. Pareek, M. Waelti, G. Kirkos, T. Shone, C. Fung, and C. Mastrangelo, "Single-Crystal Silicon Micromirror Array with Polysilicon Flexures," *Sensors and Actuators A*, vol. 119, pp. 559-566, 2005.
- [93] M. R. Dokmeci, A. Pareek, S. Bakshi, M. Waelti, C. D. Fung, K. H. Heng, and C. H. Mastrangelo, "Two-Axis Single-Crystal Silicon Micromirror Arrays," *Journal of Microelectromechanical Systems*, vol. 13, pp. 1006-1017, 2004.
- [94] Z. Hao, B. Wingfield, M. Whitley, J. Brooks, and J. A. Hammer, "A Design Methodology for a Bulk-Micromachined Two-Dimensional Electrostatic Torsion Micromirror," *Journal of Microelectromechanical Systems*, vol. 12, pp. 692-701, 2003.
- [95] J. Kim and L. Lin, "Batch-Fabricated Scanning Micromirrors Using Localized Plastic Deformation of Silicon," Technical Digest of the 17th IEEE International Conference on Micro Electro Mechanical Systems (MEMS 2004), Maastricht, The Netherlands, 25-29 Jan., pp. 494 – 497, 2004.
- [96] R. A. Conant, J. T. Nee, K. Y. Lau, and R. S. Muller, "A Flat High-Frequency Scanning Micromirror," Technical Digest of the 2000 Solid-State Sensor & Actuator Workshop, Hilton Head, SC, Jun. 2-6, pp. 6-9, 2000.
- [97] H. Xie, Y. Pan, and G. K. Fedder, "A CMOS-MEMS Mirror with Curled-Hinge Comb Drive," *Journal of Microelectromechanical Systems*, vol. 12, pp. 450-457, 2003.
- [98] P. R. Patterson, D. Hah, N. Hung, H. Toshiyoshi, R. Chao, and M. C. Wu, "A Scanning Micromirror with Angular Comb Drive Actuation," Technical Digest of the 15th IEEE International Conference on Micro Electro Mechanical Systems (MEMS 2002), Jan. 20-24, pp. 544-547, 2002.
- [99] U. Krishnamoorthy, D. Lee, and O. Solgaard, "Self-Aligned Vertical Electrostatic Combedrives for Micromirror Actuation," *Journal of Microelectromechanical Systems*, vol. 12, pp. 458-464, 2003.
- [100] V. Milanovic, M. Last, and K. S. J. Pister, "Laterally Actuated Torsional Micromirrors for Large Static Deflection," *IEEE Photonics Technology Letters*, vol. 15, pp. 245-247, 2003.

- [101] V. Milanovic, G. A. Mathus, and D. T. McCormick, "Gimbal-Less Monolithic Silicon Actuators for Tip-Tilt-Piston Micromirror Applications," *IEEE Journal of Selected Topics in Quantum Electronics*, vol. 10, pp. 462-471, 2004.
- [102] H. Schenk, P. Durr, D. Kunze, H. Lakner, and H. Kuck, "A Resonantly Excited 2D-Micro-Scanning-Mirror with Large Deflection," *Sensors and Actuators A*, vol. 89, pp. 104-111, 2001.
- [103] S. Kwon, V. Milanovic, and L. P. Lee, "Vertical Combdrive Based 2-D Gimbaled Micromirrors with Large Static Rotation by Backside Island Isolation," *IEEE Journal of Selected Topics in Quantum Electronics*, vol. 10, pp. 498-504, 2004.
- [104] W. Piyawattanametha, P. R. Patterson, D. Hah, H. Toshiyoshi, and M. C. Wu, "A 2-D Scanner by Surface and Bulk Micromachined Angular Vertical Comb Actuators," Technical Digest of the 2003 IEEE/LEOS International Conference on Optical MEMS, Waikoloa, Hawaii, Aug. 18-21, pp. 93-94, 2003.
- [105] J. Bühler, J. Funk, O. Paul, F.-P. Steiner, and H. Baltes, "Thermally Actuated CMOS Micromirrors," *Sensors and Actuators A*, vol. 46-47, pp. 572-575, 1995.
- [106] G. Lammel, S. Schweizer, and P. Renaud, *Optical Microscanners and Microspectrometers Using Thermal Bimorph Actuators*. Boston: Kluwer Academic, 2002.
- [107] R. Buser, N. F. d. Rooij, H. Tischauser, A. Dommann, and G. Staufert, "Biaxial Scanning Mirror Activated by Bimorph Structures for Medical Applications," *Sensors and Actuators A*, vol. 31, pp. 29-34, 1992.
- [108] S. Schweizer, S. Calmes, M. Laudon, and P. Renaud, "Thermally Actuated Optical Microscanner with Large Angle and Low Consumption," *Sensors and Actuators A*, vol. 706, pp. 470-477, 1999.
- [109] G. Lammel, S. Schweizer, and P. Renaud, "MEMS Infrared Gas Spectrometer Based on a Porous Silicon Tunable Filter," Technical Digest of the The 14th IEEE International Conference on Micro Electro Mechanical Systems (MEMS 2001), Interlaken, Switzerland, Jan. 21-25, pp. 578-581, 2001.
- [110] W. Riethmuller and W. Benecke, "Thermally Excited Silicon Microactuators," *IEEE Transactions on Electron Devices*, vol. 35, pp. 758-763, 1988.
- [111] Q. Liu and Q.-A. Huang, "Micro-Electro-Mechanical Digital-to-Analog Converter Based on a Novel Bimorph Thermal Actuator," Technical Digest of the IEEE Sensors 2002, Orlando, FL, Jun. 12-14, pp. 1036-1041 vol.2, 2002.
- [112] M. Sinclair, "A High Frequency Resonant Scanner Using Thermal Actuation," Technical Digest of the 15th IEEE International Conference on Micro Electro Mechanical Systems (MEMS 2002), Las Vegas, NV, Jan. 20-24, pp. 698-701, 2002.

- [113] J. W. Judy and R. S. Muller, "Magnetically Actuated, Addressable Microstructures," *Journal of Microelectromechanical Systems*, vol. 6, pp. 249-256, 1997.
- [114] I. J. Cho, K. S. Yun, H. K. Lee, J. B. Yoon, and E. Yoon, "A Low-Voltage Two-Axis Electromagnetically Actuated Micromirror with Bulk Silicon Mirror Plates and Torsion Bars," Technical Digest of the 15th IEEE International Conference on Micro Electro Mechanical Systems (MEMS 2002), Las Vegas, NV, Jan. 20-24, pp. 540-543, 2002.
- [115] J. Bernstein, W. P. Taylor, J. Brazzle, G. Kirkos, J. Odhner, A. Pareek, and M. Zai, "Two Axis-of-Rotation Mirror Array Using Electromagnetic MEMS," Technical Digest of the 16th IEEE International Conference on Micro Electro Mechanical Systems (MEMS 2003), Kyoto, Japan, Jan. 19-23, pp. 275- 278, 2003.
- [116] R. A. Miller and Y.-C. Tai, "Micromachined Electromagnetic Scanning Mirror," *Optical Engineering*, vol. 36, pp. 1399-1407, 1997.
- [117] T. Kawabata, M. Ikeda, H. Goto, M. Matsumoto, and T. Yada, "The 2-Dimensional Micro Scanner Integrated with PZT Thin Film Actuator," Technical Digest of the 1997 International Conference on Solid State Sensors and Actuators (Transducers '97), Chicago, IL, Jun. 16-19, pp. 339-342, 1997.
- [118] N. Kikuchi, Y. Haga, M. Maeda, W. Makishi, and M. Esashi, "Piezoelectric 2-D Micro Scanner for Minimally Invasive Therapy Fabricated Using Femtosecond Laser Ablation," Technical Digest of the 12th International Conference on Solid-State Sensors, Actuators and Microsystems (Transducers '03), Boston, MA, Jun. 8-12, pp. 603- 606, 2003.
- [119] H.-J. Nam, Y.-S. Kim, S.-M. Cho, Y. Yee, and J.-U. Bu, "Low Voltage PZT Actuated Tilting Micromirror with Hinge Structure," Technical Digest of the 2002 IEEE/LEOS International Conference on Optical MEMS, Lugano, Switzerland, Aug. 20-23, pp. 89-90, 2002.
- [120] G. Lin, C.-J. Kim, S. Konishi, and H. Fujita, "Design, Fabrication, And Testing Of A C-shape Actuator," Technical Digest of the The 8th International Conference on Solid-State Sensors and Actuators (Transducers 1995 and Eurosensors IX), Stockholm, Sweden, Jun. 25-29, pp. 416-419, 1995.
- [121] M. Ataka, A. Omodaka, N. Takeshima, and H. Fujita, "Fabrication and Operation of Polyimide Bimorph Actuators for a Ciliary Motion System," *Journal of Microelectromechanical Systems*, vol. 2, pp. 146-150, 1993.
- [122] H. Xie, L. Erdmann, X. Zhu, K. Gabriel, and G. K. Fedder, "Post-CMOS Processing for High-Aspect-Ratio Integrated Silicon Microstructures," *Journal of Microelectromechanical Systems*, vol. 11, pp. 93-101, 2002.

- [123] H. Qu, D. Fang, and H. Xie, "A Single-Crystal Silicon 3-Axis CMOS-MEMS Accelerometer," Technical Digest of the IEEE Sensors 2004, Vienna, Austria, Oct. 24-27, pp. 661-664, 2004.
- [124] H. Xie and G. K. Fedder, "Fabrication, Characterization, and Analysis of a DRIE CMOS-MEMS Gyroscope," *IEEE Sensors Journal*, vol. 3, pp. 622-631, 2003.
- [125] MOSIS Integrated Circuit Fabrication Service, Marina del Rey, CA.
- [126] F. Laermer and A. Schilp, "Method of Anisotropically Etching Silicon." US-Patent No. 5501893: Robert Bosch GmbH (Stuttgart, DE), March 26, 1996.
- [127] J. Bühler, *Deformable Micromirror Arrays by CMOS Technology*, Ph.D. Thesis, The Swiss Federal Institute of Technology, 1997
- [128] S. T. Todd and H. Xie, "An Analytical Electrothermal Model of a 1-D Electrothermal MEMS Micromirror," *Proceedings of the SPIE*, vol. 5649, pp. 344-353, 2004.
- [129] A. Kopa, A. Jain, and H. Xie, "Laser Scanning Display Using a 2-D Micromirror," Technical Digest of the Optics in the Southeast (OISE) 2003, Orlando, FL, Nov. 12-13, 2003.
- [130] Z. G. Wang, H. Adler, D. Chan, A. Jain, H. Xie, Z. L. Wu, and Y. T. Pan, "Cystoscopic Optical Coherence Tomography for Urinary Bladder Imaging in vivo," *Proceedings of the SPIE*, vol. 6079, pp. 91-99, 2006.
- [131] M. A. Helmbrecht, U. Srinivasan, C. Rembe, R. T. Howe, and R. S. Muller, "Micromirrors for Adaptive-Optics Arrays," Technical Digest of the 11th International Conference on Solid State Sensors and Actuators (Transducers '01 and Eurosensors XV), Munich, Germany, Jun. 10-14, 2001.
- [132] A. P. Lee, C. F. McConaghy, G. Sommargren, P. Krulevitch, and E. W. Campbell, "Vertical-Actuated Electrostatic Comb Drive with In Situ Capacitive Position Correction for Application in Phase Shifting Diffraction Interferometry," *Journal of Microelectromechanical Systems*, vol. 12, pp. 960-971, 2003.
- [133] S. W. Chung and Y. K. Kim, "Design and Fabrication of 10 x 10 Micro-Spatial Light Modulator Array for Phase and Amplitude Modulation," *Sensors and Actuators A*, vol. 78, pp. 63-70, 1999.
- [134] D. Lee, U. Krishnamoorthy, K. Yu, and O. Solgaard, "High-Resolution, High-Speed Microscanner in Single-Crystalline Silicon Actuated by Self-Aligned Dual-Mode Vertical Electrostatic Combedrive with Capability for Phased Array Operation," Technical Digest of the 12th International Conference on Solid State Sensors, Actuators and Microsystems (Transducers '03), Boston, MA, Jun. 8-12, pp. 576-579, 2003.

- [135] O. Cugat, P. Mounaix, S. Basrour, C. Divoux, and G. Reyne, "Deformable Magnetic Mirror for Adaptive Optics: First Results," Technical Digest of the 13th IEEE Annual International Conference on Micro Electro Mechanical Systems (MEMS 2000), Miyazaki, Japan, Jan. 23-27, pp. 485-490, 2000.
- [136] Y. Yee, H.-J. Nam, S.-H. Lee, J. U. Bu, Y.-S. Jeon, and S.-M. Cho, "PZT Actuated Micromirror for Nano-Tracking of Laser Beam for High-Density Optical Data Storage," Technical Digest of the 13th Annual International Conference on Micro Electro Mechanical Systems (MEMS 2000), Jan. 23-27, pp. 435-440, 2000.
- [137] A. Tuantranont, L. A. Liew, V. M. Bright, W. Zhang, and Y. C. Lee, "Phase-Only Micromirror Array Fabricated by Standard CMOS Process," *Sensors and Actuators A*, vol. 89, pp. 124-134, 2001.
- [138] Z.-L. Wan, A. Feinerman, H.-J. Zeng, and G. Friedman, "Electrocapillary Piston Motion and a Prototype of Phase-Manipulating Micromirror," *Journal of Microelectromechanical Systems*, vol. 13, pp. 620-627, 2004.
- [139] *CoventorWare 2003 Reference Manual*. Cary, NC: Coventor, Inc., 2003.
- [140] A. Jain, H. Qu, S. Todd, and H. Xie, "A Thermal Bimorph Micromirror with Large Bi-Directional and Vertical Actuation," *Sensors and Actuators A*, 2005.
- [141] A. Jain, H. Qu, S. Todd, G. K. Fedder, and H. Xie, "Electrothermal SCS Micromirror with Large-Vertical-Displacement Actuation," Technical Digest of the 2004 Solid-State Sensor, Actuator and Microsystems Workshop, Hilton Head Isl., SC, Jun. 6-10, pp. 228-231, 2004.
- [142] A. Jain, S. Todd, and H. Xie, "An Electrothermally-Actuated, Dual-Mode Micromirror for Large Bi-Directional Scanning," Technical Digest of the 2004 IEEE International Electron Devices Meeting (IEDM 2004), San Francisco, CA, Dec. 13-15, pp. 47-50, 2004.
- [143] A. Jain and H. Xie, "An Electrothermal SCS Micromirror for Large Bi-Directional 2-D Scanning," Technical Digest of the 13th International Conference on Solid-State Sensors, Actuators and Microsystems (Transducers 2005), Seoul, Korea, Jun. 5-9, pp. 988-991, 2005.
- [144] K. Hoshino and I. Shimoyama, "An Elastic Thin-Film Microlens Array with Pneumatic Actuator," Technical Digest of the The 14th IEEE International Conference on Micro Electro Mechanical Systems (MEMS 2001), Interlaken, Switzerland, Jan. 21-25, pp. 321-324, 2001.
- [145] S.-H. Kim, Y. Yee, J. Choi, H. Kwon, M.-H. Ha, C. Oh, and J. U. Bu, "Integrated Micro Optical Flying Head with Lens Positioning Actuator for Small Form Factor Data Storage," Technical Digest of the 12th International Conference on Solid-State Sensors, Actuators and Microsystems (Transducers '03), Boston, MA, Jun. 8-12, pp. 607-610, 2003.

- [146] R. Graham, "A Variable Focus Lens and Its Uses," *J. O. S. A.*, vol. 30, pp. 560-563, 1940.
- [147] N. Sugiura and S. Morita, "Variable-Focus Liquid-Filled Optical Lens," *Applied Optics*, vol. 32, pp. 4181-4186, 1993.
- [148] B. Berge and J. Peseux, "Variable Focal Length Controlled by an External Voltage: An Application of Electrowetting," *The European Physical Journal E*, vol. 3, pp. 159-163, 2000.
- [149] B. Berge, "Liquid Lens Technology: Principle of Electrowetting Based Lenses and Applications to Imaging," Technical Digest of the 18th IEEE International Conference on Micro Electro Mechanical Systems (MEMS 2005), Miami Beach, FL, Jan. 30 - Feb. 3, pp. 227-230, 2005.
- [150] T. Krupenkin, S. Yang, and P. Mach, "Tunable Liquid Microlens," *Applied Physics Letters*, vol. 82, pp. 316-318, 2003.
- [151] A. Jain and H. Xie, "An Electrothermal Microlens Scanner with Low-Voltage Large-Vertical-Displacement Actuation," *IEEE Photonics Technology Letters*, vol. 17, pp. 1971-1973, 2005.
- [152] A. Jain and H. Xie, "A Tunable Microlens Scanner with Large-Vertical-Displacement Actuation," Technical Digest of the 18th IEEE International Conference on Micro Electro Mechanical Systems (MEMS 2005), Miami Beach, FL, Jan. 30 - Feb. 3, pp. 92-95, 2005.
- [153] D. Daly, *Microlens Arrays*. London: Taylor & Francis, 2001.
- [154] A. L. Glebov, L. Huang, S. Aoki, M. Lee, and K. Yokouchi, "Planar Hybrid Polymer-Silica Microlenses with Tunable Beamwidth and Focal Length," *IEEE Photonics Technology Letters*, vol. 16, pp. 1107-1109, 2004.
- [155] A. Jain and H. Xie, "Half-Millimeter-Range Vertically Scanning Microlenses for Microscopic Focusing Applications," Technical Digest of the 2006 Solid State Sensors, Actuators and Microsystems Workshop, Hilton Head Isl., SC, pp. 74-77, 2006.

BIOGRAPHICAL SKETCH

Ankur Jain enrolled at the Birla Institute of Technology and Science, Pilani, India, in the fall of 1996 for the B.E. (Honors) degree in electrical and electronics engineering. As an undergraduate at BITS, he participated in various projects including the design of an optoelectronic arrayed waveguide multiplexer, and also the design of an infrared transceiver system for indoor wireless communication. He completed his bachelor's degree in 2000, and was awarded the Motorola Student of the Year Gold Medal upon graduation. He received the M.S. degree in electrical and computer engineering from the University of Florida in 2002 where he specialized in the areas of photonics, semiconductor device theory, and computer systems and networking.

Ankur joined the Interdisciplinary Microsystems Group in 2002 to pursue a Ph.D. degree that involved the development of optical MEMS scanners for endoscopic biomedical imaging systems. His research interests include optical microsystems, endoscopic biomedical imaging, photonic devices, CMOS-MEMS microfabrication, and carbon nanotubes. His doctoral research has contributed to over 20 research publications, and he has also co-authored a book chapter in the MEMS/NEMS Handbook.

He is a member of the Institute of Electrical and Electronics Engineers and the Optical Society of America, and is also a member of the Eta Kappa Nu and Tau Beta Pi honor societies. After receiving his PhD degree in 2006, he plans to pursue a career in the area of optical microsystems.